Electron correlation in multiple ionization of atoms and molecules by intense ultra-short laser pulses

vorgelegt von
Diplom-Physikerin
Ekaterina Eremina
aus Kasan (Russland)

von der Fakultät II - Mathematik und Naturwissenschaften
der Technischen Universität Berlin
zur Erlangung des akademischen Grades

Doktorin der Naturwissenschaften
- Dr. rer. nat. -

genehmigte Dissertation

Promotionsausschuss:

Vorsitzender:	Prof. Dr. Mario Dähne
Berichter:	Prof. Dr. Wolfgang Sandner
Berichter:	Prof. Dr. Thomas Möller

Tag der wissenschaftlichen Aussprache: 25.04.2005

Berlin 2005
D 83

Abstract

The ionization dynamics of Ar and Ne atoms as well as N_2 and O_2 molecules in intense ultra-short laser pulses has been investigated by means of highly differential correlated electron-ion momentum spectroscopy. The main goal was to understand the detailed mechanism behind Non-Sequential Double Ionization (NSDI) and the influence of the atomic and molecular structure on the final electron-electron momentum correlation after NSDI.

The experimental results for Ne can be well understood within the instantaneous rescattering-induced electron impact ionization mechanism, while for Ar the assumption of an additional ionization channel is necessary. For the latter the likely scenario is electron impact excitation of the singly charged ion with subsequent electric field ionization. The role of this mechanism in the NSDI process increases with decreasing light intensity. The detailed analysis of the final electron momentum distributions for Ar and Ne shows that the electric field of the light wave essentially influences the recollision process in NSDI.

Significantly different electron-electron momentum correlations are found for N_2 and O_2. Both molecules show new features which are not observed for atoms. The comparison of the N_2 molecule and Ar atom, both having a comparable ionization potential, at similar light intensities reveals the effect of the two nuclei.

A semiclassical analysis based on the rescattering model has been applied to the N_2 and O_2 molecules in order to test the applicability of the electron impact ionization mechanism. The model calculation includes the symmetry of the initial molecular state occupied by the active valence electron. The results of this calculation qualitatively reproduce the main features found in the experiment. Two important conclusions can be drawn. First, electron recollision seems to be the general mechanism of NSDI for both atoms and molecules. Second, the molecular structure decisively influences the final electron-electron momentum correlation after NSDI.

It has been found that the bonding symmetry of the initial state of the molecule strongly modifies the inelastic electron recollision. In contrast, the antibonding symmetry mainly affects the first stage of NSDI during the electron transition to the ionization continuum via tunneling. This can be interpreted as interference effects of the emitted electronic wave packet with the bound electron at the instant of recollision as well as in the final state of the two photoelectrons.

Zusammenfassung

Es wurde die Ionisationsdynamik der Atome Ar und Ne als auch die der Moleküle N_2 und O_2 in intensiven ultrakurzen Laserpulsen mittels hochdifferentieller Elektron-Ion-Koinzidenz-Impulsspektroskopie untersucht. Das Hauptziel der Arbeit ist, den detaillierten Ionisationsmechanismus der nichtsequentiellen Doppelionisation (NSDI) und den Einfluss der atomaren und molekularen Strukturen auf die Impulskorrelation der Photoelektronen nach der NSDI zu verstehen.

Die experimentellen Ergebnisse für Ne lassen sich gut durch den Mechanismus der instantanen rückstreuinduzierten Elektronenstoßionisation erklären, während für Ar die Annahme eines zusätzlichen Ionisationskanals notwendig ist. Das wahrscheinliche Szenario für diesen Mechanismus ist die instantane Elektronenstoßanregung des einfachgeladenen Ions mit folgender Ionisierung durch das elektrische Feld der Lichtwelle. Mit abnehmender Lichtintensität wird der Beitrag dieses Ionisationsmechanismus zu der Impulskorrelation der Photoelektronen größer. Die detaillierte Analyse der Elektronimpulsverteilungen für Ar und Ne deutet auf einen wesentlichen Einfluss des elektrischen Feldes der Lichtwelle zum Zeitpunkt des Elektronenstoßprozesses der NSDI hin.

Für N_2 und O_2 wurden sehr unterschiedliche Elektron-Elektron-Impulskorrelationen gefunden. Beide Moleküle zeigen neue Charakteristiken, die für Atome nicht gefunden wurden. Die Rolle der zwei Kerne zeigt sich in dem Vergleich des N_2-Moleküls und des Ar-Atoms, beide mit ähnlichen Ionisiationspotentialen, bei gleicher Lichtintensität.

Um die Relevanz der Elektronenstoßionisation für die Moleküle N_2 and O_2 zu testen, wurde eine semiklassische Methode eingesetzt, die auf dem Rückstreumodel basiert. Die Modellrechnung berücksichtigt die Symmetrie des mit einem Valenzelektron besetzten molekularen Anfangszustands. Die Rechnung reproduziert qualitativ die wesentlichen Ergebnisse des Experiments. Daraus lassen sich zwei wichtige Schlüsse ziehen. Erstens, instantane Elektronenstoßionisation scheint der allgemeine Mechanismus der NSDI zu sein, sowohl für Atome als auch für Moleküle. Zweitens, die molekulare Struktur hat entscheidenden Einfluss auf die Impulskorrelation der Photoelektronen nach der NSDI.

Es wurde herausgefunden, dass die bindende Symmetrie des molekularen Anfangszustandes den inelastischen Elektronenrückstoss stark modifiziert, während die antibindende Symmetrie hauptsächlich das Elektronentunneln in der erste Stufe der NSDI beeinflusst. In beiden Fällen kann der Vorgang als Interferenzeffekt der beiden beteiligten Elektronen interpretiert werden: sowohl zum Zeitpunkt des Rückstoßes des emittierten Elektronenwellenpakets mit dem gebundenen Elektron als auch im Endzustand der beiden Photoelektronen.

Contents

List of Figures

List of Tables

List of Abbreviations

ADK	Amosov-Delone-Krainov
ATI	Above Threshold Ionization
COLTRIMS	COLd Target Recoil Ion Momentum Spectroscopy
CPA	Chirped Pulse Amplification
e^--e^-	electron-electron
FWHM	Full Width at Half Maximum
HHG	High Harmonics Generation
KFR	Keldysh-Faisal-Reiss
LCAO	Linear Combination of Atomic Orbitals
LOPT	Lowest-Order Perturbation Theory
MCP	Microchannel Plate
MPI	Multiphoton Ionization
NSDI	Non-Sequential Double Ionization
OTBI	Over-The-Barrier Ionization
SAE	Single Active Electron
TDC	Time-to-Digital Converter
TDSE	Time-Dependent Schrödinger Equation
TOF	Time Of Flight
UHV	Ultra-High Vacuum
XUV	eXtreme Ultra-Violet

1. Introduction

The discovery of lasers at the beginning of the sixties opened literally a new era for researchers. Impetuous development of laser technologies has made the laser a part of our everyday life today – from CD-ROM, laser pointer and supermarket checkout lines (*laser-based ICT*) to laser vision correction (*laser medicine*) and cutting of precise patterns in glass or metal (*laser-based materials processing and manufacturing*). Indeed lasers found very broad applications in industry, biology and medicine. They are, however, not less important research tools. Today it is impossible to imagine spectroscopy without lasers. In recent years more and more powerful lasers with extremely short pulses became available. This opened a new research field of light-matter interaction. In particular, this thesis addresses interaction of atoms and molecules with very intense ultra-short laser pulses.

A great progress in the development of the laser techniques since the sixties of the last century has been achieved. It started from **Q-switching** lasers, which delivered few-nanosecond pulses with a laser peak power of megawatt, and has been developed through the **mode-locking** to the **chirped pulse amplification technique** (CPA), which allows to reach a peak laser pulse intensity up to $10^{20} W/cm^2$ in the femtosecond pulse regime. In the CPA scheme laser pulses are stretched, amplified, and then compressed [3]. Due to the available high light intensity new nonlinear nonperturbative phenomena were discovered, such as multiphoton ionization, coherent emission of high frequency radiation by atoms, and laser-assisted electron-atom collisions.

The atomic physics in intense laser fields perhaps dates back to the first experimental observation of seven-photon ionization of Xenon with a ruby laser by Voronov and Delone in 1965 [4]. **Multiphoton ionization** (MPI) was predicted already in 1931 by Maria Göppert-Mayer, a student of Max Born, who showed that ionization of an atom can happen by absorbing many photons if the energy of one photon is not enough to overcome the ionization potential [5]. The next remarkable phenomenon, which has been called **above threshold ionization** (ATI), was discovered in Saclay by Agostini and collaborators in 1979. They found that, at a sufficient light intensity (of about $10^{13} W/cm^2$), a photoelectron is able to absorb more photons than the minimum required for MPI [6]. Another effect related to ATI is **high-order harmonics generation** (HHG), where an atom responds nonlinearly to a strong laser field emitting radiation with odd harmonics of the laser field frequency (for a recent

review see [7, 8]). This phenomenon became very important for developing compact (top-table) powerful high-frequency X-ray and XUV laser sources with attosecond pulse width.

In a low-frequency strong laser field, when the electric field of a light wave competes with the Coulomb field in an atom, one can consider the ionization process as electric field ionization, i.e. tunnelling through an effective potential barrier, which is formed by suppression of the Coulomb potential in the external electric field. Here, the necessary condition is that the time the e^- needs to tunnel through the potential barrier is small compared to the period of the laser field. This theoretical approach was first considered by Perelomov, Popov, and Terent'ev [9] and further developed by Amosove, Delone and Krainov [10]. First experiments on single ionization of noble gases and helium by high-intensity laser pulses showed a good agreement with the tunnelling theory. But for multiple ionization, when more than one electron is ionized, the experimental results showed a strong deviation from the tunnelling approach. In particular, the experimentally observed ionization rate of doubly and multiply charged ions was found to be many orders of magnitude larger than it was predicted theoretically [11, 12, 13, 14]. The highly nonlinear process in a strong laser field, which is responsible for this deviation, is now known to be **non-sequential ionization**. In the last years the study of **non-sequential double ionization** (NSDI) has attracted much interest of theoreticians and experimentalists. Highly differential methods like electron and ion momentum spectroscopy and kinetic energy spectroscopy allow one to analyze the dynamics of the ionization processes (e.g. [15, 16, 17, 18, 19, 2]). The correlation between the two photoelectrons was found to play a decisive role in the mechanism of NSDI. Actually electron correlation effects are important not only in atomic physics, but also for phenomena in condensed matter physics such as high temperature superconductivity and magnetism.

For molecules, the application of intense laser fields offers a possibility to manipulate inter- and intramolecular dynamics as well as orient, focus molecular beams, control chemical reactions. In addition, intense lasers may be employed as "soft" ionizers for sophisticated mass spectrometry of large molecules. The development of scientific and practical applications of the intense laser fields to molecules requires a complete comprehension of molecular behavior in strong laser fields. One of the basic problems is the understanding of the ionization dynamics of molecules in strong fields.

The present thesis, supervised by Prof. W. Sandner, has been performed at the Max-Born-Institute for Nonlinear Optics and Short Pulse Spectroscopy in Berlin. It is dedicated to a study of non-sequential double ionization of different atomic and molecular systems and of the electron correlation in the ionization process. An experimental technique based on ion and coincident ion-electron momentum spectroscopy, which is also known as **Cold Target Recoil Ion Momentum Spectroscopy** (COLTRIMS), was employed for this goal.

The following questions have been addressed within this work:

- detailed ionization mechanism behind NSDI;
- atom specific features of the final electron momentum correlation after NSDI;
- NSDI via instantaneous electron impact ionization under conditions where it is energetically forbidden within the semiclassical rescattering model (below ionization threshold);
- NSDI of molecules, comparison with atoms having similar ionization potentials;
- influence of molecule specific effects on the final momentum correlation.

The present thesis is organized as follows. An overview of the main multiphoton processes is given in Chapter 2, including the discussion of different theoretical models developed for NSDI. In Sec. 2.5 the dynamics of a free electron in a laser field is considered. The latter is an important part of the NSDI process.

The experimental setup used for the present investigation is described in detail in Chapter 3. It includes the momentum spectrometer together with the electronics for the data acquisition and the laser system. The momentum resolution of the spectrometer and the determination of the light intensity of the focused laser beam are also discussed in this chapter.

Chapter 4 presents the actual experimental results on NSDI of atoms. The observed electron sum-momentum distributions for Ar and Ne as well as their electron momentum correlation after NSDI will be discussed. An explanation is given for NSDI via electron impact ionization found at light intensities where it is not expected within the semiclassical rescattering model. A qualitative comparison of the experimental data with a semiclassical model calculation based on rescattering will be given as well. Finally, several theoretical models and their relevance for the experiment are considered.

Chapter 5 is dedicated to NSDI of molecules. N_2 and O_2 molecular systems are considered. Electron sum-momentum distributions and the final electron momentum correlations are presented and discussed. In this chapter a semiclassical model is developed for NSDI of molecules. The model allows one to reproduce the main features found in the experiment as well as to understand different ionization behavior of N_2 and O_2. It is based on the initial-state symmetry of the molecular orbital occupied by the active valence electrons.

2. Ionization in intense laser fields: fundamentals

The present chapter focuses on fundamental aspects of the ionization dynamics in intense laser fields and gives an overview of the accumulated knowledge on this topic. Special attention is given to the matter of non-sequential ionization, including the rescattering ionization mechanism and various theoretical approaches. The presented material is partly guided by several reviews devoted to multiphoton processes in intense laser fields [20, 21, 22, 23].

2.1 Multiphoton ionization

The transition from a bound state to a continuum state by absorbing many photons is known as multiphoton ionization (MPI). It occurs if the energy of one photon is not enough for ionization (see Fig. 2.1 (b)). One can write down schematically the reaction of multiphoton one-electron ionization as follows

$$n\hbar\omega + A \rightarrow A^+ + e^-, \tag{2.1}$$

where $\hbar\omega$ is the photon energy and n is an integer. As mentioned before, this process was first observed by G.S. Delone and N.B. Voronov in 1965 [4], who detected seven-photon ionization of xenon using a ruby laser. In the same year J.L. Hall and collaborators recorded two-photon ionization of the negative Iodine ion I^- [24]. Early experiments on MPI at relatively low light intensity ($< 10^{13}$ W/cm^2) were in good agreement with lowest-order perturbation theory (LOPT) [25, 26] where the n-photon ionization rate is given by

$$\omega_n = \sigma_n I^n. \tag{2.2}$$

Here, n is the minimum number of photons needed for ionization, σ_n the n-photon ionization cross section and I the light intensity of the laser beam. This highly nonlinear dependence on light intensity was proven experimentally up to $n = 22$ for MPI of He [27]. However this intensity scaling breaks down at a critical intensity. Above this critical value there is no change in the intensity dependence of the ion yield [28]. This can be explained in terms of population depletion [29]. In general,

in an experiment we deal with a pulsed focused laser beam with an inhomogeneous intensity distribution in the ionization volume and in time. For a given pulse duration all atoms in the focus will be ionized if the light intensity is larger than the so-called saturation intensity. The latter can be lower than the peak intensity of the laser pulse. In order to obtain ionization up to the peak intensity of the laser pulse we require shorter pulses.

2.2 Above threshold ionization

At light intensities $> 10^{13}$ W/cm^2 the low-order perturbation theory is no longer valid because of the strong coupling of the atomic states with the pulsed laser field, which leads to the AC-Stark shift. In this regime of light intensity an electron can absorb more photons than the minimum needed to overcome the ionization barrier. This process is known as **above threshold ionization** (ATI) and is depicted schematically in Fig. 2.1 (c). Experimentally ATI was first observed by P. Agostini

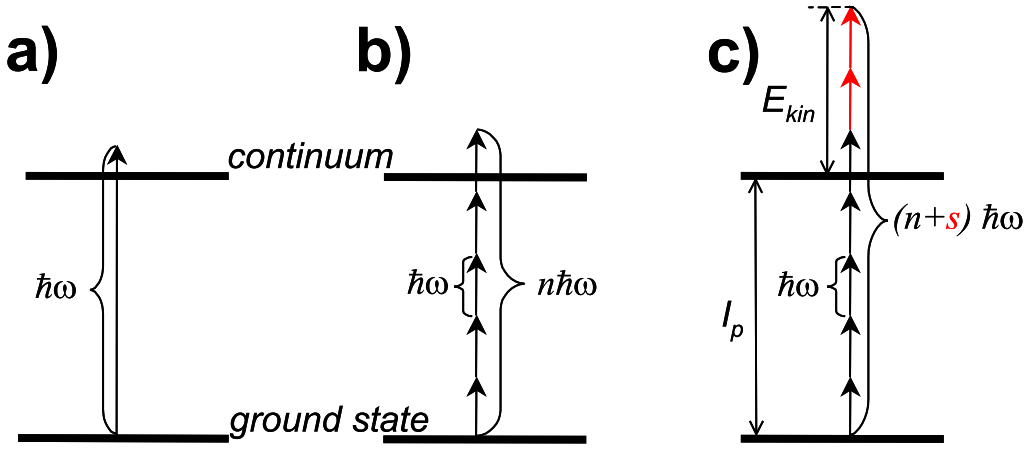

Fig. 2.1: Schematic diagram of ionization mechanisms: a) one-photon ionization; b) multiphoton ionization by n photons; c) above-threshold ionization by $(n+s)$ photons.

et al. (1979) [6]. In the photoelectron energy spectrum of six-photon ionization of Xe at 10^{13} W/cm^2 they found a second energy peak separated from the expected first one by the photon energy. An example of ATI spectra of Xe is shown in Fig. 2.2. After this discovery energy-resolved photoelectron spectra have been studied in detail for different atoms and molecules and with lasers at different wavelengths [25, 30, 1, 31, 32]. Despite its obstructions perturbation theory has been applied to ATI [33] and has been shown to be sufficient to account for experimental results in a certain intensity range [25]. The ionization rate then has a more general form than

Eq. (2.2)

$$\omega_{n+s} \propto I^{n+s}, \tag{2.3}$$

where s is the number of excess photons absorbed. The photoelectron energy can be calculated from the extended Einstein photoeffect formula

$$E = (n+s)\hbar\omega - I_p \tag{2.4}$$

with I_p the ionization potential.

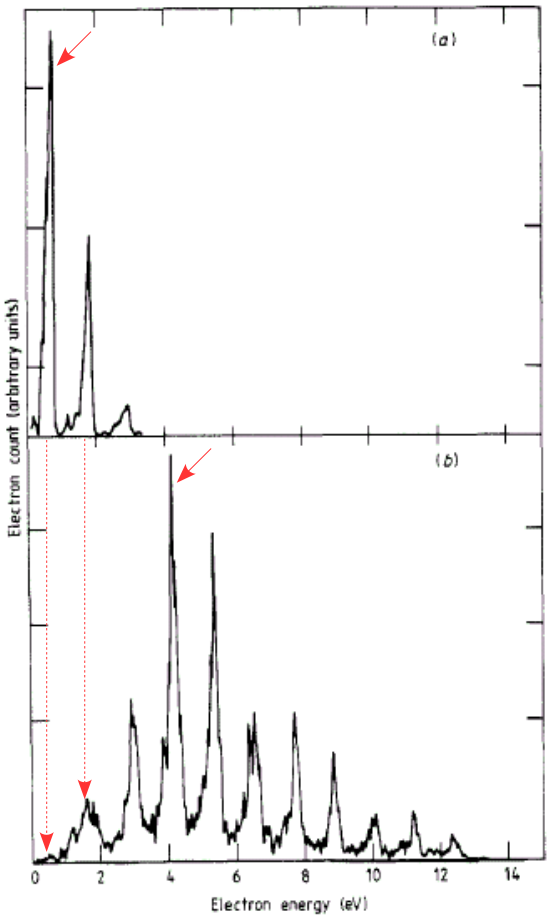

Fig. 2.2: ATI electron energy spectra of Xe at $\lambda = 1064$ nm with 130 ps laser pulses [1]. (a) $I = 2.2 \times 10^{12}$ W/cm^2; (b) $I = 1.1 \times 10^{13}$ W/cm^2.

Another remarkable feature of ATI is the suppression of the low-energy peaks in the photoelectron spectra. This effect occurs at increasing laser intensity (see the first two peaks marked with dashed red arrows in Fig. 2.2). The reason for this suppression is the AC-Stark shift of the energies of atomic states in the presence of

the external field. For low laser frequencies the AC-Stark shifts of the lowest bound states are not significant and can be neglected (e.g. a Nd-YAG laser with $\hbar\omega = 1.17$ eV). In contrast, the shift of Rydberg and continuum states is characterized by the electron **ponderomotive energy** U_p. The latter is an important parameter for many processes in intense laser fields. U_p is defined as the kinetic energy of the electron quiver motion in a laser field averaged over an optical cycle and is given by

$$U_p = \frac{e^2 E_0^2}{4m\omega^2}, \tag{2.5}$$

where m is the mass and e the charge of an electron, E_0 is the electric field strength and ω the frequency of the laser. The ionization barrier is boosted by U_p in the laser

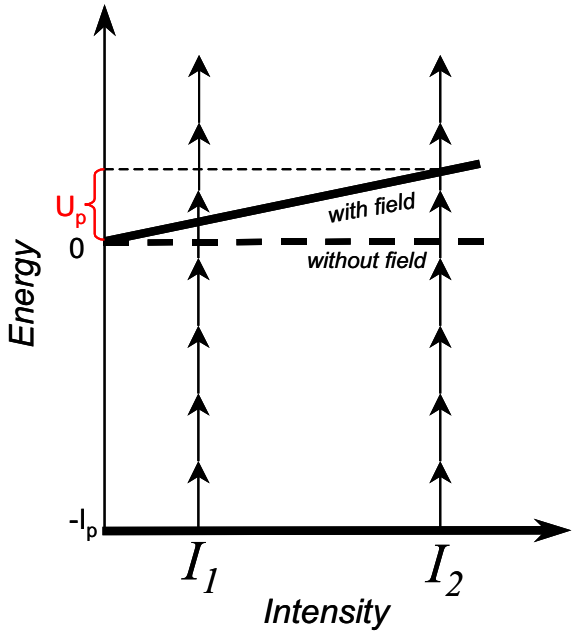

Fig. 2.3: Illustration of the Stark shift of the ionization potential depending on the laser intensity. At the intensity I_1 five-photon ionization occurs, whereas at the higher light intensity I_2 one photon more is needed for ionization. The ionization threshold is increased by U_p.

field (Fig. 2.3) and the final photoelectron energy is given by

$$E = (n + s)\hbar\omega - (I_p + U_p). \tag{2.6}$$

Fig. 2.3 illustrates the AC-Stark shift of the ionization threshold. One can see that ionization by absorption of $n = 5$ photons, which is possible at the laser intensity

I_1, is energetically forbidden at I_2. Here, one photon more is needed to ionize the atom. However, in experiment we deal with a smoothly varying intensity in the focus during the laser pulse, so that the corresponding energy peak at I_1 will not completely disappear. Fig. 2.2 demonstrates well this evolution of the main energy peak (marked with the small red arrow) with increasing laser intensity.

Despite the suppression at low energy, the positions of the ATI peaks in Fig. 2.2 do not change with increasing light intensity. The reason is the following. Due to the intensity gradient of a focused laser beam, a freed electron experiences a force $-\nabla U_p$. Accelerated by this force in the laser field, the electron regains exactly its ponderomotive energy deficit, which appears due to the ionization potential shift by U_p [34]. This is possible for long laser pulses ($\gg 1$ ps) when the laser intensity changes slowly compared with the time, the photoelectron needs to leave the focal spot. As a consequence, the photoelectron peaks appear at the same energy as predicted in Eq. (2.4). For sub-picosecond laser pulses (< 1 ps), however, there is no time for the photoelectron to acquire the full amount of energy during the ponderomotive acceleration in the laser field before the end of the pulse. Therefore, the ATI peaks become shifted towards lower energies. Such a shift as well as a broadening of the ATI energy peaks with decreasing laser pulse width has been observed experimentally [31]. Additionally, fine structures appear in the photoelectron energy spectrum when sub-picosecond laser pulses are used [35, 36, 37]. The origin of these structures has been attributed to resonant MPI processes. The latter occur for excited states when ac-Stark shifted into resonance during the laser pulse[37]. In the long-pulse regime the substructures in the ATI electron energy spectrum cannot be resolved due to the ponderomotive acceleration of the photoelectron in the intensity gradient of the focused laser beam.

2.3 Tunneling ionization

Using laser techniques, based on the **Chirped Pulse Amplification** (CPA) scheme [3], it has become possible to produce very intense ultrashort light pulses with a light intensity of the focused laser beam in excess of $10^{14} - 10^{15}$ W/cm^2. Such a light intensity corresponds to an electrical field strength of about $10^8 - 10^9$ V/cm. This is already comparable with the strength of the Coulomb field in an atom and is considered as a strong field. In this case perturbation theory is no more valid. A more useful approach is obtained by considering the strong-field photoionization process as tunneling through an effective potential barrier. The latter is formed by the suppression of the atomic potential in the laser electric field as shown in Fig. 2.4. Such an approach is valid if the oscillation period of the external field is long enough in comparison with the time the electron needs to tunnel through the potential barrier. This quasi-stationary theory was first worked out by Keldysh

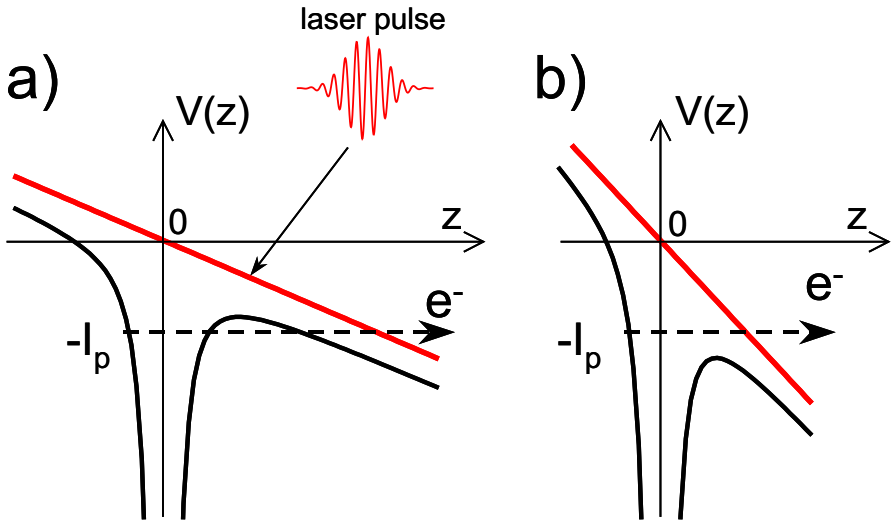

Fig. 2.4: Schematic diagram of strong-field photoionization mechanisms: a) tunneling; b) over-the-barrier ionization.

(1965) [38] and then developed further by many theoreticians [10, 9, 39, 40, 41, 42]. Using a quasi-stationary model in the low-frequency limit first Perelomov, Popov, and Terent'ev [9] and then Amosov, Delone and Krainov [10] have found a tunneling ionization rate (ADK rate) which is given by

$$\omega = \omega_0 \exp[-\frac{2(2I_p)^{3/2}}{3E}]. \tag{2.7}$$

Here, I_p is the ionization potential, E is the laser field strength and ω_0 is a slowly varying function of E, I_p and Z, the atomic core charge. The atomic unit system ($\hbar = m_e = e = 1$) is used.

As the laser intensity is further increased a critical value of the intensity is eventually reached. Beyond this value the Coulomb potential is so strongly suppressed by the external field that the ground state is no longer bound. An electron then just "flows over the top" of the barrier as shown in Fig. 2.4 (b). This process is known as **over-the-barrier ionization** (OTBI) and occurs at 1.4×10^{14} W/cm^2 for atomic hydrogen. The critical intensity for OTBI is defined by [21]

$$I_{cOTBI} = \frac{c\epsilon_0 I_p^4}{32Z^2}, \tag{2.8}$$

with c the speed of light and ε_0 the dielectric constant of vacuum.

As a quantity indicating the transition from multiphoton ionization to the low-frequency tunneling limit Keldysh has introduced the adiabaticity parameter γ.

The latter can be defined as the ratio of the mean time the electron needs to tunnel through the potential barrier [38] to the period of the laser field oscillation, which can be expressed as

$$\gamma = \frac{\omega\sqrt{2mI_p}}{eE} = \sqrt{\frac{I_p}{2U_p}}, \tag{2.9}$$

where I_p is the field free atomic ionization potential and U_p is the ponderomotive energy. For $\gamma > 1$, multiphoton absorption is adequate to describe the ionization process. In contrast, for $\gamma < 1$ the quasistatic tunneling ionization is most appropriate. The transition between the two approaches, multiphoton and tunneling, takes place at $\gamma = 1$. It occurs over a rather narrow range of light intensity or frequency. In the intermediate regime with $\gamma \sim 1$ the ionization process has a complicated character and is difficult to model. In fact multiphoton ionization and tunneling are two limiting cases of one ionization process. Moreover, the formula (2.7) was obtained with a short-range atomic potential, while for real atoms it is rather long-range. Actually, for real atoms the laser field effect on a freed photoelectron is accompanied by the Coulomb force of the ionic core. An analytical solution of such a complex problem is highly complicated [43]. Experiments in optical, infrared and ultraviolet wavelength ranges have confirmed qualitatively the exponential dependency of the ionization rate found in (2.7) at $\gamma < 1$ and also at $\gamma \sim 1$ [44, 45, 12, 46].

From Eqs. (2.9) and (2.5) follows that the Keldysh parameter depends on the frequency and is inversely proportional to the square root of intensity of the field. In contrast to the quite high laser intensities needed to obtain tunneling ionization in the optical region (e.g. $> 10^{14}$ W/cm^2 for an 800 nm Ti:Sa laser), microwave tunneling ionization of highly excited Rydberg atoms has been obtained in considerably weaker fields [47, 48].

2.4 Non-sequential multiple ionization

The formation of doubly charged ions in multiphoton ionization was first observed for the alkaline-earth atoms Ba and Sr with two valence electrons on the outer shell [49]. Later it was also found for the rare-gas atom Kr ionized by Nd:YAG laser pulses [50]. The light intensity necessary to obtain multielectron ionization via absorption of many photons is about 10^{13} W/cm^2 and higher.

At the time of these experiments, theoretical methods allowed one to calculate the total ionization rate for multi-electron ionization in intense laser fields based on the so called **single-active-electron approximation** (SAE) [10, 41, 42, 51, 52]. In this approximation, correlations between electrons in a many-electron atom are included only via the field-free initial state wave function. The ionization dynamics is only governed by the outermost electron while the other electrons are "frozen". The latter only contribute to the effective atomic potential (Hartree-Fock potential). In

this way the SAE approximation assumes that multi-electron ionization is a stepwise process (sequential ionization). For instance double ionization can be written as a two-step process

$$A + n_1\hbar\omega \longrightarrow A^+ + e^-, \tag{2.10}$$

$$A^+ + n_2\hbar\omega \longrightarrow A^{++} + e^-, \tag{2.11}$$

where n_1 and n_2 are the numbers of absorbed photons. With the new generation

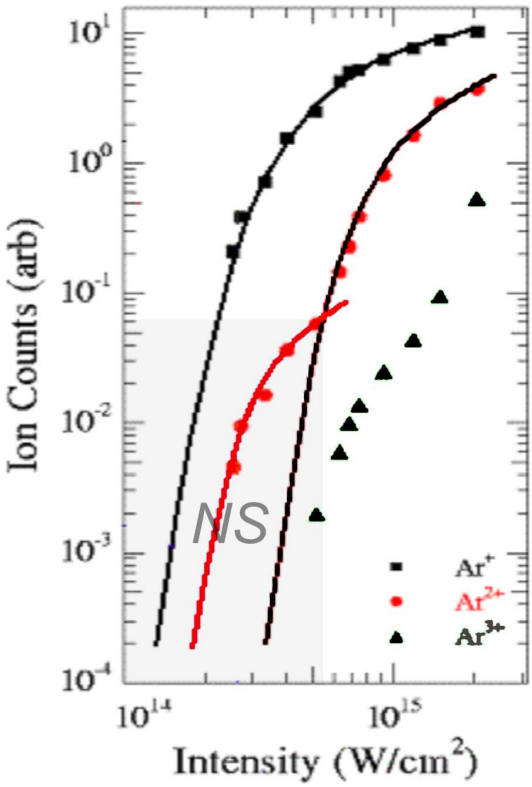

Fig. 2.5: Ion yield dependence on light intensity for single (■), double (●) and triple (▲) ionization of Ar using Ti:Sapphire laser radiation (800 nm, 80 fs) from [2] [1]. The two black curves are the ion yields calculated using ADK tunneling rates for single and double (sequential) ionization. The red curve is for non-sequential double ionization.

of high-power, stable laser systems with ultra-short pulses (of the order of fs) and high repetition rates it became possible to measure total ion yields for higher charge states for all rare-gas atoms and also for He with high precision. These SAE-based

[1] see also the web site http://gomez.physics.lsa.umich.edu/nsdidetail.html.

approaches to double and multiple ionization were found to be no more applicable for the description of such experiments. Although the experimentally found dependence of the total ionization rate on light intensity for singly charged ions was in perfect agreement with sequential ADK model, the results for double ionization in a certain intensity range showed an ion yield which is many orders of magnitude higher than theoretically predicted [12]. Only at high laser intensity, where single ionization is saturated, double ionization becomes sequential (see Fig. 2.5 for Ar). There is a characteristic "knee" structure in the ion yield curves for double and triple ionization between the two intensity ranges. At this point sequential ionization starts to dominate over non-sequential ionization as the intensity is further increased (Fig. 2.5). This failure of the theory to predict the experiment correctly, suggests that two electrons are removed from a neutral atom simultaneously rather than in a sequential way

$$A + n\hbar\omega \longrightarrow A^{++} + e^- + e^- \tag{2.12}$$

This ionization process is called **Non-Sequential Double Ionization** (NSDI). It was observed first for Xe [11], then for He [12, 14, 53] and other rare-gas atoms [54, 55, 56], and meanwhile also for some molecules [57, 58, 59]. The observation of NSDI is a strong evidence of electron correlation in strong field physics.

In order to explain NSDI several mechanisms were proposed.

- **"Shake-off"**

  Fittinghoff et al. [12] proposed a "shake-off" mechanism for non-sequential ionization. This mechanism is known to be responsible for double ionization by absorption of a single high-energy photon ($\hbar\omega \gg I_p$) [60]. Here, an electron is removed during ionization in the laser field so fast that the remaining electrons cannot adjust adiabatically to the new eigenstates. Thus some of them may become excited to a higher-energy state or directly shaken off into the ionization continuum.

- **Rescattering**

  Rescattering (also referred to as the "simple-man model") was proposed originally by Kuchiev [61] under the name "antenna model". He assumed that an ionized electron is driven in the laser field acting as an antenna. The latter absorbs the energy which is then shared with a bound electron via correlation. This idea was extended by Schafer et al. [62] and Corkum [63] to a three-step rescattering model as presented in Fig. 2.6.
  In the first (bound-free) step, an electron is liberated from its parent atom by tunneling or via over-the-barrier ionization. The probability for these processes is maximum near the extrema of the oscillating electric field in the laser pulse.

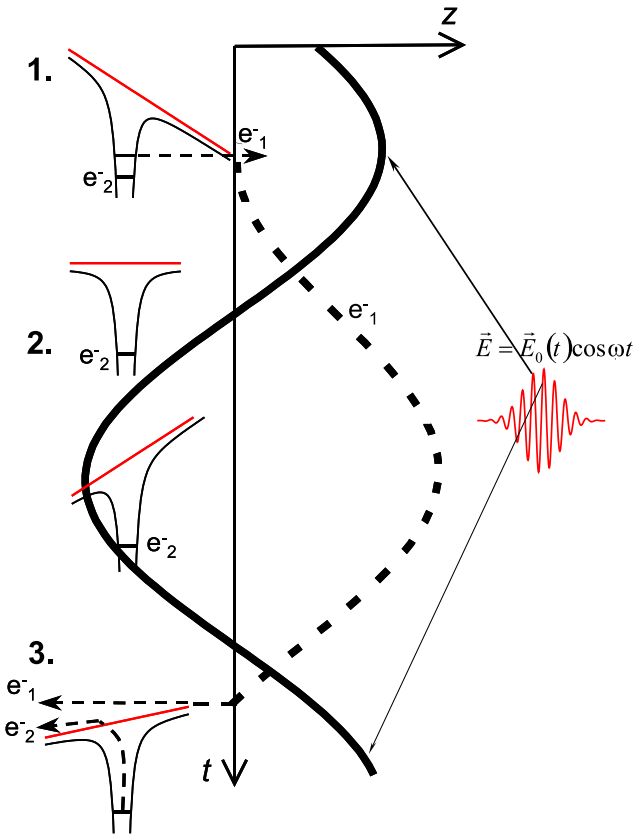

Fig. 2.6: Rescattering ionization mechanism: after tunneling through the effective barrier (1.), electron e_1 moves in the electric field of the light wave during one optical cycle (2.), until it is driven back to the parent ion core where it can ionize a bound electron e_2 by an inelastic collision (3.).

In the second (free-free) step, the free electron is accelerated by the electric field of the laser away from the remaining ionic core. As the phase of the field reverses the electron can be driven back to its parent ion core with some additional energy acquired from the field.
When the electron returns to the core (most effectively in linearly polarized light) a third step takes place: an inelastic scattering of the energetic electron by the core leads to ionization of a second electron.

- **Collective Tunneling**

  A further mechanism for NSDI was suggested by Eichmann et al. [64]. Here, two electrons tunnel together through the Coulomb barrier which is suppressed in the laser field. From an analytical model calculation and numerical solution

of a 1D Schrödinger equation it has been concluded that collective two-electron tunneling ionization does exist in a strong electric field if both electrons stay at equal distance from the nucleus. However, the total ionization rate for two-electron collective tunneling was found to be too small to account for the observed NSDI in a strong laser field [64]. Rather, collective tunneling can become a dominant ionization mechanism in a static (or quasi-static) field with a very high field strength or for half-cycle pulses, when there is no time for rescattering.

First guess-work about the mechanism behind NSDI came from experiments where the dependence of the total yield of doubly charged ions on the polarization of the laser beam was studied [54, 65]. It was found [54] that NSDI is suppressed in elliptically polarized light and the "knee" structure completely vanishes at circular polarization. This effect can be understood within the rescattering model while the "shake-off" and collective tunneling fail to explain it. For Ar, the experimentally observed dependence of NSDI on wavelength [13] also suggests rescattering as the main ionization mechanism. Furthermore the semiclassical rescattering model was successfully used to explain some effects related to NSDI, such as high harmonics generation (HHG) [62, 63] and the existence of a "plateau" in ATI photoelectron energy spectra [32, 66]. Elastic scattering of the active electron on its parent ion core contributes to the emission of high-energy ATI photoelectrons while recombination of the electron with the ion results in the release of its kinetic energy plus the ionization energy in the form of short-wavelength photon emission (HHG).

At first sight the semiclassical rescattering model predicts the appearance of an NSDI threshold at a certain critical laser intensity. For intensities lower than this value the returning electron can no longer get enough energy from the laser field to ionize the second bound electron directly. Thus one would expect an abrupt change in the intensity dependence of the ratio of double to single ionization rates. However, no such threshold was found experimentally [14, 67].

The validity of any of the ionization mechanisms cannot be revealed based on the integral measurements of the total ion yields only. These measurements are integrated over all final kinetic energies, yielding just the number of ions or electrons, and thus do not give any idea of the dynamics of the ionization process and the correlation between photoelectrons. In order to obtain more insight into the underlying physics, differential methods are necessary, for example, photoelectron spectroscopy or correlated measurements of the energy and angular distribution of the photoelectrons. In differential measurements the energy or momentum of every electron (ion) can be detected. Unfortunately, the first experimental results on electron spectroscopy based on electron-electron and electron-ion coincidence measurements for Xe [53] have not been sufficient to reveal the mechanism of non-sequential ionization.

Considerable progress in the study of multiple ionization in high-intensity laser

fields by differential methods was made, when the momentum imaging technique was applied to the problem. The momentum distributions of doubly charged He and Ne ions were measured with so-called Cold Target Recoil Ion Momentum Spectroscopy (COLTRIMS) [16, 17]. These experiments were soon extended to a kinematically complete momentum analysis of the final state of the photoelectrons after ionization [68, 69, 70, 71, 72]. The pioneering experimental works have been done by the group of R. Dörner (Frankfurt University) in collaboration with Marburg University and the group of J. Ullrich (MPI, Heidelberg) in collaboration with our group (MBI, W. Sandner). Based on these measurements and also on highly resolved electron kinetic energy distributions measured in coincidence with doubly charged ions [18, 19, 2, 73], the mechanism of non-sequential ionization of atoms in high-intensity laser fields was identified as rescattering. However, the question of an ionization threshold for the rescattering mechanism is still open. Moreover, the ionization rates found in experiment cannot be reproduced quantitatively. The theoretical treatment of the problem of atomic ionization in high-intensity laser fields is quite complicated. The laser field is too strong to allow perturbative methods to be applied. Furthermore, one has to deal with a quantum many-body atomic system and a nonseparable Coulomb correlation between electrons. There are several theoretical approaches which have been used to interpret the experimental results on NSDI of atoms in high-intensity laser field. Most of them are applied to the He atom as the simplest correlated two-electron system.

- **Numerical Integration of the TDSE**

  One *ab initio* approach is the attempt to solve the time-dependent Schrödinger equation (TDSE) for a few-electron system directly. For N electrons this involves a partial differential equation with $3N$ spatial variables to be solved over a realistically large space-time domain. For He, the assumption of an infinite nuclear mass and of a linearly polarized light wave efficiently reduces the problem to that of a five-dimensional time-dependent partial differential equation. A remarkable progress on numerical integration of the five-dimensional Schrödinger equation for He has been achieved in recent years using massively-parallel computing (Cray T3D) [74, 75, 76, 77, 78]. However, in these calculations the laser wavelength was limited to 390 nm. That is shorter than the typical wavelength used in experiments (800 nm). Just recently a numerical TDSE calculation for He at 780 nm has been performed [79]. As a result, a time delay between single and double ionization has been found which supports the idea of rescattering for NSDI of He. Unfortunately, till now there was no success, using this theoretical method, to obtain the final state electron momentum correlation or energy distribution. This would be highly desirable for comparison with experimental data.

- **Intense-field Many-body S-matrix Theory (IMST)**

In this systematic approach the quantum mechanical S-matrix theory is applied to the NSDI problem. The main Feynmann diagram of this approach can be interpreted in terms of the rescattering picture. The full transition matrix amplitude (S-matrix) is defined by three essential contributions:

- transition of an electron from a bound state to a so-called Volkov state in the continuum (wave function of a free e^- interacting with a plane-wave laser field);
- propagation of the ionized electron in the laser field with a vector potential $\vec{A}(t)$, which is described by the so-called Volkov propagator (time-evolution operator); here, the strong field approximation (SFA) is used, where the Coulomb interaction of the propagating electron with the remaining ion core and with the bound electrons is neglected as well as the influence of the laser field on the bound electrons;
- electron-electron interaction, which leads to the ionization of a second electron

Two different forms for the latter and crucial contribution to the S-matrix element have been considered. The first form includes the e^--e^- Coulomb interaction and ignores the interaction with the ion [80, 81, 82, 83, 84]. In the other form e^--e^- contact interaction localized at the position of the ion core is assumed [85, 86, 87]. In the earlier calculations any interaction between the two photoelectrons has been neglected in the final state after they reached the continuum.
The S-matrix calculations by A. Becker and Faisal have so far provided the closest agreement with experimentally observed double ionization rates [80, 88, 89].
A good agreement was found between S-matrix calculations involving the rescattering (correlated energy-sharing) picture [82] and experimental measurements of the photoelectron energy distribution for NSDI of He [19]. There was also agreement that "shake-off" can be ruled out as the main NS ionization mechanism for atoms in low-frequency laser fields.
The quantum-mechanical S-matrix analysis qualitatively reproduces the experimental results for the recoil-ion momentum distribution and for the correlated electron momentum distribution found for NSDI of Ne [85, 86, 87]. In contrast, for other rare-gas targets like He and Ar the theoretical calculations [81, 82, 84, 85] are not sufficient to explain the experimental data. Thus, a consideration of additional ionization mechanisms is required. One such mechanism will be discussed later in this section.
The comparison between the model implying an e^--e^- Coulomb interaction at

the instant of electron rescattering and the other model using a contact interaction reveals that the latter matches the experimental data better [86, 90, 91]. Despite the generally successful application of the IMST to interpret particular experimental results, there are some controversies concerning several points.
In particular, the importance of the Coulomb repulsion between the two outgoing photoelectrons in the final state is still unclear. Some calculations indicate that this interaction is essential to explain the recently observed "back-to-back" emission of two photoelectrons in the plane perpendicular to the electric field of the linearly polarized light wave [92]. In other NSDI calculations the effect of the e^--e^- Coulomb repulsion in the final state becomes visible in the e^--e^- momentum correlation spectrum if the transverse momentum (perpendicular to the light polarization) of one of the electrons is restricted to a small value [87, 91]. In contrast, for a nonrestricted transverse momentum $p_{1e,\perp}$, taking into account the final state e^--e^- repulsion results in an e^--e^- momentum correlation which does not agree with experiment.
Another point is the use of different gauges in the S-matrix treatment of the NSDI problem: *i.* the length gauge [86, 90, 91], and *ii.* the velocity gauge [81, 82, 92]. Some approximations in the S-matrix calculation obviously break gauge invariance since the results are quite different for the two gauges.
The crucial point, however, is that the above mentioned S-matrix approaches still miss the inclusion of the interaction of the returning electron in the intermediate state as well as of the two final state electrons with the ion core.

- **Semiclassical and Classical Approaches**

  Different semiclassical approaches have been developed on the basis of the simple rescattering model (e.g. [67, 93, 94, 95, 96]).
  In these approaches the ionization probability of the first electron by tunneling is determined by the ADK formula (2.7). The further evolution of the freed electron in the electric field of the laser is described using classical mechanics. The only free parameter in the rescattering model by Corkum is the impact parameter. This is determined by the spread of the electron wave packet transverse to the electric field of the light wave.
  The original rescattering picture [62, 63] neglects several important physical effects and thus, cannot predict quantitatively the double ionization yield. In particular, it does not take into account the Coulomb potential of the parent ion. Later it has been shown that the the ion's attracting Coulomb potential together with the laser field plays an important role for the NSDI yield (so-called Coulomb focusing) [93, 94, 95].
  Because of spreading a large part of the electron wave packet misses the ion at the first return. However, due to the Coulomb attraction, the electron trajectories can be focused (especially after multiple returns) onto the parent ion

and thus, the probability of electron collision-assisted ionization increases significantly.
Alternatively the returning electron may be trapped temporarily by the parent ion into Rydberg orbits. In this state the electron can gain additional energy during "soft" collisions with the ion until it finally ionizes a bound electron [95].
For certain electron trajectories in the continuum, the returning electron does not directly ionize a second bound electron. The collision then only leads to an excitation of the ion followed by laser-induced ionization. The probability for such a scenario depends on the energy of the recolliding electron and on the impact excitation cross section. The semiclassical theory for He including both, impact ionization and excitation plus the Coulomb focusing effect, predicts well the experimentally observed double to single ionization yield ratio [95].
For He and Ar impact excitation dominates the total inelastic scattering cross section over the whole range of electron impact energies. This fact is a possible reason for the discrepancy between experimentally found momentum distributions of He^{2+} and Ar^{2+} on one hand and Ne^{2+} on the other hand [97].
Despite its simplicity, the three-dimensional classical trajectory analysis for NSDI of atoms in linearly polarized light is able to reproduce qualitatively the characteristic double-hump structure of the electron sum-momentum distribution as well as the electron momentum correlation in the final state found in COLTRIMS experiments [98, 99, 100].
Apart from this semiclassical approach, a pure classical analysis of the final stage of NSDI has been developed which also reveals main features of the electron sum-momentum distributions [101]. The idea here is that the rescattering of one electron on the ionic core produces a highly excited two-electron complex, which is next doubly ionized in the laser field. The main requirement for two electron escape is the formation of a saddle in the Coulomb potential in the presence of the electric field of the laser; the relevant parameters for the model are the total energy of the excited complex and the time of its formation.

- **One-dimensional quantum mechanical approaches**

  As mentioned above, the full time-dependent 3D two-electron problem of the He atom in a laser field is still not solved for relevant experimental conditions, i.e. for near-infrared light [79]. For linearly polarized light the field is acting only in one direction. This gives an opportunity for testing various 1D quantum mechanical models, where the motion of both electrons is restricted to one dimension along the polarization direction [102, 103, 104, 105, 106].
  In such a 1D He model atom both, the electron-electron and the electron-nucleus interaction are described by the soft Coulomb potential $V(x) = -1/\sqrt{x^2+1}$.
  The time-dependent two-electron wave function is represented numerically on

a flat grid in the presence of the oscillating laser field [104, 107, 108, 109, 106, 110].
1D numerical simulations have the advantage of providing quite easily information on the time evolution of the correlated two-electron wave function in momentum and coordinate space.
1D numerical calculations are able to reproduce qualitatively the "knee" structure in the experimentally observed yield of the doubly charged ions as a function of light intensity [105, 111]. Within this model for NSDI it also has been shown that the two photoelectrons are emitted preferentially into the same direction. This feature is consistent with experimental results. Furthermore the experimentally observed ion momentum distribution can be reproduced in such a calculation [104]. In general, all 1D calculations support the validity of the rescattering model.
The main shortcoming of a 1D model is that it cannot describe angular effects of electron emission and that it is valid only for linearly polarized light. Moreover, the repulsion between electrons is overestimated due to the restriction of the electron motion to only one dimension. As a consequence, the final state electron momentum distributions differ from the experimental results (for details see [23]).
A comparison between 1D quantum mechanical and fully classical treatments of the electron dynamics in a strong laser field has shown, that the main dynamical features of double ionization of a quantum mechanical two-electron system are reproduced well, provided a classical ensemble of two-particle trajectories is used [106]. This indicates that the classical description of multiple ionization is a good approximation for more complex atomic systems in the classically allowed phase space.

Most theoretical approaches strongly support the recollision scenario for NSDI of atoms. However, till now only a few calculations have been done for the differential yield of the correlated final state electron momenta, which have been measured in COLTRIMS experiments [82, 90, 91, 100, 104]. Most of these calculations [82, 100, 104] have been done for the He atom, while experimentally correlated two-electron momentum distributions have been obtained only for Ar and Ne so far. Available theoretical results for Ar and Ne [90, 91] presently cannot explain the difference in the electron momentum correlations of these two atomic species found experimentally. Thus, on one hand experiments on He and, on the other hand, more sophisticated calculations for other atomic systems are desirable.

2.5 Free electron dynamics in the laser field

Since electrons driven by the oscillating electric field of a light wave play a key role in double ionization of atoms in strong laser fields, let us now consider the dynamics of a free electron in the laser field. We restrict ourselves to a classical description of an electron in linearly polarized light. This simplification is justified because NSDI is most efficient at linear polarization and most differential measurements have been performed under these conditions [16, 17, 18, 19, 68, 69, 73]. Moreover, for low-frequency ultra-short intense laser pulses both the classical analysis and the quantum mechanical treatment of double ionization lead to similar results [106].

We start with an electron which is ionized in the electric field of the light wave via tunneling in the first step of NSDI. For simplicity, we consider the electron motion in the strong field approximation, i.e. we neglect the electron interaction with the ionic core. A free electron in the electromagnetic field of a laser pulse ($\vec{E}$, $\vec{B}$) is exposed to the Lorenz force

$$\vec{F} = e(\vec{E} + \vec{v} \times \vec{B}), \tag{2.13}$$

with e the electron charge and $\vec{v}$ its velocity. Within the considered regime of NSDI with a light intensity of the laser field of about $10^{13}-10^{16}$ W/cm^2 and the wavelength of about 800 nm, the electron velocity v is small compared to c, the speed of light (nonrelativistic regime). This fact allows one to neglect the second term in (2.13) and take into account only the electric field of the light wave, which is then described as

$$\vec{E} = \vec{e}E_0(t)\cos\omega t, \tag{2.14}$$

where ω is the frequency of the field, $\vec{e}$ is a unit vector. In a linearly polarized light wave the electron experiences a force only along one axes parallel to the field

$$m\dot{v_x} = 0, \qquad m\dot{v_y} = 0, \qquad m\dot{v_z} = eE_0(t)\cos\omega t. \tag{2.15}$$

Let us assume that the electron starts from the position $z = 0$ at time t_0 with zero velocity. Tunneling occurs most probably near the top of the laser pulse which consists of few optical cycles (see Fig. 2.6). Here, the amplitude change $E_0(t)$ is very small after one optical cycle that is relevant for the electron return to the ion core. Thus after the integration of Eq. (2.15) we obtain the electron velocity along the field and the position of the electron z

$$v_z(t) = \frac{e}{m\omega}E_0(\sin\omega t - \sin\omega t_0), \tag{2.16}$$

$$z(t) = \frac{e}{m\omega^2}E_0(\cos\omega t_0 - \cos\omega t - \omega(t - t_0)\sin\omega t_0). \tag{2.17}$$

Whether the electron comes back to the ion or not depends on the initial time t_0 when the motion starts. In Fig. 2.7 (a) the position $z(t)$ of the electron is plotted

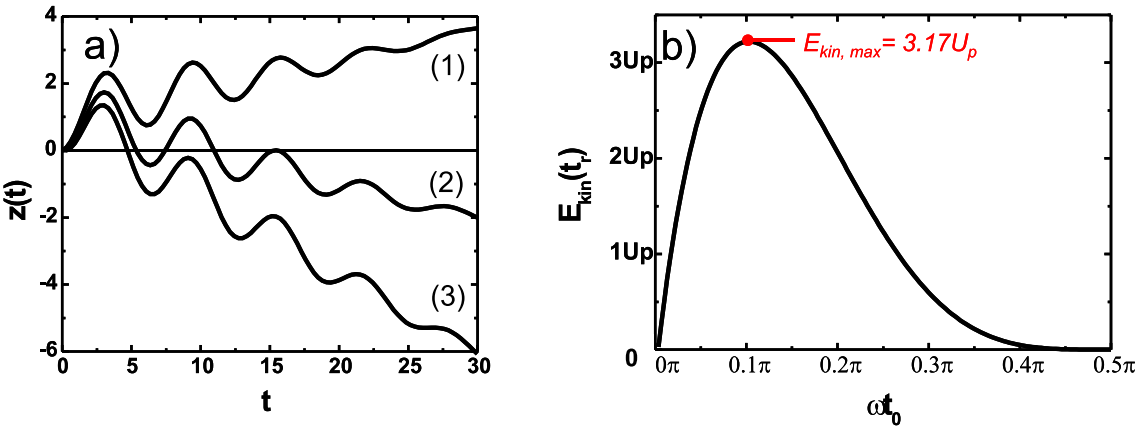

Fig. 2.7: a) Electron motion along the electric field of the light wave obtained from Eq. (2.17) for different t_0: (1) for an electron which does not return; (2) for a single and (3) for multiple electron returns. **b)** electron kinetic energy at the instant of rescattering t_r in terms of U_p as a function of t_0 [2].

for three different values of t_0. The latter have been chosen such that the electron never returns (1), returns once (3), or returns several times (2) back to the ion. Analyzing Eq. (2.17) for a certain t_0 we can obtain the return time t_r and then the corresponding electron kinetic energy E_{kin} using (2.16). The latter is an important parameter for collisional ionization. As is well known the mean quiver energy of a free electron in an electric field is given by the ponderomotive energy U_p (see (2.5)). For instance, the ponderomotive energy of a free electron in a laser field with a wavelength of 800 nm and with a light intensity of 10^{14} W/cm^2 is about 6 eV. The classical analysis considered here shows that the maximum kinetic energy an electron can gain upon recollision is $3.17U_p$ (see Fig. 2.7 (b)). If the maximum kinetic energy of the electron $E_{kin,max}$ is larger than the ionization potential of the parent ion I_p^+ **direct impact ionization** of a second bound electron can occur. Since $E_{kin,max}$ depends on the ponderomotive energy U_p and thus on the intensity of the light wave, an ionization threshold is expected to occur in the classical rescatterig picture at a certain intensity, where the electron kinetic energy reaches I_p^+.

Double ionization in a strong laser field upon inelastic recollision may happen in a second way: via **collisional excitation** of a bound electron, which is subsequently field ionized from the excited state, or alternatively, via **capture** of the recolliding electron into an excited state. The released energy leads to excitation of the bound electron. Finally, the two bound electrons get ionizied from their ecited states by the electric field of a light wave.

[2] Rottke in [112]

As mentioned above experiments on Ar indicate that impact excitation may contribute significantly to double ionization [69, 70]. Taking into account this mechanism also allows one to reproduce the double to single ionization yield ratio for He [96].

For the scenario with capture – field ionization the lifetime of the excited state has to be long enough to survive until both electrons can be freed simultaneously by the increasing electric field of the light wave.

After the two electrons are in the continuum, they oscillate and start to drift in the electric field of the light wave until the laser pulse has passed by. The remaining doubly charged ion moves in a similar way in the opposite direction.

Thus the final electron drift momentum for an e^- which starts with zero velocity is given by

$$p_z = -2e\sqrt{U_p(t_r)}\sin\omega t_r. \tag{2.18}$$

Namely this final electron momentum after the acceleration in the laser field can be measured in COLTRIMS experiments in coincidence with the drift momentum of the corresponding doubly charged ion.

In this chapter we have considered the fundamental aspects of ionization dynamics of atoms in intense laser fields based on the present knowledge of the subject from the experimental and theoretical point of view. We have also addressed the open questions and the perspectives for future theoretical as well as experimental investigations of the ionization dynamics of atoms and molecules in strong laser fields. In the next chapter we will concentrate on a detailed description of our experimental setup.

3. Experiment

In this chapter we consider in detail our experimental setup used for the present investigation. Our aim has been to study the ionization dynamics of atoms and molecules in an intense laser field.

The setup consists mainly of three parts: the atomic (molecular) gas-jet source chamber, differential pumping stages and the interaction chamber (Fig. 3.3). A supersonic atomic or molecular beam is formed in the gas-jet source chamber, it is collimated by apertures separating the differential pumping stages, and finally interacts in the main chamber with a focused laser beam. We will also discuss the momentum resolution of the spectrometer and the issue of light intensity determination in a focused laser beam.

3.1 Setup modifications

In the course of the present work the previously existing experimental setup has been significantly modified. In particular, a supersonic gas jet source together with a beam collimation system has been incorporated. Additionally, two turbomolecular pumps have been installed. Moreover, a new detection system has been integrated. The latter includes two position sensitive MCP detectors for ions and electrons as well as the data acquisition electronics which allows coincident detection of ion-electron pairs. A new software (CoboldPC) has been applyed for data acquisition and analysis.

3.2 The COLTRIMS technique

The experimental technique we used is based on COLTRIMS (Cold Target Recoil Ion Momentum Spectroscopy) (for a review see Ref. [15, 113]). It was developed from recoil-ion momentum spectroscopy (RIMS) [114, 115], a powerful tool for the investigation of the dynamics of atomic collision reactions, e.g. atoms interacting with electrons, ions or photons. It provides the possibility of high-resolution measurement of the recoil-ion momentum in combination with a large detection solid angle close to 4π. However, due to thermal motion a room-temperature static target limits the momentum resolution to a few atomic units. This corresponds to a kinetic energy

of ~ 40 meV. The realization of a cold supersonic gas-jet target in the COLTRIMS technique allowed one to achieve a momentum resolution of only a few per cent of 1 a.u. [1] corresponding to kinetic energies at the 1μeV level.

The combination of COLTRIMS with an electron imaging technique (based on the same principle as the recoil-ion detection), which is also known as "Reaction Microscope" [116], enabled the coincident detection of the momenta of recoil-ions and electrons, and thus, made possible a complete kinematical analysis of atomic or molecular reactions. In particular, the coincident ion-electron momentum spectroscopy was successfully applied to study the ionization dynamics of atoms in high-intensity laser fields [16, 17]. In the present work its application has been extended to molecular systems.

A reaction microscope includes a well collimated target beam of cold atoms or molecules, which interacts with a projectile beam (in our case a laser beam) at some point. After the interaction, the charged target fragments (ions and electrons) are extracted from the interaction region by a weak homogeneous electric field. After acceleration in opposite directions the ions and the electrons pass a field-free drift region until they reach position-sensitive microchannel plate (MCP) detectors [117]. From the detected time-of-flight (TOF) and the position of a fragment on the detector its momentum vector after the interaction can be reconstructed. The detailed description of our momentum spectrometer will be given below. Here we just note that the spectrometer geometry plays a decisive role for the momentum resolution.

3.3 The supersonic atomic and molecular jet

A spatially well localized atomic/molecular target is realized by supersonic expansion of gas from a high-pressure gas source into vacuum through a small nozzle. The important condition for a supersonic expansion is that the pressure ratio between the gas source and vacuum $P_0/P_v > 2.1$ [118].

In the free-jet isentropic expansion the free enthalpy h of the gas is converted into the kinetic energy of directed motion in the gas-jet[2]

$$h_0 - h = \frac{v^2}{2}, \tag{3.1}$$

where h_0 is the stagnation enthalpy per unit mass. During the expansion the gas cools down from the temperature of the gas source T_0 to some temperature $T \ll T_0$.

[1] 1 a.u. corresponds to the momentum of an electron bound in the ground state of a hydrogen atom.

[2] h is enthalpy per unit mass.

Tab. 3.1: Typical values of speed ratio S, temperature in the atomic/molecular beam T and the spread in momenta Δp under different experimental conditions.

Gas	T_0, K	P_0, bar	S	T, K	Δp, a.u.
Ar	300	1	12.9	4.5	1.4
	300	2	18.8	2.1	1.0
Ne	300	1	8.4	10.6	1.6
	77	1	22.7	0.4	0.3
N_2	300	1	6.0	29.0	3.0
	300	4	9.8	10.8	1.8
O_2	300	1	6.2	27.4	3.1
	300	4	10.2	10.1	1.9

For an ideal gas $dh = c_p dT$ and thus the squared velocity after the expansion is

$$v^2 = 2 \int_T^{T_0} c_p dT. \tag{3.2}$$

Taking into account $T \ll T_0$ and $c_p = (\gamma/(\gamma - 1)(R/W))$ for an ideal gas we obtain for the final jet velocity [118]

$$v = \sqrt{\frac{2R}{W} \left(\frac{\gamma}{\gamma - 1} \right) T_0}, \tag{3.3}$$

where R is the molar gas constant, γ is the specific heat ratio c_p/c_v and W is the molar molecular weight. For example, the mean velocity of Ar-atoms in the jet after expansion is 560 m/s at a source temperate $T_0 = 300$ K. This corresponds to a momentum of 18.6 atomic units.

The quality of the jet is characterized by the so-called speed ratio, $S = v/\sqrt{2kT/m}$, which is defined as the mean velocity divided by the thermal spread in velocities. Using Eq. (3.3) we get a simple expression for the speed ratio

$$S = \sqrt{\left(\frac{\gamma}{\gamma - 1} \right) \frac{T_0}{T}}. \tag{3.4}$$

The typical values of the speed ratio, the corresponding temperature in the jet after expansion from a nozzle of 20μm diameter, and the thermal spread in momenta in the atomic/molecular beam are presented in table 3.1 for target gases used in the experiment under different conditions (pressure P_0 and temperature T_0) of the gas

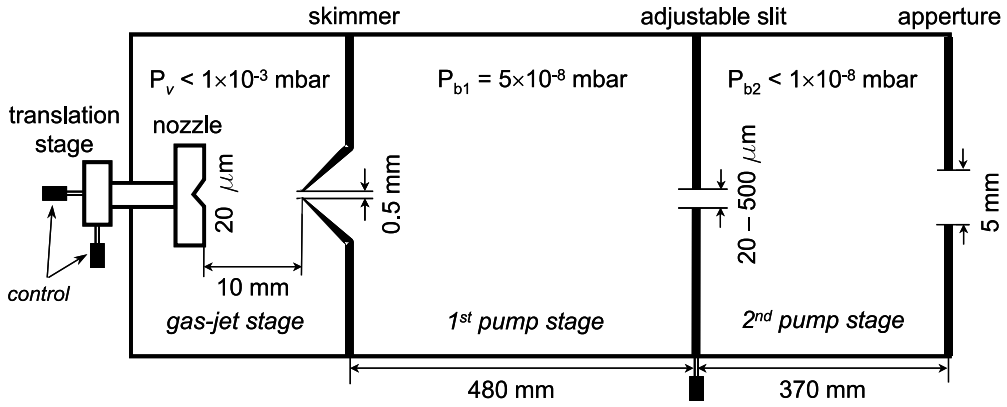

Fig. 3.1: Top view of the gas-jet chamber and the differential pumping stages.

jet source. Minimum spread in momenta of 0.3 a.u. is reached for neon as a target gas using a pre-cooled gas jet source (with liquid nitrogen at $T_0 = 77$ K) at $P_0 = 1$ bar.

The other characteristic parameter of the supersonic free-jet expansion is the Mach number. This is the mean flow velocity divided by the speed of sound

$$M = \frac{v}{\sqrt{\gamma RT/W}}. \tag{3.5}$$

For a supersonic expansion $M \gg 1$. The latter condition is also known as the "zone of silence", where the expansion properties become independent of the background gas pressure P_v in the vacuum chamber. The atomic/molecular beam is extracted from this region by a skimmer. The diameter and shape of the nozzle and the skimmer design determine the free-jet properties.

In our experiment a nozzle with a diameter of 20μm can be operated with the pressure of $1 - 20$ bar (usually, in experiment $1 - 2$ bar). The nozzle is mounted on a translation stage, which allows for the adjustment of the nozzle position in the plane perpendicular to the atomic beam axis (Fig. 3.1). The nozzle design enables cooling of the gas before expansion down to the temperature of liquid nitrogen.

A cone-shaped skimmer with a 0.5 mm diameter and a very sharp edge of the opening at the tip is located at a distance of 10 mm from the nozzle. The skimmer wall serves as a boundary between two differential pumping stages. The gas-jet chamber is pumped by two turbomolecular pumps with pumping speeds of 300 l/s and 500 l/s respectively. The background pressure in the jet chamber is smaller than 1×10^{-3} mbar when the beam source backing pressure is 1 bar.

Under certain conditions dimers, trimers or clusters may be formed in the gas-jet during expansion. The clustering depends on the gas used, the pressure P_0,

Tab. 3.2: Hagena parameters Γ and condensation parameters c for target gases in our experiment at the gas-jet source conditions $P_0 = 2$ bar and $T_0 = 300$ K.

Gas	Ar	Ne	N_2	O_2
c	1650	185	528	1400
Γ	90	10	28	76

the temperature T_0 in the beam source, and the diameter of the nozzle d. Cluster formation in a gas-jet can be estimated by using the semi-empirical scaling law of Hagena [119, 120, 121]:

$$\Gamma = c\frac{d[\mu m]^{0.85}P_0[mbar]}{T_0[K]^{2.29}} \tag{3.6}$$

where Γ is a dimensionless scaling parameter and c is the condensation parameter, which depends on the gas. The table below includes c values for the gases used in our experiment and the corresponding estimated maximum values of the Γ parameter. Based on available experimental data clusters start to be observed when $\Gamma = 100 - 300$. Therefore we do not expect any cluster formation under our experimental conditions ($T_0 = 300$ K, $P_0 = 1 - 2$ bar).

The formation of dimers and trimers for monoatomic gases can be avoided if the corresponding semi-empirical dimensionless parameters C and D do not exceed specific critical values [122, 123]

$$C \equiv \frac{P_0}{\varepsilon/\sigma^3}\left(\frac{d}{\sigma}\right)^{0.88}\left(\frac{T_0}{\varepsilon/k}\right)^{-2.3} < 15, \tag{3.7}$$

$$D \equiv \frac{P_0}{\varepsilon/\sigma^3}\left(\frac{d}{\sigma}\right)^{0.4}\left(\frac{T_0}{\varepsilon/k}\right)^{-2.4} < 0.1. \tag{3.8}$$

Here, ε and σ are gas-specific Lennard-Jones parameters. In our case the upper limits of the parameters for Ar are: $C = 11; D = 0.05$, and for Ne: $C = 1.5; D = 0.006$. At lower nozzle temperature ($T_0 < 160$ K) clusters form with higher probability. For example, at $T_0 = 162$ K and $P_0 = 2$ bar we detected singly charged Ar-dimers after multiphoton ionization in the reaction microscope.

Fig. 3.2 shows the ion yield dependence on the nozzle pressure P_0 for Ar^+ and Ne^+. The ion yield on the y-axis is measured using a ratemeter which counts the number of the singly charged ions per second detected by the MCP. It increases steeply at low pressure ($1-2$ bar). With the pressure increasing further the ion yield first becomes saturated ($P_0 : 2-4$ bar) and then decreases slightly ($P_0 > 4$ bar). The main reason for this behavior is scattering of the target jet on the background gas

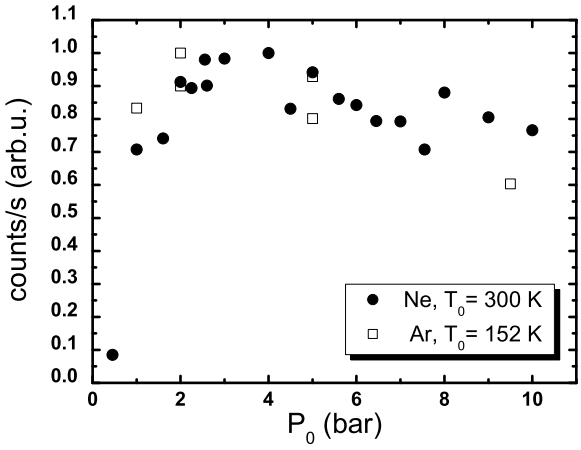

Fig. 3.2: Ion yield dependence on the gas source pressure for Ar^+ ions with pre-cooled nozzle ($T_0 = 152$ K) and for Ne^+ ions at room temperature.

in the gas-jet chamber at high pressure. This leads to a decrease of the gas density at the focal spot of the laser beam.

3.4 The Differential Pumping Stages

The first differential pumping stage is separated from the gas jet chamber by the supporting wall of the skimmer (Fig. 3.1). It is pumped by a turbomolecular pump with a pumping speed of 300 l/s. The background pressure in this stage is about 5×10^{-8} mbar. A small slit with adjustable width ($20 - 500\mu$m) and fixed hight of 3 mm is located at a distance of 480 mm from the skimmer. It collimates the atomic beam and thus determines the final momentum spread in the beam along the x direction (Fig. 3.3). The slit serves to separate the two differential pumping stages. The second stage (370 mm long) is pumped with an identical pump (300 l/s) as the first one. At the end of the second pumping stage there is an aperture with the diameter of 5 mm, which separates this stage from the main chamber. Finally, a well collimated atomic beam with low density enters the interaction chamber. At the point of interaction with the laser beam the gas density in the atomic beam is $\sim 10^9$ atoms/cm^3.

3.5 The momentum spectrometer

The momentum spectrometer employed in the experiment is schematically shown in Fig. 3.3. After passing the beam collimation chambers the cold atomic/molecular target beam (y-axis) intersects the focused laser beam (x-axis) at right angle in the center of the interaction chamber.[3]

The rest gas pressure in this chamber has to be as low as possible, to reduce the contribution from background gas ionization in the focused, high intensity laser beam. The base pressure in our ultra-high vacuum (UHV) chamber was kept at about 3×10^{-10} mbar using several pumps: a cryopump with the pumping speed of 1500 l/s, a turbopump with 500 l/s pumping speed and a couple of titanium sublimation pumps, which were operated from time to time.

The laser beam is focused onto the target atomic/molecular beam by a spherical mirror with a focal length of 100 mm in back reflection. The focal spot diameter in the focal plane is estimated to be 10μm [4]. The interaction volume is determined by the focal spot diameter and by the width of the atomic beam along the x-axis (laser beam propagation direction). It is approximately 2.5×10^{-9} cm^3. The atom/molecule density in the interaction volume is about $1.5 \times 10^9 - 3.5 \times 10^9$ cm^{-3}. Therefore the mean number of atoms/molecules in the interaction region is $3 - 8$. A low target density is important for coincident ion and electron momentum spectroscopy for reasons that will be discussed later.

After photoionization in linearly polarized 30 fs laser pulses, electrons and ions are accelerated in opposite directions (along the z-axis) in an applied static electric field with a field strength of $1 - 7$ V/cm. This electric field is generated by a system of twenty metal rings equally separated from each other. The applied voltage is equally divided between the rings so that the electric field is nearly homogeneous. After extraction by this field the charged particles are flying to their corresponding detectors in field-free tubes. They are detected with position-sensitive microchannel-plate (MCP) detectors.

The geometry of a whole flight tube is chosen such that we can reconstruct with high precision the initial momentum vector of the particle after ionization from its detected time-of-flight and its position on the detector. For ions the ratio between the length of the field-free drift path and the acceleration length was chosen as 2 : 1 (0.2 m and 0.1 m respectively). The lengths ratio for electrons in our experiment was 1 : 1 (0.1 m for each).

Electrons emitted from the focal spot with a large kinetic energy into a large solid angle usually miss the detector. The application of a weak homogeneous magnetic field parallel to the extraction electric field allows one to detect high-energy electrons

[3] This coordinate system will be used throughout the work.

[4] FWHM of a Gaussian function

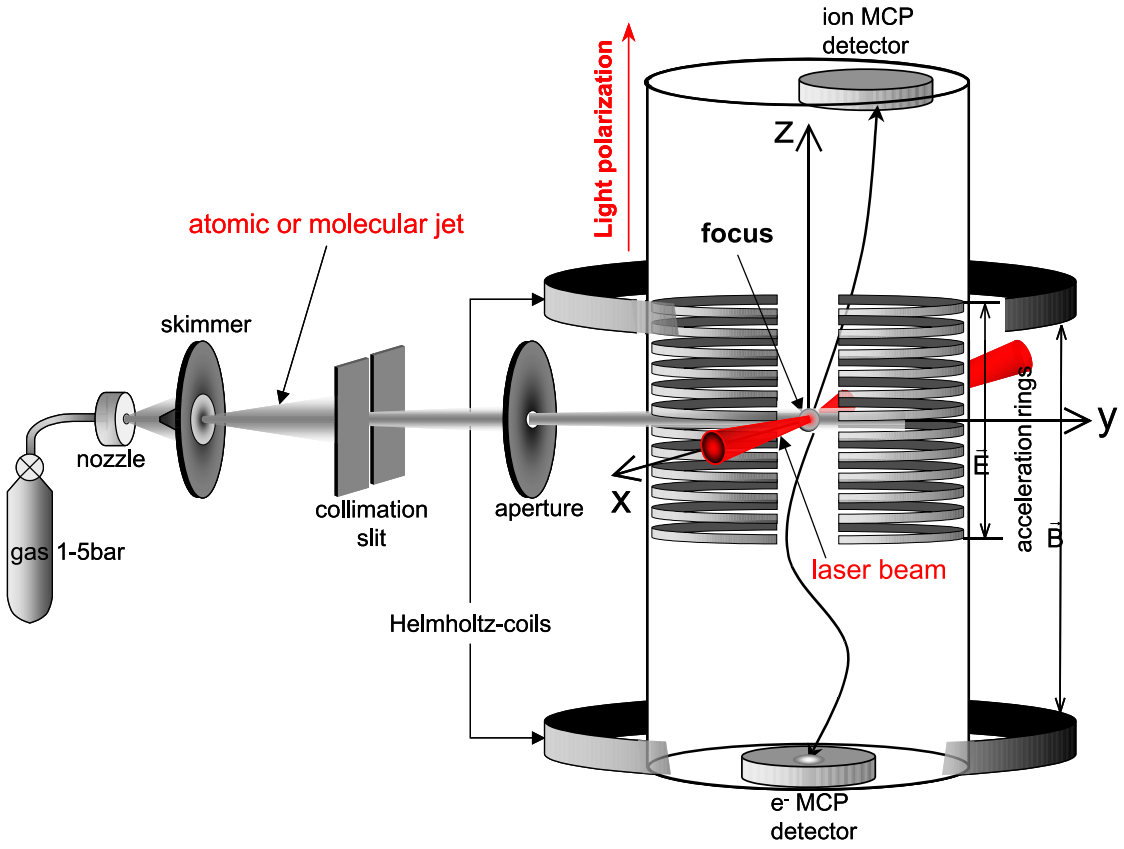

Fig. 3.3: Schematic view of the momentum spectrometer including the supersonic atomic (molecular) jet.

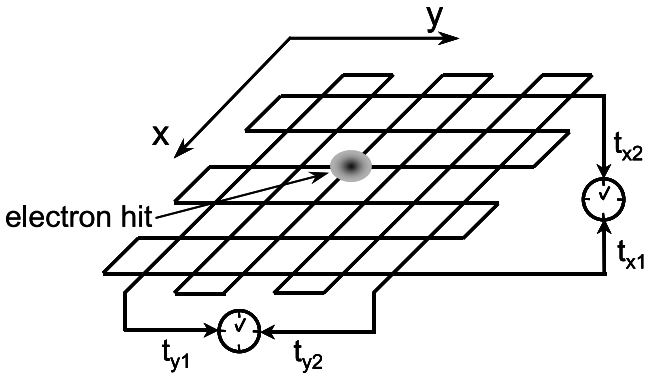

Fig. 3.4: Operation principle of the delay-line anode: signals from the electron avalanche arrive at two ends of each delay-line (x and y); the time difference between them is measured (symbolized by the clocks).

emitted within a solid angle of up to 4π. This magnetic field is generated by a couple of Helmholz-coils. By adjusting the distance between the coils equal to their radius a sufficiently homogeneous magnetic field can be achieved in a quite large spatial region. In our experiment the radius of the magnetic field coils was 0.42 m and the magnitude of the magnetic field reached $4 - 20$ G. The deviation from homogeneity of the magnetic field $\frac{\Delta B}{B}$ over the flight path of the electron from the laser focal spot to the electron detector is less than 1%. The influence of the magnetic field on electrons and on ions is defined by the Lorenz-force $\vec{F} = q[\vec{v} \times \vec{B}]$. However, for an electron and an ion with the same momentum, for instance 1 a.u., the corresponding velocity of the ion (e.g. Ar^+), and therefore the Lorenz-force, is 1.4×10^{-5} times smaller than that of an electron. In fact we can neglect the influence of the magnetic field on ions.

Both, electrons and ions, are detected with identical commercial position-sensitive MCP detectors [124]. Their active detection area is 80 mm. Each detector consists of a pair of micro-channel plates (MCP) where the time-of-flight of the charged particle is picked off, and a delay-line anode for position decoding. An optimal MCP detection efficiency is achieved for ions at a kinetic energy of 2.2 keV and for electrons at 200 eV. An avalanche of secondary electrons emerging from the MCP creates a signal on the delay-line anode. The time resolution is limited only by the electronics used usually to 0.5 ns. A delay-line anode consists of two couples of parallel wires wound spirally in many turns along two directions perpendicular with respect to each other. Fig. 3.4 shows the detection principle of a delay-line anode. The position is decoded from the arrival time difference of the signal an electron cloud induces in the wire at both ends of the corresponding line. Both coordinates x and y can be

calculated as [112]

$$x = (t_{x1} - t_{x2})v_{signal}, \tag{3.9}$$

$$y = (t_{y1} - t_{y2})v_{signal}, \tag{3.10}$$

where $(t_{x1} - t_{x2})$ and $(t_{y1} - t_{y2})$ are the respective time differences and v_{signal} is the signal velocity. The latter can be determined from the time a signal needs to travel from one end of the line to the other one (for our detector about 1 mm/ns). A position resolution of 0.25 mm is achieved with a time resolution of 0.5 ns of the time-to-digital converter we used.

The timing signals from each MCP and the corresponding delay-line anode are amplified by means of a differential amplifier (RoentDek DLATR6), converted to standard ECL pulses by constant fraction discriminators, and then measured by a fast time-to-digital convertor (TDC) with a time resolution of 0.5 ns (LeCroy TDC 3377). Additionally the ion time-of-flight and position were measured by a second TDC (Philips Scientific 7186) with a higher resolution of 100 ps. The signal from the laser pulse served as the reference time for each event. Since the electron time-of-flight is typically less than 500 ns and the ion TOF amounts to several tens of microseconds, the ion TDC was started by a suitably chosen high precision constant time delay after an electron arrived at the electron MCP. Data from the TDCs were only accepted by the data acquisition system if at least one electron and one ion reached the respective MCP within a laser shot. The TDCs used were integrated in a CAMAC crate. The data were read out by a CAMAC controller, which was connected to a PC via an interface card. By means of a special commercial software "CoboldPC" (ReontDek Handles GmbH) we controlled the data acquisition and stored the raw data in a so-called List-Mode-File (LMF) event by event. This allows one to replay an experiment off-line. CoboldPC also enables the full data analysis and graphic representation of the analyzed or raw data. A typical ion TOF spectrum for argon as a target gas is presented in Fig. 3.5. Beside the main peaks of the three Ar^+ isotopes and Ar^{2+}, arising from ionization of the Ar gas jet in the laser focus, other peaks are found. The quite broad peaks of O^+, N_2^+, and H_2O^+ originate from photoionization of the background gas. The sharp lines of O_2^+ and H_2O^+ come from ionization of the gas jet, which was not entirely consisting of Ar atoms. Moreover, due to the high repetition rate of the laser pulses (100 kHz), atoms/molecules are ionized every 10μs. This gives rise to the peaks $(Ar^+)^*$, $(Ar^{2+})^*$, and $(H_2O^+)^*$ coming from the previous/next laser pulse, and thus repeating their respective actual peaks with a time difference of 10μs. The ion and electron position images are shown in Fig. 3.6. Ar^+ and Ar^{2+} ions (Fig. 3.6 (a)) can be identified as the two maxima extended along the x-axis, i.e. the direction of the atomic beam. In the projection onto the detector plane, ions start their motion from the point C (laser beam focal spot) and move along the arrow until they hit the detector. Electrons move helically in the applied magnetic and electric fields. In the detector plane an electron trajectories is

a circle, C is the starting point (Fig. 3.6 (b)). As mentioned above we detect only one electron and one ion per laser shot. The data acquisition is initiated only if both signals are detected.

Ultimately, for double ionization, in our experiment the momentum of a doubly charged ion and that of one of the two photoelectrons are measured. The momentum

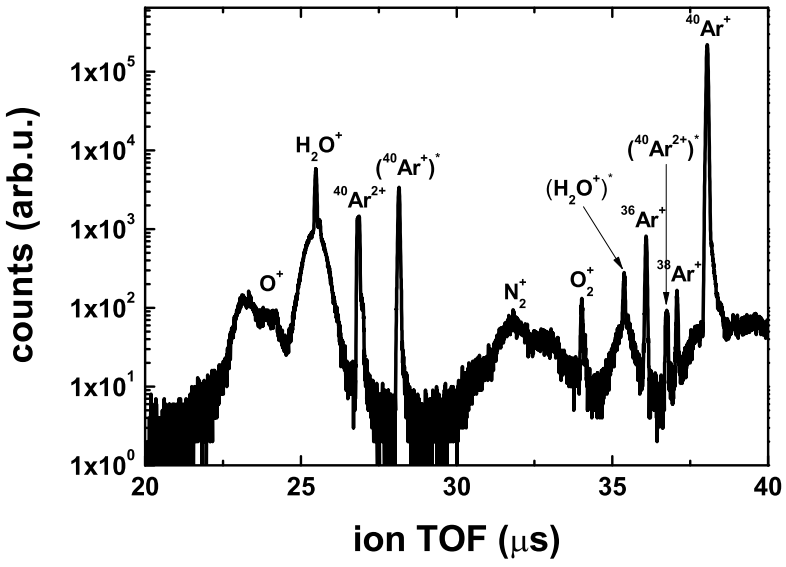

Fig. 3.5: Typical ion TOF spectrum obtained from strong field ionization of Ar as target gas using a Ti:Sa laser system at a light intensity of 1.5×10^{14} W/cm^2. An explanation for every peak is given in text.

of the second electron can be calculated from the momentum conservation law

$$\vec{p}_A + n\hbar\vec{k} = \vec{p}_{i^{++}} + \vec{p}_{e1} + \vec{p}_{e2}. \tag{3.11}$$

A neutral atom A absorbs effectively n photons each with a momentum $\hbar\vec{k}$. The momentum of one photon at 800 nm wavelength is 4.15×10^{-4} atomic units. This is small compared to the typical experimental momentum resolution. Depending on the ionization potential and the final charge state of the ion from several tens up to several hundreds of photons are absorbed by a target atom. But even for 200 effectively absorbed photons the whole photon momentum transfer (0.08 a.u.) is still smaller than our accuracy of ion momentum determination (see below). Therefore we can exactly calculate, within the spectrometer resolution, the momentum of the

second electron from the measured momenta of the doubly charged ion and one of the two photoelectrons

$$\vec{p}_{e2,z} = -(\vec{p}_{i^{++},z} + \vec{p}_{e1,z}), \tag{3.12}$$

$$\vec{p}_{e2,x} = -(\vec{p}_{i^{++},x} + \vec{p}_{e1,x}), \tag{3.13}$$

$$\vec{p}_{e2,y} = -(\vec{p}_{i^{++},y} + \vec{p}_{e1,y}) + \vec{p}_{A,y}. \tag{3.14}$$

Here, it has been taken into account that the initial momentum components of the atom in the well collimated atomic beam are negligibly small along the x and z axes. For instance, for Ar as a target gas, with the temperature of the gas source 300 K and the pressure 1 bar, the maximum momentum in the jet along x-axis is estimated to be 2.8×10^{-4} a.u. and 9×10^{-5} a.u. along the z-axis. For the atomic beam direction (y-axis) we cannot neglect the momentum of the neutral atom and the residual thermal momentum spread in the beam. Even in a pre-cooled (77 K) target jet the momentum of an atom is about 9 a.u. Fig. 3.6 (a) shows the two-dimensional ion image on the detector. Ar^+ and Ar^{2+} ions created in the jet are resulting in two maxima extended in the x direction on the right side of the detector. The spectrum is observed at an atomic beam source temperature of 300 K and a pressure of 1 bar. At these conditions the thermal velocity distribution of atoms in the beam results in a quite large momentum spread of ions along the beam propagation direction (x-axis) of 2 a.u. for Ar^+ ions and 3 a.u. for Ar^{2+}. The spread in momenta along the y-axis, which is actually determined in the ionization event, is much narrower: 0.6 a.u. for Ar^+ and 1.1 a.u. for Ar^{2+}. This can be obtained from Fig.3.6 (a) if one divides the widths of the x and y coordinate distributions by the corresponding ion TOF.

The calculation of the momentum of one electron from the measured momenta of the other electron and of the doubly charged ion is problematic because we cannot decide whether the detected ion-electron pair arose from one double ionization event or not. The best solution of this problem would be to ensure that only one atom/molecule is ionized per laser shot. As was mentioned before, there are $3 - 8$ target atoms/molecules in the interaction volume in our experiment. The experimental conditions were chosen such that the repetition rate of the laser pulse was 100 kHz with 8000 photoelectrons detected per second (i.e. 8 kHz measured by a ratemeter during the experiment). It follows that the probability to ionize one atom per laser shot and to detect the corresponding electron is not higher than 0.08. Under these conditions the contribution from false ion-electron coincidences can be estimated to be about 8%. This value can be derived from the momentum conservation for single ionization, where the narrow peak around zero due to true coincidences ($p_{i^+,z} + p_{e,z} = 0$) is sitting on the broad background resulting from false coincidences. Integrating over the main peak and over the background we obtain the number of true and false events.

The momenta of the detected ions and electrons are calculated from their measured time-of-flight and from the positions where the particles hit the detectors using a classical analysis of their motion in the extraction electric field $\vec{E}$ and in the homogeneous magnetic field $\vec{B}$ for electrons

$$m_i\ddot{\vec{v}} = q\vec{E}, \tag{3.15}$$

$$m_e\ddot{\vec{v}} = e\vec{E} + e[\vec{v} \times \vec{B}]. \tag{3.16}$$

Since both the electric and the magnetic fields are directed along the z-axis (Fig. 3.3) the electron motion along z-axis is determined by the electric field only while in the xy-plane the magnetic field alone acts on the electron

$$m_e\dot{v}_z = -eE, \qquad m_e\dot{v}_x = ev_yB, \qquad m_e\dot{v}_y = -ev_xB. \tag{3.17}$$

From a classical calculation for an electron and an ion which first move in a homogeneous electric field and then in a field-free space we obtain the relation between the time-of-flight to the detector and the initial momentum component parallel to the extraction electric field $p_\parallel$ (along the z-axis). Thus for electrons

$$T_e = \frac{p_{e\parallel}}{eE} + \frac{\sqrt{2m}}{eE}\sqrt{eEl + \frac{p_{e\parallel}^2}{2m}} + \frac{L\sqrt{2m}}{2\sqrt{eEl + \frac{p_{e\parallel}^2}{2m}}}, \tag{3.18}$$

where l is the length of the acceleration stage, L the length of the field-free tube and E the electric field strength. The corresponding time-of-flight for ions is

$$T_i = -\frac{p_{i\parallel}}{qE} + \frac{\sqrt{2m}}{qE}\sqrt{qEl + \frac{p_{i\parallel}^2}{2m}} + \frac{L\sqrt{2m}}{2\sqrt{qEl + \frac{p_{i\parallel}^2}{2m}}}, \tag{3.19}$$

where q is the ion charge. In the experiment with the above-mentioned parameters ($E : 1 - 7$ V/cm, $l : 10$ cm) we usually have for ions the condition

$$\frac{p_\parallel^2}{2m} \ll qEl. \tag{3.20}$$

Expanding Eq. (3.19) into a Taylor-series with respect to $p_{i,\parallel}^2/(2mqEl)$ we obtain

$$\begin{aligned} T_i = &-\frac{p_{i\parallel}}{qE} + \frac{\sqrt{2m}(2l+L)}{2\sqrt{qEl}} + \left(\frac{p^2}{2mqEl}\right)\frac{\sqrt{2m}(2l-L)}{4\sqrt{qEl}} \\ &+ \left(\frac{p^2}{2mqEl}\right)^2\frac{\sqrt{2m}(3L-2l)}{16\sqrt{qEl}} + \left(\frac{p^2}{2mqEl}\right)^3\frac{\sqrt{2m}(6l-15L)}{96\sqrt{qEl}} + \ldots \end{aligned} \tag{3.21}$$

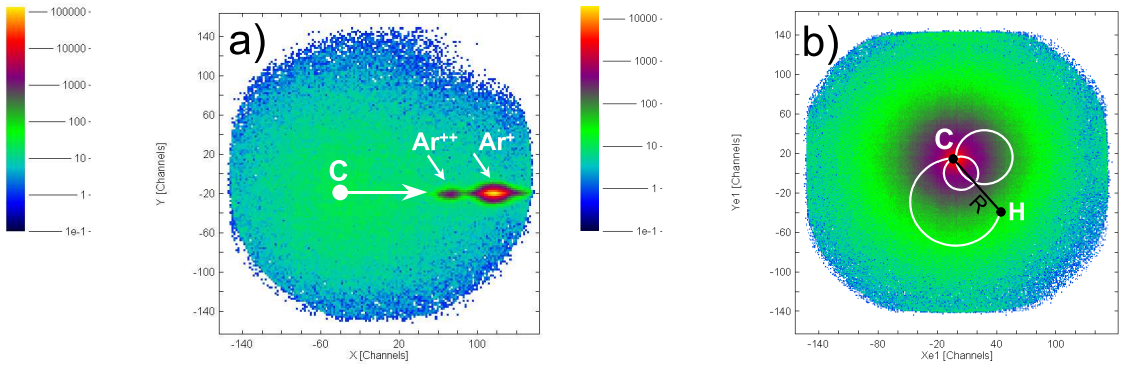

Fig. 3.6: Two-dimensional position images showing the position distributions for ions (a) and for electrons (b) where they hit their detectors.

Furthermore, as we mentioned before, for ions the field-free path L is twice as long as the path l in the acceleration electric field. Therefore the third term in Eq. (3.21) vanishes. Finally, we have

$$T_i = 2\sqrt{\frac{2ml}{qE}} - \frac{p_{i\|}}{qE} + \varnothing\left(\left[\frac{p_{i,\|}^2}{2mqEl}\right]^2\right), \tag{3.22}$$

where only the first two terms are significant. Thus, under our experimental conditions, the ion time-of-flight depends almost linearly on the momentum of the ion after photoionization.

An electron in a magnetic field cycles with a cyclotron frequency $\omega = (eB)/m_e$. In the xy-plane it moves along a circle starting at point C (laser beam focal spot) and hitting the detector at H (Fig. 3.6 (b)). The initial momentum of the electron in the xy-plane ($\vec{p_{e\perp}}$) determines the length of the helical trajectory. As an example, Fig. 3.7 shows twelve typical electron trajectories at an extraction electric field $E = 250V/m$ and magnetic field $B = 5G$ obtained using the simulation program SIMION. Electrons are emitted from the focal spot with a kinetic energy of $12eV$ and an emission angle which is varying from 0 to 360 degree (in xz-plane). The momentum component of an electron $\vec{p}_{e\perp}$ perpendicular to magnetic field $\vec{B}$ (which coincides with the light polarization direction) can be calculated if we know the time-of-flight of the electron T_e, the cyclotron frequency ω and the distance R from the electron starting point C to its end point at the detector H

$$|\vec{p}_{e\perp}| \times 2\,|\sin\frac{\omega T_e}{2}| = m_e\omega R, \tag{3.23}$$

where $R = \sqrt{(x-x_C)^2 + (y-y_C)^2}$. Here, (x, y) are actual coordinates of an electron at the detector and (x_C, y_C) can be obtained from the maximum C of the

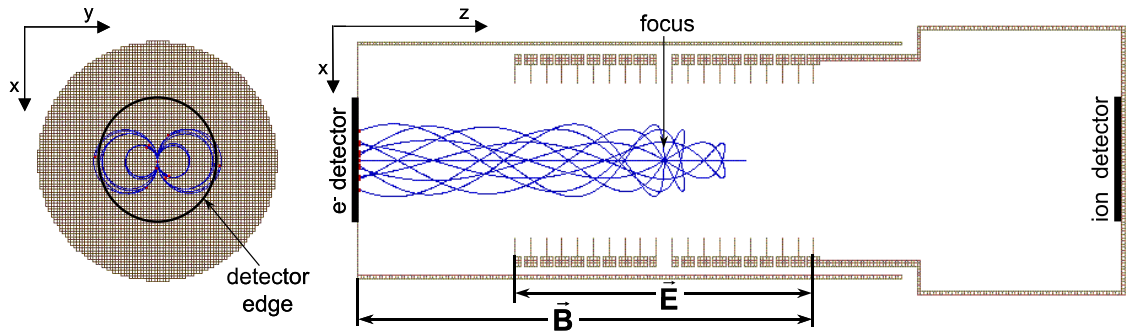

Fig. 3.7: Electron trajectories at an extraction electric field $E = 250V/m$ and a magnetic field $B = 5G$ in xy-plane (left) and in xz-plane (right). Red points are the end points of the trajectories, where the respective electron hits the detector surface.

electron position image. Many electrons in Fig. 3.6 (b) start and arrive at the detector at the same point flying an integer number of cycles $\omega T_e = 2n\pi, n = 0, 1, 2, ...$ This can be seen in Fig. 3.8, where R is plotted versus the electron time-of-flight. The two maxima at $R = 0$ correspond to electrons with closed trajectories. At these points we cannot resolve $\vec{p}_{e\perp}$ since the sin term, and thus R in Eq. (3.23) become zero. The cyclotron frequency ω is easily determined from the time difference between two points with $R = 0$ where the number of events is maximum (Fig. 3.8).

The ion momentum component transverse to the extraction electric field, which coincides with the light polarization direction, can be obtained from the position of the ion on the detector (Fig. 3.6 (a)). Ions with a transverse momentum $p_{i\perp} = 0$ arrive at the detector in the center of the corresponding ion distributions (Ar^+ or Ar^{2+}). Therefore the ion momentum components along the x and y axes can be calculated using the coordinate distribution and the corresponding TOF of the ion

$$p_{i,x} = \frac{x - x_c}{T_i} m_i, \tag{3.24}$$

$$p_{i,y} = \frac{y - y_c}{T_i} m_i, \tag{3.25}$$

where x and y are actual coordinates of the ion on the detector, T_i is its time-of-flight and m_i is the ion mass. x_c and y_c correspond to the center of the respective coordinate distributions (Ar^+ or Ar^{2+}). In general, the transverse ion momentum is a sum of the momentum of the respective atom in the atomic gas jet p_A and the momentum transfer δp through photoionization

$$p_{i,x} = p_{A,x} + \delta p_x, \tag{3.26}$$

$$p_{i,y} = p_{A,y} + \delta p_y. \tag{3.27}$$

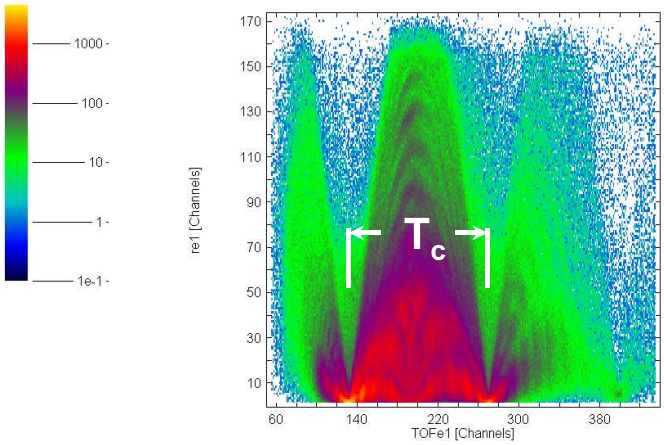

Fig. 3.8: Cyclotron deflection R versus the electron TOF. The period of the a cycle is $T_c = 2\pi/\omega$.

The momentum component $p_{i,y}$ is mainly determined in the ionization event, since $p_{A,y}$ in a well collimated beam propagating along the x-axis is negligibly small. Thus, $p_{i,y} = \delta p_y$ with uncertainty 5.7×10^{-4} a.u.[5]. This is much smaller than the typical measured values of $p_{i,y}$. As can be seen in Fig. 3.6, the ion coordinate distribution along the x-axis is much broader than that along y. This indicates that the $p_{i,x}$ momentum distribution, in contrast to $p_{i,y}$, is determined by the remaining thermal momentum distribution of atoms in the jet $p_{A,x}$. The latter cannot be neglected.

3.6 Momentum resolution

In general, the ion momentum resolution is determined by the time-of-flight ($0.5ns$) and the position resolution (0.26 mm for each delay-line). It also depends on the target jet quality. The ion and electron momentum resolution in the longitudinal direction with respect to the light polarization direction also depends on the extraction voltage. Similarly, the transverse momentum resolution for electrons depends on the magnitude of the applied magnetic field. The longitudinal ion momentum resolution can be derived from the momentum conservation condition for single ionization. A sharp peak at zero momentum is expected for the sum-momentum $(p_{i\parallel} + p_{e\parallel})$. The density plot of the latter versus the electron longitudinal momentum $p_{e\parallel}$ (Fig. 3.9 (a)) yields some useful information. A narrow distribution around zero of the sum-momentum is observed. The width of the distribution depends mainly

[5] this value is estimated using Eq. (3.3) and taking into account the jet geometry in the experiment

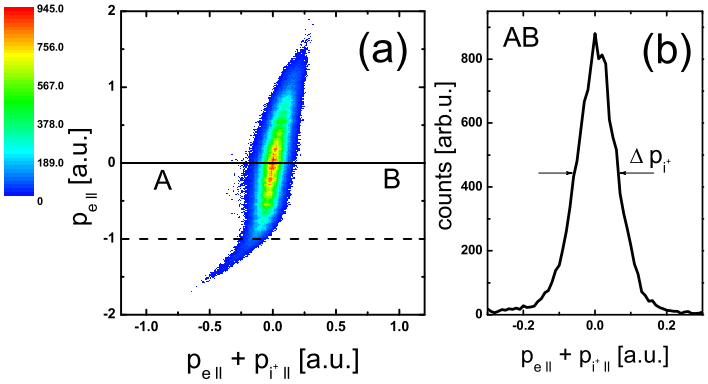

Fig. 3.9: (a) The momentum conservation of single ionization of Ar parallel to the light polarization direction represented as a density plot of $(p_{i\|} + p_{e\|})$ versus $p_{e\|}$; (b) cut AB through the two-dimensional distribution in (a) along the line $p_{e\|} = 0$.

on the ion momentum resolution when the electron momentum is equal zero. Thus we can estimate $\Delta p_{i\|}$ from a cut through the two-dimensional distribution along the line $p_{e\|} = 0$ (Fig. 3.9 (b)). The width of this distribution (FWHM) is about 0.12 a.u. This value can be taken as the upper limit for $\Delta p_{i\|}$. The deviations from $(p_{i\|} + p_{e\|}) = 0$ for $p_{e\|} \geqslant 1$ a.u. (Fig. 3.9 (a)) indicates that the extraction electric field is not entirely homogeneous and thus the TOF - momentum transformations (3.18) and (3.19) are not exact. The deviations for $p_{e\|} \leqslant -1$ a.u. occur due to high-energy electrons starting into the direction opposite to the electron detector. These electrons are flying up to the edge of the applied electric field, where the field is inhomogeneous.

Fig. 3.10 shows the scalar potential of the extraction field throughout the yz-plane of the spectrometer and a comparison with the extraction potential of an ideally homogeneous field along the z-axis ($y = 0$), which was used to derive the ion and electron TOF in (3.19) and (3.18), respectively. It is evident that the main difference between the ideal and real scalar potentials appears at the transition between the extraction region and the field-free drift part ($z = 100$ and 300 mm). The real field distribution in the spectrometer was determined by means of the "SIMION 3D" simulation program [125]. In SIMION electrostatic or static magnetic fields are computed by solving the corresponding Laplace equations. The program also allows one to simulate the motion of any charged particle in an electric or/and magnetic field of a given geometry. In Fig. 3.11 we compare the TOF dependence on the initial momentum for ions and electrons derived from the SIMION simulation

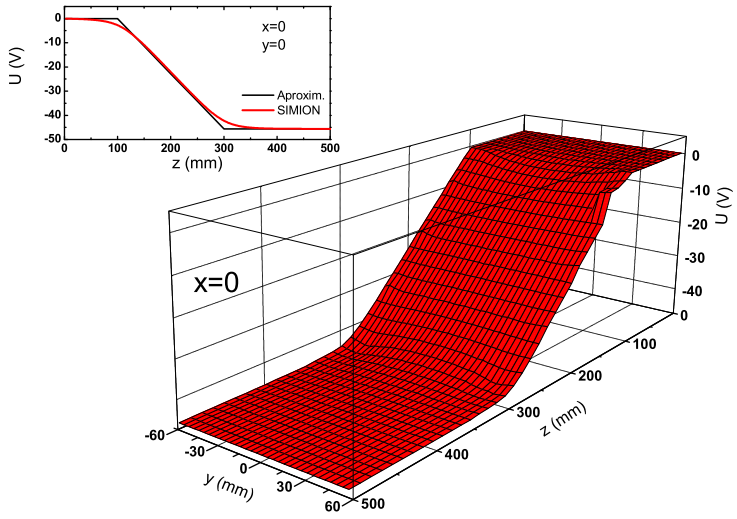

Fig. 3.10: The scalar potential of the extracting electric field in the yz-plane and along z-axis (small graph) of the spectrometer derived from the SIMION simulation for the real spectrometer geometry. It is compared with the ideal extraction potential (black curve in the small graph) used in Eqs. (3.18) and (3.19).

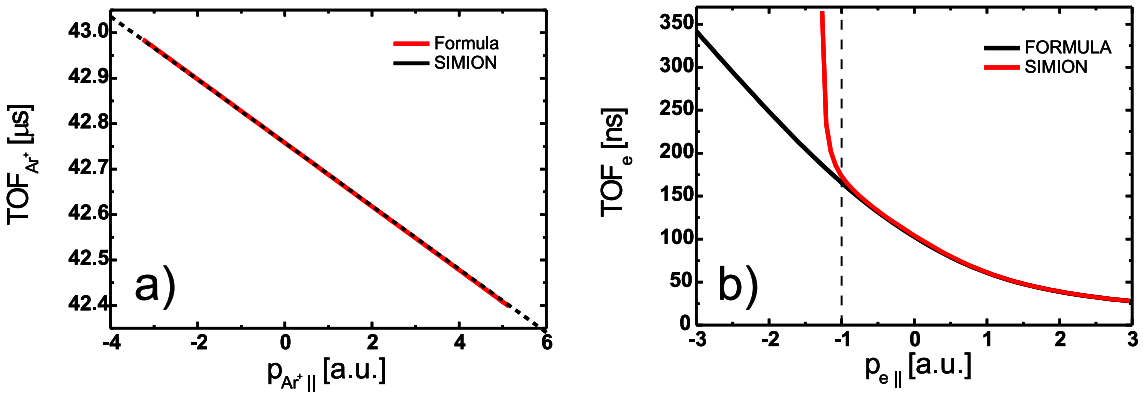

Fig. 3.11: Comparison of the TOF dependence on the initial momentum derived from a SIMION simulation (red curve) and calculated from (3.18) and (3.19) (black curve): (a) for ions; (b) for electrons.

on one hand and from calculations with the formulae (3.18), (3.19) on the other hand. For ions the results coincide. But for electrons emitted with large negative momenta (backward from the detector) the discrepancy is quite strong for $p_{e\|} < -1$ a.u., which is marked as a dashed line in Fig. 3.11 (b). The consequence of this discrepancy can also be seen in Fig. 3.9 (a) as a deviations from zero momentum for $p_{e\|} \leqslant -1$ a.u. as discussed above.

Since the essential discrepancy for the TOF-momentum dependency appears for $p_{e\|} < -1$ a.u. we can use the formula (3.18) in a limited range of momenta for an estimation of the resolution in the longitudinal electron momentum. The momentum resolution is mainly determined by the resolution in time-of-flight (0.5 ns). It therefore depends on the electron momentum $p_{e\|}$ (Fig. 3.12). $\Delta p_{e\|}$ is almost constant for electrons emitted with negative momenta (better than 0.01 a.u.) and degrades for positive momenta up to 0.06 atomic units.[6] The same momentum resolution dependence has been obtained by the SIMION simulations (red curve in Fig. 3.12).

For ions, the effect of the extraction field inhomogeneity is that the ion TOF does not depend on the longitudinal momentum alone (3.19) but becomes a function of both $p_{i\|}$ and $p_{i\perp}$. Fig. 3.13 clearly demonstrates the dependence of $p_{i\|}$ on the position on the detector, and thus on $p_{i\perp}$ for Ar^+ ions. The left pannel of Fig. 3.13 shows the distribution of Ar^+ ions on the detector where the equal narrow areas at three different coordinates $x_i, (i = 1, 2, 3)$ are marked. On the right side of Fig. 3.13 the momentum distribution $(p_{e\|} + p_{i\|})$ is plotted at $p_{e\|} = 0$ (similar to Fig. 3.9 (b)) only

[6] In Fig. 3.11 (b) and Fig. 3.12 electrons with positive momenta are emitted towards the electron detector and those with negative momenta start in the opposite direction.

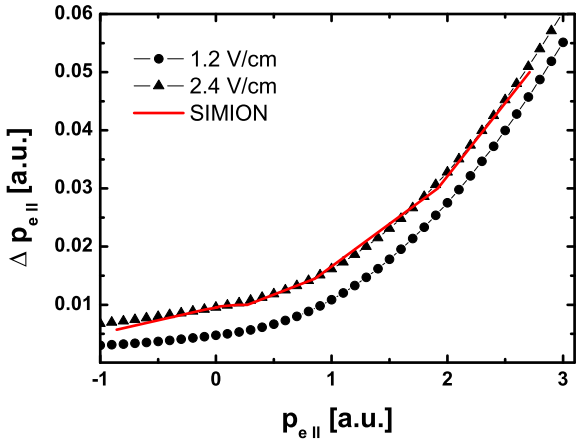

Fig. 3.12: Electron momentum resolution estimated using Eq. (3.18) for two acceleration electric field strengths: 1.2 V/cm and 2.4V/cm; comparison with the SIMION simulations (red curve).

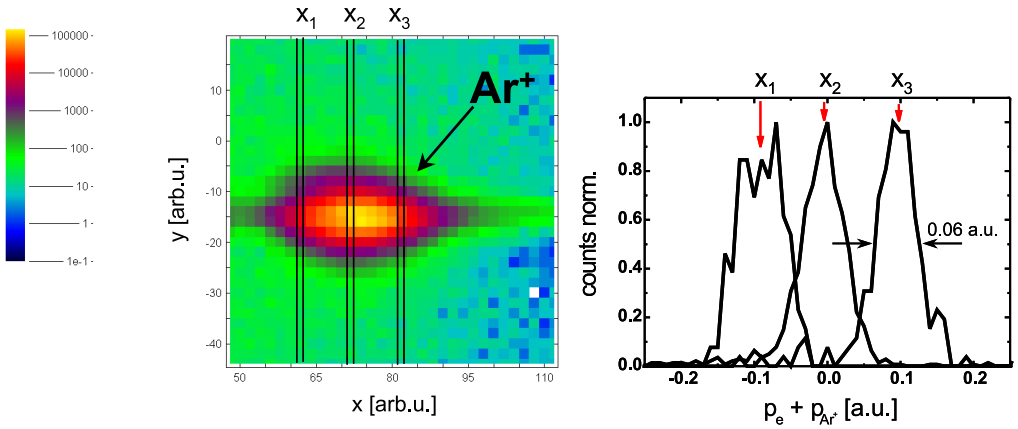

Fig. 3.13: Left: two-dimensional ion image for Ar^+ ions; right: sum-momentum $p_{e\|} + p_{Ar^+\|}$ at $p_{e\|} = 0$ (identical to Fig. 3.9 (b) for three different positions x_i on the ion detector image.

for those Ar^+ ions which hit the detector within one of these three narrow areas. As can be seen, the $(p_{e\|} + p_{i\|})$ distributions resulting from the different x positions on the detector are slightly shifted. Furthermore, the width of the $(p_{e\|}+p_{i\|})$ distribution (0.06 a.u.) is just half of that in Fig. 3.9 (b), which is integrated over all x coordinates. As we discussed before (Fig.3.9) the width of $(p_{e\|}+p_{i\|})$ at zero electron momentum is a measure of the ion momentum resolution $\Delta p_{i\|}$. Thus, the ion momentum resolution can be amended by improving the electric field homogeneity over the spectrometer volume traced out by the ion trajectories.

The electron momentum resolution in the transverse direction is determined by the position uncertainty resulting from the detector resolution and the target size. We can estimate it using Eq. (3.23) and taking into account that the position resolution in the detector plane is 0.36 mm (using a LeCroy TDC). The best momentum resolution (better than 0.01 a.u.) is obtained for electrons with a time-of-flight, which corresponds to $\sin\frac{\omega T_e}{2} = 1$. However, this momentum resolution degrades when the electron time-of-flight approaches an integer multiple of the cyclotron period $T = 2\pi/\omega$. At these times the resolution is lost completely.

The ion momentum resolution in the transverse direction acquired from the SIMION simulations is about 0.18 atomic units. It is obtained without taking into account the extension of the interaction volume. The real transverse momentum resolution for ions is worse than this value.

3.7 The laser system

We used a Ti:Sapphire laser system in our experiment to irradiate the atoms and molecules. It consists of a Ti:sapphire oscillator, a spatial light modulator (SLM), a regenerative amplifier, and a prism compressor (Fig. 3.14). The detailed description of the laser system can be found in Ref. [126]. Unlike the conventional chirped-pulse amplification technique (pulse stretching-amplification-recompressing) used for high peak-power ultrafast lasers [3, 127], the present system does not include a pulse stretcher. Instead, pulse broadening occurs due to accumulation of a large amount of dispersion during the amplification process.

The laser pulses are generated in a Kerr-lens mode-locked Ti:Sapphire oscillator with a repetition rate of 78 MHz and a mean output power of 200 mW. This corresponds to a pulse energy of $\sim$ 3 nJ. The output pulse width of the oscillator is about 30 fs.

A liquid-crystal phase modulator (SLM) serves for the pre-compensation of high-order dispersion, while the main part of dispersion (second and third orders) is compensated after amplification by the prism compressor. Without the SLM the pulse width after the compressor is limited to 60 fs. Fig. 3.15 represents the non-collinear autocorrelation curves of the amplified pulse with and without the SLM [126]. The

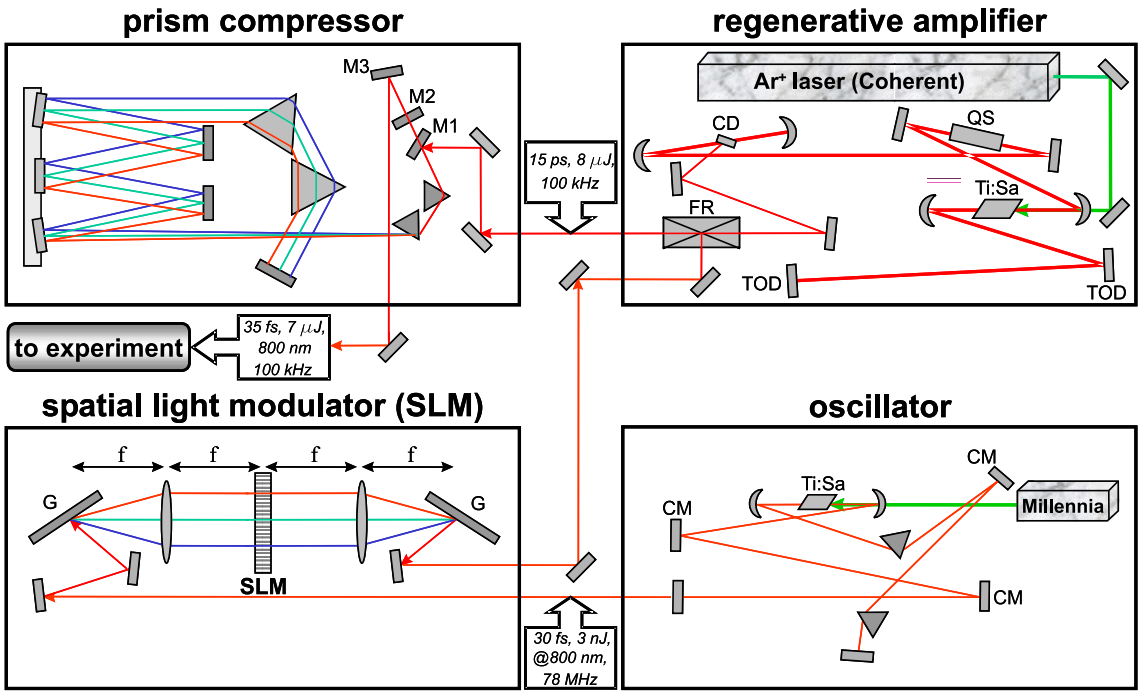

Fig. 3.14: Diagram of the Ti:Sa laser system used in the experiment [128]. FR - Faraday isolator; QS - Q switch; CD - cavity dumper; TOD - chirped mirrors to control third-order dispersion; CM - chirped mirror; G - grating.

pulse width is two times shorter with the SLM used. The modulator consists of an array of 128 pixels, each with a width of 97μm. Every pixel can independently affect the phase of the corresponding spectral component of the beam passing through it by means of an applied voltage. The phase distribution is controlled and optimized by adjusting the voltages in a feedback loop using an evolutionary algorithm. In our experiment the phase distribution was optimized on the ion rate, which served as a feedback signal.

After passing the phase modulator the low-energy pulses from the oscillator are amplified in a regenerative amplifier. The Q-switched cavity of the amplifier with a Ti:sapphire crystal is CW pumped by an Ar^+ ion laser. The pulse repetition rate in the amplifier is 100 kHz. After 18 round trips, the amplified pulses are ejected with an energy of 8μJ and a pulse width of 15 ps.

In order to obtain short pulses the dispersion is compensated in a prism compressor. A Proctor-Wise double prism configuration is used. Finally, the 35 fs laser pulses at a wavelength of 800 nm and a repetition rate of 100 kHz are delivered to the experiment. The maximum output energy is 7μJ.

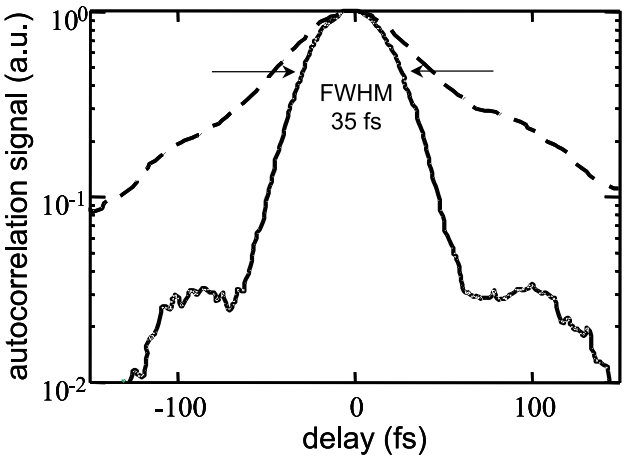

Fig. 3.15: Non-collinear autocorrelation traces of the amplified output pulses with SLM (solid line) and without SLM (dashed line) [126].

3.8 Determination of light intensity

The light intensity of the on-axis focused laser beam cannot be measured directly. It can be derived from the measurement of the integral ion yield dependence on light intensity. Since single ionization of atoms in a strong laser field is well described by the ADK tunneling theory, we can use the ADK single ionization rate [10] for the light intensity calibration. Fig. 3.16 shows the result of this calibration for krypton as a target. We measured the number of singly charged Kr^+ ions as a function of the laser output power, which was determined by means of a power meter. From the ADK curve which fits the experimental points we are able to derive a relation between the laser output power and the light intensity peak in the focal spot. However, the determination accuracy of the light intensity in this way is quite low. Alternatively, it can be obtained from the differential ATI photoelectron energy spectra (Fig. 3.17). Here, we can use the differential ADK formula for the electron momentum distribution based on the tunneling theory [129]

$$\omega(p_{\parallel}, p_{\perp}) = \omega(0) \exp\left[-\frac{p_{\parallel}^2 \omega^2 (2I_p)^{3/2}}{3E^3} - \frac{p_{\perp}^2 (2I_p)^{1/2}}{E}\right], \tag{3.28}$$

where I_p is the ionization potential, ω is the laser frequency and E is the electric field strength of the light wave. The corresponding energy distribution $(p_{e,\parallel}^2/(2m_e))$ obtained using this formula fits very well to the experimentally observed one in the low energy region ($E_{kin} < 2U_p$) of directly emitted electrons. Based on these methods the light intensity is determined within an uncertainty of 20%. Furthermore,

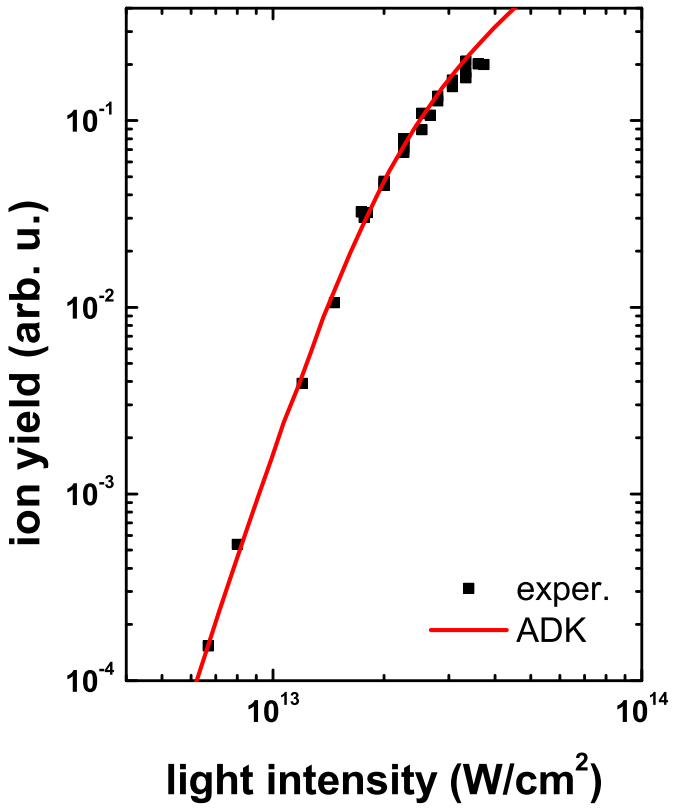

Fig. 3.16: Kr^+ ion yield as a function of light intensity: ADK theory (red curve) and experiment (black squares).

we compared our electron energy spectra at different light intensities with those of Paulus [130], which have been obtained using the same laser system.

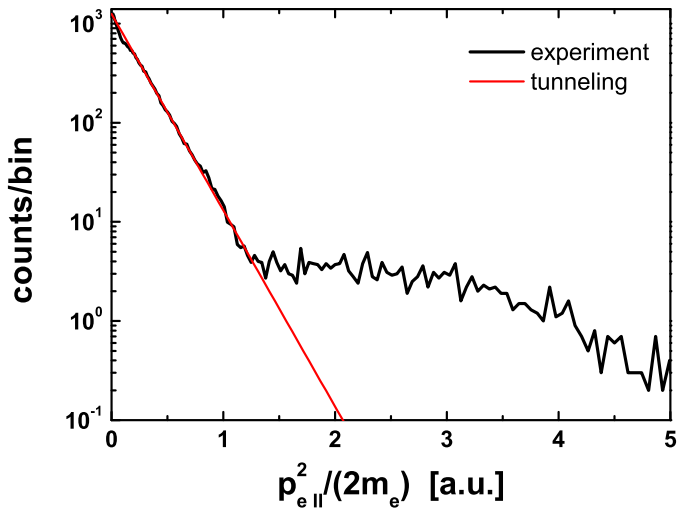

Fig. 3.17: ATI photoelectron kinetic energy distribution for single ionization of Ne (black curve) at a light intensity of 3×10^{14} W/cm^2; comparison with the kinetic energy distribution calculated based on the tunneling theory (red curve).

4. Non-sequential double ionization of atoms: results and discussion

In this chapter we discuss the experimental results on non-sequential double ionization of atoms (neon and argon) in linearly polarized high-intensity 35 fs laser pulses. The laser system is considered in Chapter 3. As noted before, the "CoboldPC" software was employed to analyze the raw experimental data. The analysis program is given in the Appendix A.

4.1 Electron sum-momentum distributions

We measured the electron sum-momentum distributions for Ar and Ne in order to analyze in detail the NSDI mechanism and its atom specific features. For NSDI via electron impact ionization one expects a double-hump structure of the e^- sum-momentum distribution parallel to the light polarization direction.

In the previous chapter we have discussed the momentum conservation for single and double ionization by many photons. We have shown that in the direction of the light polarization (z-axis, Fig. 3.3) and perpendicular to it (x-axis) the momentum of a doubly charged ion is equal to the sum of the momenta of the two photoelectrons emerging from double ionization (3.12), (3.13). It follows that the momentum distribution of doubly charged ions is equivalent to the sum-momentum distribution of the two corresponding photoelectrons. We have to take into account that, after ionization, electrons and ions are additionally accelerated by the oscillating electric field of a light wave (2.14) along the z-axis during the laser pulse. The drift momentum of the doubly charged ion gained during this acceleration is twice as large as the drift momentum of each electron (2.18). In the experiment we actually measure the final momenta of the photoelectrons and ions including the drift momentum they get. The measured momentum distributions of ions and electrons in the transverse direction (x-axis) are not affected by the light wave which is linearly polarized along z.

Fig. 4.1 displays Ne^{2+} and Ar^{2+} ion momentum distributions (= sum-momentum distributions of the two photoelectrons) measured in a focused linearly polarized light beam at light intensities, where non-sequential double ionization is expected.

The number of doubly charged ions per momentum bin[1] is plotted versus the corresponding momentum measured in atomic units. The panels on the left show the momentum distributions projected onto the polarization axis $f(p_\parallel)$, which is obtained by integrating the momentum distribution function over all transverse momenta

$$f(p_\parallel) = \int d^2\vec{p}_\perp f(\vec{p}). \tag{4.1}$$

The panels on the right show the corresponding distributions projected onto the light beam propagation direction (x-axis) $f(p_\perp)$, where

$$f(p_{\perp,x}) = \int dp_\parallel dp_{\perp,y} f(\vec{p}). \tag{4.2}$$

The Ne^{2+} momentum distribution (Fig. 4.1 (a)) exhibits a double-hump structure with a pronounced minimum at $p_\parallel = 0$ which has been observed earlier [17, 131]. Such a structure is an indication of instantaneous electron impact ionization (rescattering) which occurs preferentially when the oscillating electric field of the light wave $E_0(t)\cos\omega t$ is close to zero [17]. The final longitudinal drift momentum of the doubly charged ion

$$p_{i\parallel} = \frac{q}{\omega} E_0(t_r)\sin\omega t_r, \tag{4.3}$$

reaches maxima at zero crossings of the electric field and it is equal to zero at field maxima. For other ionization mechanisms ("shake-off", collective tunneling) both electrons are expected to be released near maxima of the oscillating electric field. This should lead to small final longitudinal momenta with a maximum of the momentum distribution at zero. Therefore these mechanisms can be ruled out to be the main NSDI mechanism.

The Ar^{2+} momentum distribution exhibits a minimum at zero, which is much less pronounced in comparison with Ne (Fig. 4.1 (a)) and is even absent at the lower light intensity (Fig. 4.1 (c)). This may indicate that the ionization mechanism for Ar differs from that for Ne. However, we supply evidence below that the main NSDI mechanism for Ar is also instantaneous impact ionization by a rescattering electron. First, we note that the longitudinal momentum distributions of Ar^{2+} and Ne^{2+} have equal widths at the same light intensity (Fig. 4.1 (a)). Due to acceleration in the light pulse after electron impact ionization, the doubly charged ion, and therefore the electrons are able to gain a drift momentum. Based on the classical rescattering model, the maximum drift momentum is $4\sqrt{U_p}$. This value determines the width of the electron sum-momentum distribution along the light polarization direction. The momentum $|p_\parallel| = 4\sqrt{U_p}$ is denoted by the arrows in Fig. 4.1 (a,c). It is close to the

[1] The bin size is determined in the "CoboldPC" program; in our case it is 0.25 a.u.

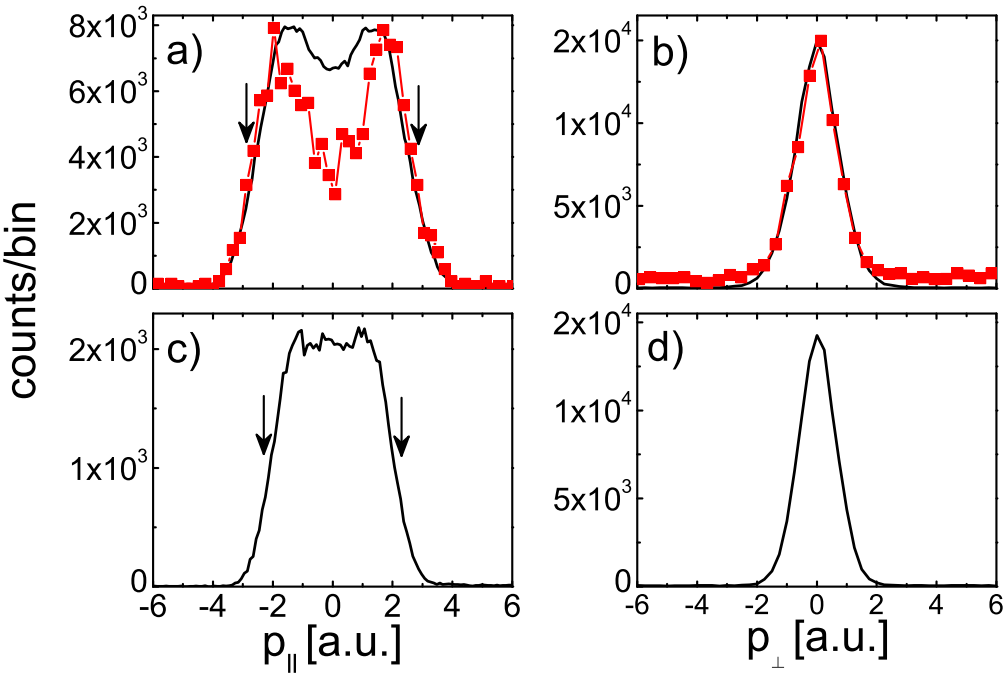

Fig. 4.1: Ar^{2+} (black curve) and Ne^{2+} (red curve with squares) momentum distributions parallel (left) and perpendicular (right) to the light polarization direction: (a,b) at 2.4×10^{14} W/cm^2; (c,d) at 1.5×10^{14} W/cm^2.

half widths of the observed distributions for Ne and Ar. This is an indication that the main double ionization mechanism of Ar and Ne is the same.

The transverse momentum distributions of Ar^{2+} and Ne^{2+} are practically identical at the same light intensity (Fig.4.1 (b)). This indicates that $f(p_\perp)$ is insensitive to the initial state from which the electrons are removed, for Ne from the $(2p)$ and for Ar from the $(3p)$ shell. Both momentum distributions are very narrow with a maximum at $p_\perp = 0$. In the semiclassical rescattering model, the kinetic energy of the recolliding electron is expected to play a decisive role for electron impact ionization. The latter occurs when $E_{kin,max}$ is larger than the ionization potential of the singly charged ion core I_p^+ (see Chapter 2). As can be seen in Fig. 4.1 (b), the essential difference in the respective maximum electron excess energy $(E_{kin,max} - I_p^+)$ (4.5 eV for Ne and 18 eV for Ar) does not influence $f(p_\perp)$. The overall distribution shape also does not change with light intensity (Fig.4.1 (d)). A detailed discussion of the measured transverse momentum distributions $f(p_\perp)$ will be given in Sec. 4.4.

Summarizing, we observed a clear double-hump structure of the electron sum-momentum distribution for Ne, that gives a strong evidence for electron impact ionization as the main NSDI mechanism. Although for Ar these indications are not pronounced, the width of the distribution suggests that electron impact ionization contributes strongly to NSDI.

4.2 Electron momentum correlation

Our momentum spectrometer allows for highly resolved differential measurements of the momentum correlation of the two photoelectrons emitted in double ionization. We measured the e^--e^- momentum correlation in order to clarify the origin of the specific behavior of Ar, which we found in the electron sum-momentum measurements.

Fig. 4.2 shows the e^--e^- momentum correlation for Ar parallel to the light polarization axis at the same light intensities as in Fig. 4.1. In these density plots the horizontal axis represents the momentum $p_{1,\parallel}$ of the detected electron and the vertical one corresponds to the momentum $p_{2,\parallel}$ of the second photoelectron. The value of $p_{2,\parallel}$ is calculated from the momentum conservation (3.12) using the measured $p_{1,\parallel}$ and the measured momentum of the corresponding Ar^{2+} ion. The color scale denotes the number of electron pairs detected per momentum bin.

At both light intensities two maxima along the main diagonal in the first and third quadrants of the plots are observed. They have been found to be a characteristic of instantaneous impact ionization [68, 69]. The maxima appear on the diagonal $p_{1,\parallel} = p_{2,\parallel}$ at ± 1 a.u. (Fig. 4.2 (a)) and ± 0.7 a.u. (Fig. 4.2 (b)) for the given light intensities. This corresponds to the case where the two photoelectrons with equal longitudinal momenta are emitted in the same half-space along the z-axis (positive

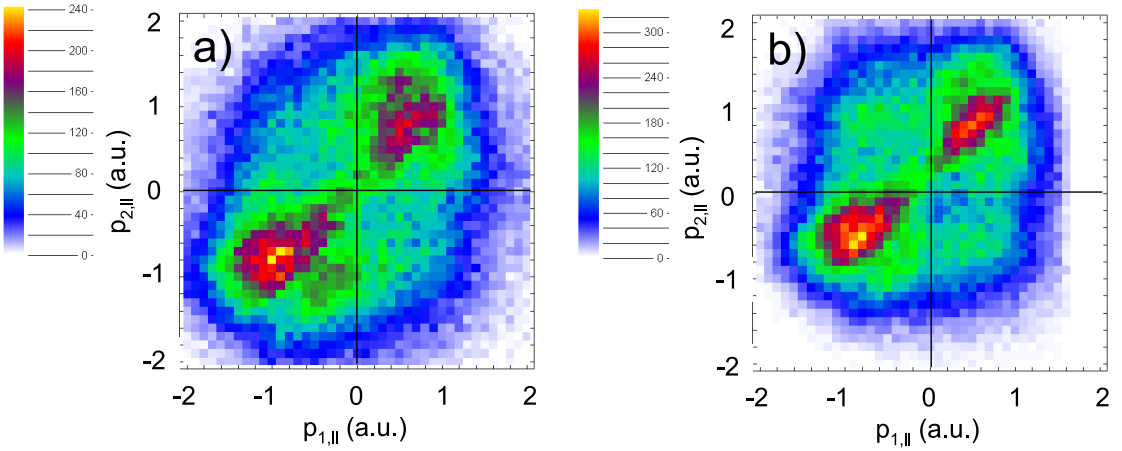

Fig. 4.2: The momentum correlation of the two photoelectrons after double ionization of Ar in linearly polarized 35 fs laser pulses at two light intensities: (a) at $2.4\times10^{14} W/cm^2$; (b) at 1.5×10^{14} W/cm^2. The momentum components parallel to the light polarization direction are shown.

or negative direction). The two electrons ejected simultaneously after impact ionization tend to have equal longitudinal final momentum vectors due to post-collision acceleration in the light wave.

The projection of the plots onto the main diagonal $p_{1,\parallel} = p_{2,\parallel}$ is equivalent to the sum-momentum distributions we have already discussed (Fig. 4.1 (a,c)), where $p_\parallel = p_{1,\parallel} + p_{2,\parallel}$. Evidently electrons from instantaneous impact ionization dominate the sum-momentum distribution at large momenta $|p_\parallel|$. The reason for the shallow minimum at $p_\parallel = 0$ at the light intensity $2.4 \times 10^{14} W/cm^2$ and its disappearance at 1.5×10^{14} W/cm^2 for Ar also becomes clear. In contrast to Ne, where the vast majority of electron pairs is emitted with similar momenta into the same half-space [72], in non-sequential double ionization of Ar many electron pairs are also emitted into the opposite half-spaces with significant and similar $|p_{i,\parallel}|$ $(i = 1, 2)$. This gives rise to a large amount of events in the second and fourth quadrant of the plots in Fig. 4.2. They contribute to the sum-momentum distribution near $p_\parallel = 0$.

In Fig. 4.3 the sum-momentum distributions are obtained by projecting only a narrow part ($p_{1,\parallel} - p_{2,\parallel} \sim 0$) of the e$^-$-e$^-$ momentum distribution along the diagonal $p_{1,\parallel} = p_{2,\parallel}$. Constructed in this way, they include only the contribution from the electron pairs gained in recollision ionization. A pronounced double-hump structure, which is not observed in the full sum-momentum distribution (Fig. 4.1) can be clearly seen. Obviously the valley around $p_\parallel = 0$ is filled by the electron pairs arising from a second ionization mechanism. A possible scenario for this mechanism is electron impact excitation during recollision with subsequent electric field (tun-

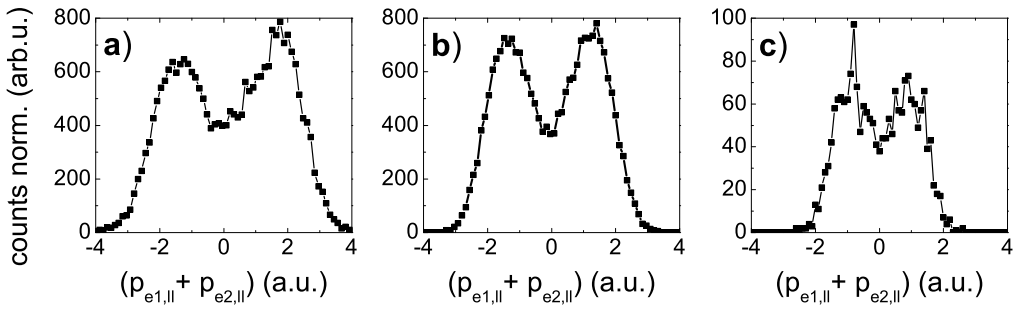

Fig. 4.3: Projections of a narrow part ($p_{1,\parallel} - p_{2,\parallel} \sim 0$) of the e^--e^- momentum correlation from Fig. 4.2 and Fig. 4.5 along the diagonal $p_{1,\parallel} = p_{2,\parallel}$. (a) at 2.4×10^{14} W/cm^2; (b) at 1.5×10^{14} W/cm^2; (c) 0.9×10^{14} W/cm^2.

neling) ionization [69]. The contribution of this ionization mechanism becomes more prominent with decreasing light intensity (Fig. 4.2 (b)).

From our measurement of the electron momentum correlation we conclude that for Ar in addition to electron impact ionization (two maxima on the main diagonal) a second ionization mechanism contributes to NSDI. The latter is related to electron impact excitation with subsequent electric field ionization by the light wave. The electron pairs from this mechanism conceal the double-hump structure in the electron sum-momentum distribution for low light intensities.

4.3 Sub-threshold electron impact ionization

As discussed before, in the semiclassical rescattering picture an ionization threshold for electron impact ionization is expected. If the kinetic energy of the recolliding electron $E_{kin,max}$ is smaller than the ionization potential of the singly charged ion core I_p^+ electron impact ionization should become impossible. However, preceding experiments have shown that the dependence on light intensity of the integral ion yield ratio of doubly charged to singly charged ions $[A^{2+}]/[A^+]$ does not show any abrupt change at light intensities where $E_{kin,max}$ reaches the ionization threshold I_p^+ [14, 67]. Since the rescattering scenario was found to be valid for non-sequential double ionization of rare gases [17, 68], this fact has remained a puzzle and may point to a gradual change of ionization mechanisms near threshold. We investigated non-sequential double ionization of Ar at light intensities, where the kinetic energy of the returning electron $E_{kin,max}$ is close to or below the expected threshold for instantaneous impact ionization of Ar^+.

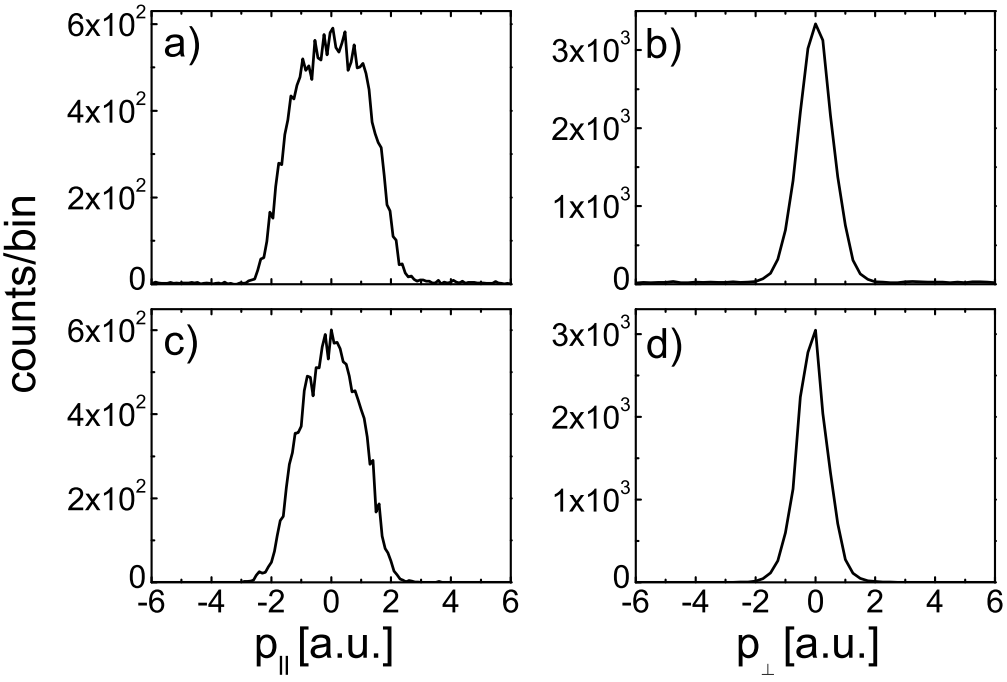

Fig. 4.4: Ar^{2+} momentum distributions parallel (left) and perpendicular (right) to the light polarization direction: (a,b) at 1.1×10^{14} W/cm^2; (c,d) at 0.9×10^{14} W/cm^2.

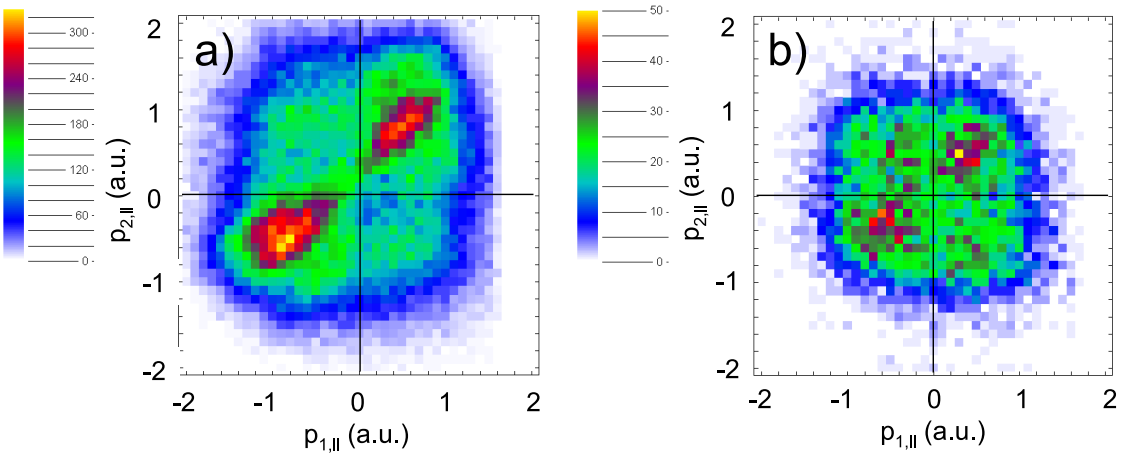

Fig. 4.5: The momentum correlation of the two photoelectrons after double ionization of Ar similar to Fig. 4.2 but at light intensities below the threshold for e^- impact ionization: (a) at 1.5×10^{14} W/cm^2; (b) at 0.9×10^{14} W/cm^2.

Fig. 4.4 shows the sum-momentum distributions of the two photoelectrons after double ionization of Ar similar to those in Fig. 4.1, but this time at 1.1×10^{14} W/cm^2 and 0.9×10^{14} W/cm^2. At these light intensities $E_{kin,max}$ is not sufficient for instantaneous impact ionization. The corresponding "excess energies" $(E_{kin,max} - I_p^+)$ are -7.2 eV and -10.5 eV. Comparing Fig. 4.4 with Fig. 4.1 we observe a gradual change of the functional form of $f(p_\parallel)$ (left panel) with decreasing intensity while crossing the threshold $E_{kin,max} = I_p^+$. It changes from a double-hump structure at 2.4×10^{14} W/cm^2 to a bell-shaped one at 0.9×10^{14} W/cm^2. The distribution width becomes smaller with decreasing intensity. In contrast, the transverse sum-momentum distribution $f(p_\perp)$ does not change its shape with decreasing light intensity whereas its width slightly decreases. At first sight, a bell-shaped structure of $f(p_\parallel)$ with a maximum at $p_\parallel = 0$ seems to indicate the disappearance of impact ionization below the threshold. But, as we have seen before, the sum-momentum distribution for Ar near $p_\parallel = 0$ is dominated by a second ionization mechanism (impact excitation), which seems to become more prominent with decreasing intensity (Fig. 4.2).

A closer look at the e^--e^- momentum correlation at the lowest intensity 0.9×10^{14} W/cm^2 (Fig. 4.5 (b)) reveals that the characteristic maxima due to electron impact ionization do not vanish, although $E_{kin,max} \ll I_p^+$. This becomes even more evident from Fig. 4.3 (c) where a narrow part of this e^--e^- momentum distribution along the diagonal $p_{1,\parallel} = p_{2,\parallel}$ is projected. The double-hump structure does not disappear in the below-threshold regime. It is just masked due to the electron pairs from a second ionization mechanism. They completely fill the minimum at $p_\parallel = 0$

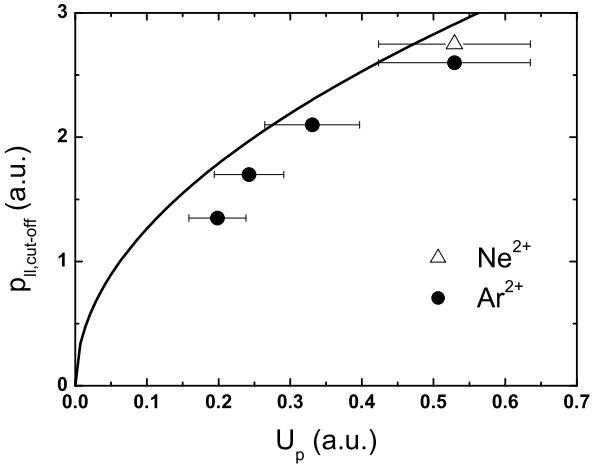

Fig. 4.6: The dependence of the cutoff momentum of the Ar^{2+} and Ne^{2+} momentum distributions on the light intensity. The data are acquired from Fig. 4.1 and Fig. 4.4. The solid line is the function $4\sqrt{U_p}$.

of the full sum-momentum distribution in Fig. 4.4 (c). For convenience, in Fig. 4.5 the e^--e^- momentum correlations at 0.9×10^{14} W/cm^2 (below threshold) and at 1.5×10^{14} W/cm^2 (above threshold) are directly compared. As can be seen, below threshold instantaneous electron impact ionization still dominates the distribution $f(p_{1,\parallel}, p_{2,\parallel})$, and therefore the corresponding sum-momentum distribution $f(p_\parallel)$ at large electron momenta where $p_{1,\parallel} = p_{2,\parallel}$. However, the overall contribution of electron pairs from recollision ionization becomes smaller in the intensity regime below ionization threshold. In contrast, the second ionization mechanism, forming events in the second and fourth quadrants of the e^--e^- momentum correlation in Fig. 4.5, seems to become more important below the threshold for impact ionization. At the intensity 0.9×10^{14} W/cm^2 the maximum kinetic energy of the returning electron just suffices to excite Ar^+ from the ground state $3s^2 3p^5$ to the lowest bound excited states $3s^2 3p^4 (^3P) 4s$, that may facilitate electron impact excitation.

The importance of the e^- impact ionization mechanism for the final electron momentum distribution becomes more obvious in the dependence of the cutoff of the sum-momentum distribution $f(p_\parallel)$ on the light intensity (in terms of ponderomotive energy) in Fig. 4.6. We here define the cutoff momentum of $f(p_\parallel)$ as the momentum where $f(p_\parallel)$ reaches half of the maximum ion yield in Fig. 4.1 and Fig. 4.4. The data points for Ar and Ne are closely following the function $4\sqrt{U_p}$ (solid curve) lying systematically slightly below. The error bars of U_p reflect the uncertainty in

determination of the light intensity. The deviation of the data points from $4\sqrt{U_p}$ is somewhat larger at small U_p due to an increasing amount of events in the second and fourth quadrants of Fig. 4.5. These events arise from the e^- impact excitation channel and give rise to the maximum of $f(p_\parallel)$ at $p_\parallel = 0$ in Fig. 4.4. At low light intensities they tend to decrease the cutoff momentum. Keeping in mind that $4\sqrt{U_p}$ is classically the largest momentum that the doubly charged ion can gain in post-collision acceleration, we come to the conclusion that photoelectrons contributing to large $|p_\parallel|$ at all light intensities in experiment, including the sub-threshold regime, are generated in instantaneous e^- impact ionization. It should be noted that also at large light intensity ($1.3 \times 10^{15} W/cm^2 \rightarrow U_p = 2.8$ a.u.) the data point for Ne from Ref. [17] (not shown in Fig. 4.6) is in agreement with the tendency of our data lying slightly below $4\sqrt{U_p}$.

The question arises how the observed instantaneous electron impact ionization below the threshold $E_{kin,max} = I_p^+$ can be explained within the semiclassical rescattering model? In the quasi-static limit it may be understood by taking into account that the electric field of the light wave is usually different from zero at the instant of the electron recollision at t_r. The actual threshold for e^- impact ionization of a singly charged ion in an external electric field of strength $E_0(t_r)\cos\omega t_r$ at the time t_r is therefore lowered to the instantaneous saddle point energy of the combined external and Coulomb potential, which is given by

$$I_p^+(t_r) = I_{p,0}^+ - 2\sqrt{2E_0(t_r)\cos\omega t_r} \qquad (a.u.), \tag{4.4}$$

where $I_{p,0}^+$ is the unperturbed ionization potential. Fig. 4.7 displays schematically the lowering of the ionization threshold. Here, the one-dimensional ionic Coulomb potential modified by the electric field of the light wave is depicted at the instant of recollision t_r. The relation (4.4) is a good approximation of the real ionization threshold as long as the Stark shift of the ionic ground state remains small and the saddle point appears well outside of the electron charge cloud of the doubly charged ion core. Such a field induced shift of the ionization threshold has been introduced recently by van der Hart and Burnett in order to understand the missing threshold behavior in the dependence of the total ion yield ratio $[He^{++}]/[He^+]$ on the light intensity for helium [94].

Fig. 4.8 (a) gives an idea of the instantaneous electron impact ionization below threshold from the viewpoint of energy. The kinetic energy of the returning electron $E_{kin}(t_r)$ (solid line) and the instantaneous ionization potential of the singly charged argon ion $I_p(Ar)^+(t_r)$ for two light intensities, below the impact ionization threshold (0.9×10^{14} W/cm^2 - dashed line) and above (2.4×10^{14} W/cm^2 - dot-dashed line), are plotted in terms of the ponderomotive energy U_p versus the phase of the external electric field at the instant of recollision ωt_r. The oscillating electric field of the light wave crosses zero at $\omega t_r = 1.5\pi$. At the instant of time $1.5\pi/\omega$ the ionization potential $I_p^+(t_r)$ is unperturbed and reaches its maximum $I_{p,0}^+$. At all ωt_r with

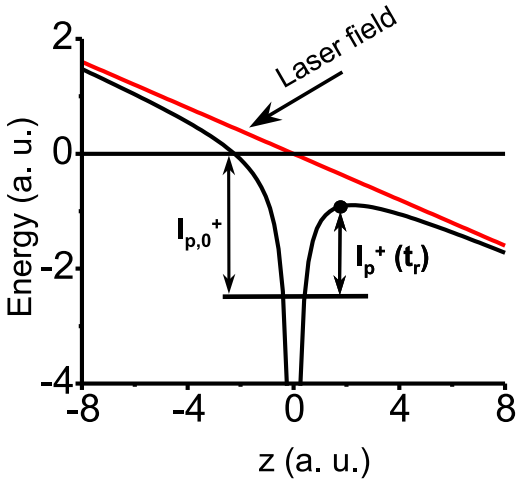

Fig. 4.7: Schematic diagram of the 1D Coulomb potential of a singly charged ion core in the presence of the external electric field of the laser at the instant of recollision t_r. $I_{p,0}^+$ is the unperturbed ionization potential of the singly charged ion, and $I_p^+(t_r)$ is the ionization potential in the non-zero electric field of the light wave at the time of recollision t_r.

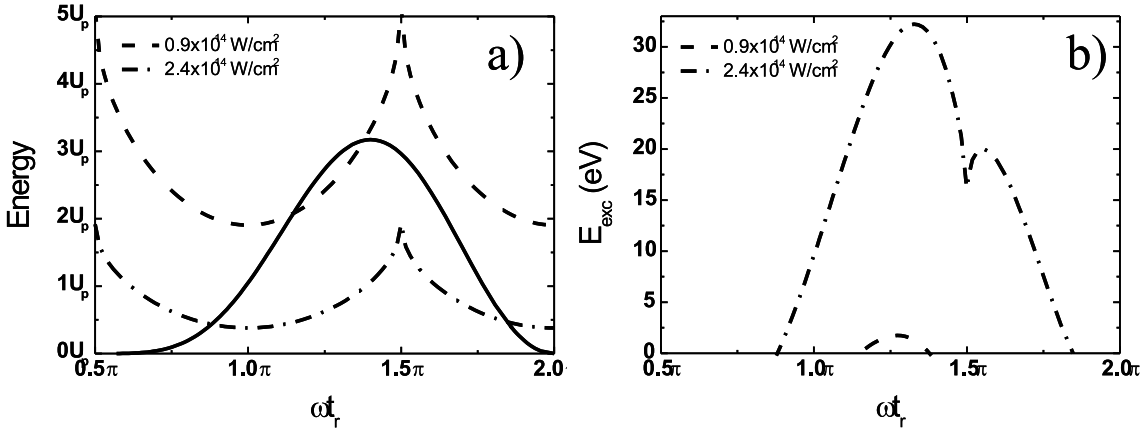

Fig. 4.8: (a) The kinetic energy of the returning electron $E_{kin}(t_r)$ (solid curve) and the instantaneous ionization potential $I_p(Ar)^+(t_r)$ (dashed line at 0.9×10^{14} W/cm^2 and dot-dashed line at 2.4×10^{14} W/cm^2) as a function of ωt_r, the electric field phase at the instant of recollision (the energy scale is given in units of U_p!). (b) The corresponding excess energy E_{exc} after e^- impact ionization.

$E_{kin,max}(t_r) \geqslant I_p^+(t_r)$ the kinetic energy of the returning electron classically suffices to kick out a second electron instantaneously in an inelastic collision. This may occur in a large interval of return times at the light intensity 2.4×10^{14} W/cm^2, i.e. above threshold. Below threshold, at 0.9×10^{14} W/cm^2, electron impact ionization may also happen in a restricted interval of ωt_r, where the $E_{kin,max}(t_r)$ curve is lying above the corresponding instantaneous ionization potential curve $I_p^+(t_r)$, although it is not possible with the unperturbed ionization potential $I_{p,0}^+$. The dependence of the instantaneous excess energy after collision $E_{exc} = E_{kin,max}(t_r) - I_p^+(t_r)$ on the return time is plotted in Fig. 4.8 (b).

Concluding, we observed an electron momentum correlation characteristic of instantaneous electron impact ionization below the corresponding ionization threshold. We are able to explain this behavior within the semiclassical rescattering model by taking into account the electric field of the light wave, which reduces the ionization threshold at the instant of electron recollision. At all light intensities in our experiment electron impact ionization was found to be the dominant NSDI mechanism.

4.4 The transverse electron sum-momentum distribution

We now draw our attention to the transverse electron sum-momentum distribution. $f(p_\perp)$ is not affected by post-collision acceleration of ions, and thus of the photoelectrons, in the electric field of the linearly polarized light wave. It, nevertheless, is determined in the recollision event while the colliding electron interacts with the singly charged ion core and with the second electron which is going to be kicked out. Therefore $f(p_\perp)$ is expected to give more insight into the recollision process than $f(p_\parallel)$.

As we have seen in Fig. 4.1 (b,d) and Fig. 4.4 (b,d), at all light intensities in our experiment $f(p_\perp)$ is a very narrow distribution with a maximum at zero momentum. The distribution can be well fitted with a Gaussian function. Within the rescattering model one would expect that the full width at half-maximum (FWHM) of $f(p_\perp)$ depends on the square root of the available excess energy ($E_{kin,max} - I_p^+$), and therefore linearly on the external electric field strength E_0. Surprisingly, we found instead a scaling of the FWHM of $f(p_\perp)$ with $\sqrt{E_0}$ (Fig. 4.9). The experimental data points for the FWHM of $f(p_\perp)$ of Ar and Ne follow closely the $const \times \sqrt{E_0}$ curve. No abrupt change is found at the threshold for impact ionization of Ar^+ which corresponds to the electric field strength $E_0 = 0.06$ a.u.. Also at large excess energy (200 eV) for Ne the corresponding data point at $E_0 = 0.19$ a.u.[2] is lying on the $const \times \sqrt{E_0}$ curve. A faster decrease in width is found only at the lowest E_0, which corresponds to the light intensity 0.9×10^{14} W/cm^2. Here, a large amount of events

[2] the data point is taken from [131].

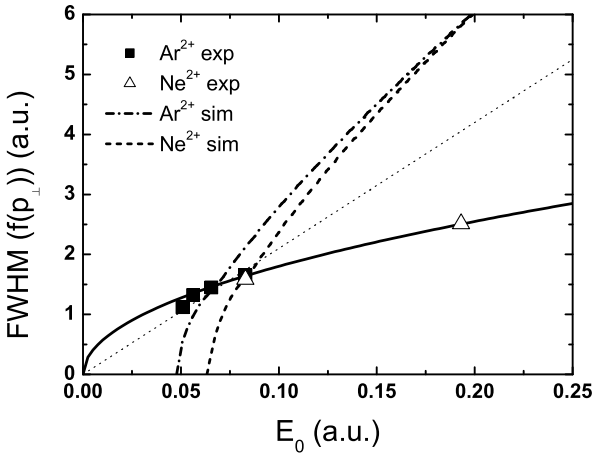

Fig. 4.9: The FWHM of the doubly charged ion momentum distribution $f(p_\perp)$ plotted versus the peak electric field strength E_0. Black squares and open triangles are experimental data points of Ar and Ne, respectively. Dashed and dot-dashed lines are corresponding results for Ne and Ar derived from the semiclassical model calculations. The solid line along the experimental points is the function of $const \times \sqrt{E_0}$ and the thin dotted line is proportional to E_0.

not attributed to instantaneous impact ionization of Ar^+ contributes to $f(p_\perp)$. This may be responsible for the deviation.

In Fig. 4.9 the experimentally observed dependence of the FWHM of $f(p_\perp)$ on E_0 is directly compared with our semiclassical model calculations for Ne (dashed curve) and Ar (dot-dashed curve). The calculation is based on the rescattering model with taking into account the lowering of the ionization threshold I_p^{+3}. The curves are far from describing the experimental behavior. They are rising much faster than $\sqrt{E_0}$ and even faster than E_0, which is displayed by a thin dotted line. Therefore, it seems that the width of the transverse electron sum-momentum distribution from the experiment is not determined by the impact parameters of the recolliding electron.

The scaling of $f(p_\perp)$ with $\sqrt{E_0}$ reminds one of the scaling found for the FWHM of the momentum distribution of the photoelectron in strong field single ionization in the quasi-static limit (see, for example, [132]). The corresponding momentum distribution is

$$f(\vec{p}_\perp) = \omega_0 \exp -\frac{\sqrt{2I_p}\vec{p}_\perp^{\,2}}{E_0}, \tag{4.5}$$

[3] the details of the model calculation will be discussed in the next section.

with I_p the ionization potential of the atom. The FWHM of this Gaussian function is

$$FWHM = \frac{2\sqrt{\ln 2}}{(2I_p)^{1/4}}\sqrt{E_0}. \tag{4.6}$$

Here, an electron tunnels through an effective potential barrier formed by the combined Coulomb and external electric field. The similar behavior of $f(\vec{p}_\perp)$ for single ionization and for the electron sum-momentum distribution in double ionization is not accidental. This implies that in electron impact ionization of the singly charged ion, at the instant of recollision, the electric field of the light wave plays an important role to free the second electron. Such a behavior can be explained if one assumes that the returning electron does not transfer enough energy to the second one so that either the second electron or the whole collision complex gets ionized by tunneling or above-barrier ionization in the presence of the external field. This scenario has been discussed by Sacha and Eckhardt [101]. The light electric field in that case would have a significant influence on the transverse momentum distribution of the two electrons similar to single ionization. Barrier suppression or tunneling would favor small transverse momenta and a scaling of the width of $f(\vec{p}_\perp)$ with $\sqrt{E_0}$, as found in the experiment, may result. For this scenario the collisions which most efficiently lead to double ionization are expected to happen neither at zero crossings of the electric field of the light wave nor at the highest kinetic energy possible for the returning electron.

The importance of recollision events at non-zero electric field which do not result from the most energetic electrons ($E_{kin} < 3.17U_p$) but contribute efficiently to non-sequential double ionization, has also been discussed by Panfili et al. [133] within a one-dimensional classical simulation. They found that the most effective collisions happen at $1/2\pi < \omega t_r < \pi$ and $3/2\pi < \omega t_r < 2\pi$, where the recolliding electron is moving against the external light electric field back to the ion core. After the energy transfer during the collision, even if small, the bound electron is able to escape the Coulomb potential while the barrier suppression is maximum. In this case one would also expect that the final electron momentum distribution is mainly determined by the field and not by the excess energy of the recolliding electron. However, the relevance of this one-dimensional simulation in the full three-dimensional real world is presently not assured. It is also not clear whether the recollision scenario outlined above allows one to reproduce the electron sum-momentum distribution parallel to the polarization direction $f(p_\parallel)$ and the e-e momentum correlation found in the experiment.

To conclude, our analysis of the transverse electron sum-momentum distribution indicates that the distribution width is not determined by the impact parameters of the recolliding electron, as expected from the rescattering model, but by the electric field of the light wave, which was found to play an important role at the instant of

electron recollision in NSDI.

4.5 Comparison with theoretical results

Let us compare our experimental results to several theoretical calculations for NSDI. Most of them assume instantaneous electron impact ionization. Therefore we first concentrate on this NSDI mechanism.

The quantum-mechanical S-matrix calculations [87, 85, 90] yield a good qualitative agreement with our experimentally observed momentum correlation of the two photoelectrons. In this S-matrix approach the electron interaction at the instant of recollision is described by a three-body contact interaction potential of the two electrons and the ion core. Figs. 4.10 (b) and 4.11 (b) show the results of such a calculation made by Schomerus [134] for Ar. A strong field approximation has been used in this quantum-mechanical calculation. The two maxima in the first and third quadrants of the momentum correlation are well reproduced. This result is quite remarkable since the contact interaction of the electrons at the ion core seems a crude approximation.

Replacing the three-body contact interaction in the S-matrix calculations by the e^--e^- Coulomb potential [82, 84, 90, 91] and applying first-order Born approximation leads to a momentum distribution that differs substantially from the experimental one. This approach favors different longitudinal momenta of the two photoelectrons in the final state ($|p_{1,\parallel}| \neq |p_{2,\parallel}|$), especially with increasing light intensity. The plausible reason for this behavior is that the potential of the ion core is neglected.

The correct Coulomb interaction has been used by L.-B. Fu and co-workers [100] in a semiclassical trajectory calculation to model NSDI of helium. It included e^--e^- repulsion as well as the attractive Coulomb interaction of both electrons to the ion core. The momentum correlation $f(p_{1,\parallel}, p_{2,\parallel})$ for He obtained within this model qualitatively reproduces the experimentally expected ($f(p_{1,\parallel}, p_{2,\parallel})$ has not been measured for He but it is expected to behave as Ar). Both electrons tend to have large and equal momenta and thus the distribution $f(p_{1,\parallel}, p_{2,\parallel})$ peaks at the main diagonal where $|p_{1,\parallel}| = |p_{2,\parallel}| = 2\sqrt{U_p}$. No such calculation has been performed so far for Ar or Ne since the inclusion of further electrons turns the problem intractable.

At the time of our experiment no calculations have been available at the relevant light intensities that could be compared to our experimental results. We performed a semiclassical model calculation which allows one to obtain the momentum correlation of the two photoelectrons in double ionization for a comparison with the experimental results. Our calculation is based on the replacement of the quantum-mechanical S-matrix for recollision double ionization by its classical analog [87]. The distribution of the momenta $\vec{p}_1$ and $\vec{p}_2$ of the two photoelectrons is then determined

by

$$|S(\vec{p}_1,\vec{p}_2)|^2 = \int dt_0 R(t_0)\delta\left(E_{kin}(t_r) - \frac{\left(\vec{p}_1 - \vec{A}(t_r)/c\right)^2}{2} - \frac{\left(\vec{p}_2 - \vec{A}(t_r)/c\right)^2}{2} - I_p^+(t_r)\right)|V_{\vec{p}_1,\vec{p}_2,\vec{k}}|^2, \tag{4.7}$$

where $\vec{A}$ is the vector potential for the electric field of the light wave[4] and $|V_{\vec{p}_1,\vec{p}_2,\vec{k}}|^2$ is the collision form factor, which is determined by the e^--e^- interaction at the instant of recollision. The δ-function expresses energy conservation for electron impact ionization of the singly charged ion. The ionization probability of the first electron is calculated using the tunneling ADK rate $R(t_0)$ [10]. We assume that the recolliding electron starts its motion in the external electric field of the light wave $E = E_0 \sin\omega t$ at a time t_0 with zero-velocity. The electron trajectories are calculated purely classically. In the next step we take into account only those trajectories, for which the electron returns back to the singly charged ion core. This happens at a time t_r. Ionization of the bound electron from the ground state of the ion occurs, provided that the kinetic energy of the returning electron $E_{kin}(t_r)$ is larger than the instantaneous ionization potential $I_p^+(t_r)$. The latter is changing with the electric field of the light wave (see Eq. (4.4)). We investigated the influence of two different types of e^--e^- interactions at the instant of recollision: the three-body contact interaction of the two electrons and the ion core, analogously to that in the S-matrix calculations in Ref. [86, 91], and the electron-electron contact interaction. Finally, we take into account the acceleration of the two free photoelectrons in the external field after electron impact ionization. In Eq. (4.7) this is incorporated by the argument $\left(\vec{p}_i - \vec{A}(t_r)/c\right)^2$, $(i = 1, 2)$ in the δ-function. The main code of the simulation can be found in Appendix B.

Let us consider our theoretical results for the three-body contact interaction. In our model the three-body contact interaction results in a form factor $|V_{\vec{p}_1,\vec{p}_2,\vec{k}}|^2 = const$ in Eq. (4.7). It neither depends on the intermediate state momentum $\vec{k}$ of the recolliding electron nor on the final state electron momenta $\vec{p}_1$, $\vec{p}_2$. In Fig. 4.10 we compare our calculation (left panel) for the electron-electron momentum correlation for Ar at the light intensity 1.5×10^{14} W/cm^2 to the quantum-mechanical S-matrix calculation (right panel) by Schomerus [134]. In Fig. 4.11 the same comparison is done for the light intensity 0.9×10^{14} W/cm^2. The distributions have been integrated over all final transverse momentum components. As can be seen, our simple semiclassical model yields similar results as the quantum-mechanical S-matrix calculation at the given light intensities. In both calculations the two maxima appearing on the

[4] $\vec{E}(t) = -\frac{1}{c}\frac{\partial}{\partial t}\vec{A}(t)$

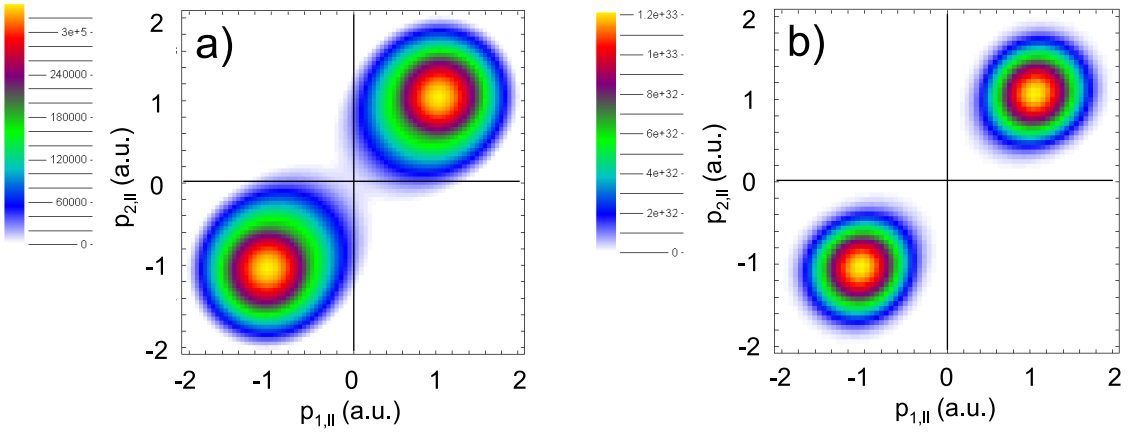

Fig. 4.10: e^--e^- momentum correlation for the longitudinal momentum components at a light intensity of 1.5×10^{14} W/cm^2 derived from (a) the semiclassical calculation; (b) the quantum-mechanical S-matrix calculation [134].

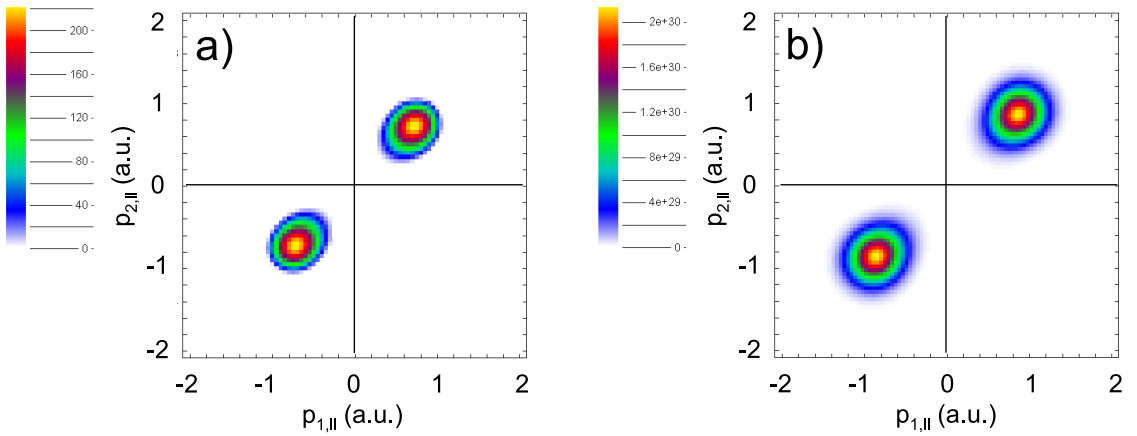

Fig. 4.11: The same as Fig. 4.10, but at 0.9×10^{14} W/cm^2. (a) the semiclassical calculation; (b) the quantum-mechanical S-matrix calculation [134].

main diagonal are qualitatively similar to those observed in the experiment. At the intensity 1.5×10^{14} W/cm^2 the semiclassical momentum distribution fills a larger phase space area than the quantum-mechanical one. The opposite is found at the lower light intensity. This tendency is a consequence of the shifting ionization potential I_p^+ in the presence of the external electric field incorporated in our semiclassical model. At high light intensity this leads to a larger available phase space than the constant $I_{p,0}^+$. Without taking into account this effect we obtain a very restricted electron momentum distribution near the classical ionization threshold and none at all below the threshold. At higher intensities, far above the threshold, the effect due to the decrease of I_p^+ is less prominent. The quantum-mechanical description, in contrast to the classical one, avoids the problem of the ionization threshold, since the absorption of a corresponding number of photons by the first electron in the continuum provides the energy needed for e^- impact ionization of the singly charged ion. This can be seen in the electron sum-momentum distribution obtained by the strong-field S-matrix calculation by Kopold et al. [85]. At light intensities below the classical threshold the distribution exhibits a sawtooth-like structure which reflects the discrete energy transfer from the light field.

The two maxima of the distributions in Fig. 4.10 (b) and Fig. 4.11 (b) appear at $p_{1,\parallel} = p_{2,\parallel} = \pm 2\sqrt{U_p}$, the value of the maximum classically allowed momentum. This is in a good agreement with previous results, e.g. [90]. A slightly smaller value is found for the peak of the classical distribution at low intensity (Fig. 4.11 (a)). However, both calculations predict a peak position at slightly higher momenta compared to the experiment (Fig. 4.5).

In the case of electron-electron contact interaction the form factor in Eq. (4.7) depends on the momentum $\vec{k}$ of the returning electron:

$$|V_{\vec{p}_1,\vec{p}_2,\vec{k}}|^2 \sim \frac{1}{[2I_p^+ + (\vec{k} - \vec{p}_1 - \vec{p}_2)^2]^2}. \tag{4.8}$$

In a linearly polarized electric field $\vec{k}$ has only one component parallel to the field. In the length gauge $\vec{k}$ is the instantaneous electron momentum at recollision

$$\vec{k} = 2\sqrt{U_p}(\cos\omega t_r - \cos\omega t_0)\vec{e}, \tag{4.9}$$

where $\vec{e}$ is the unit vector along the electric field, while in the velocity gauge $\vec{k}$ is the electron drift momentum at ωt_r:

$$\vec{k} = -2\sqrt{U_p}\cos\omega t_0\vec{e}. \tag{4.10}$$

This interaction potential thus results in a dependence of the final electron momentum correlation on the gauge chosen. Fig. 4.12 displays the results on the e^--e^- momentum correlation obtained using velocity (on the left) and length gauge (on

the right) for several light intensities. In velocity gauge the two peaks of the distribution are lying closer to the center compared to that in length gauge. The gauge dependence of $|S(\vec{p}_1, \vec{p}_2)|^2$ is certainly not physical. It appears due to a number of approximations which are not gauge invariant. However, the tendency to shift the maxima of $f(p_{1,\parallel}, p_{2,\parallel})$ on the diagonal $p_{1,\parallel} = p_{2,\parallel}$ closer to zero is a general feature of the e^--e^- contact interaction potential. The experimentally found positions of the maxima of $f(p_{1,\parallel}, p_{2,\parallel})$ are described better by the model with e^--e^- contact interaction than with the three-body contact one. A dramatic change happens for the e^--e^- contact interaction potential in both gauges with increasing intensity. The peaks on the main diagonal are spreading out along the direction $p_{1,\parallel} = -p_{2,\parallel}$. Consequently the almost round distribution found at 0.9×10^{14} W/cm^2 turns into a distribution stretched along the direction perpendicular to the main diagonal at higher intensities. In this case the calculated final momentum distribution is dominated by the photoelectron pairs emitted with different momenta $p_{i,\parallel}$. Such a behavior is, however, not confirmed experimentally. It should be noted here that in the case of the three-body contact interaction, discussed above, the round shape of the distribution does not change essentially with the light intensity.

So far we have discussed the theoretical results for the main NSDI mechanism, i.e. electron impact ionization. There is a well-known second ionization mechanism contributing to NSDI of Ar which is associated with instantaneous impact excitation followed by electric field ionization of the exited singly charged ion. This mechanism gives rise to the large amount of electrons emitted into opposite half-spaces along the light polarization direction. These electrons contribute to the second and forth quadrants of the e^--e^- momentum correlation (Fig. 4.2) and thus lead to the disappearance of the minimum at $p_\parallel = 0$ in the sum-momentum distribution for Ar at low intensities. A similar experimental behavior was observed for NSDI of He [16] but no such features were found for Ne [72].

Up to now just a limited number of NSDI calculations have taken into account the electron impact excitation mechanism. So far such calculations have only been done for He. The main problem of performing these calculations for other atomic systems is the deficiency of the theoretical and experimental data on total inelastic cross section for electron impact excitation. Moreover, excited states may be perturbed in the external laser field, that turns accurate calculations of the ionization probability from an excited state difficult.

The quantum-mechanical S-matrix calculations for He by Kopold *et al.* [85] and Goreslavskii *et al.* [86] showed that including electron impact excitation mechanism as a superposition of contributions from different excited states may yield momentum distributions similar to that found in experiments. It has been found that for the lowest excited states the electron sum-momentum distribution $f(p_\parallel)$ does not change its double-hump shape, while for higher excited states the minimum at zero momentum fills up quickly and the absolute electron yield rises.

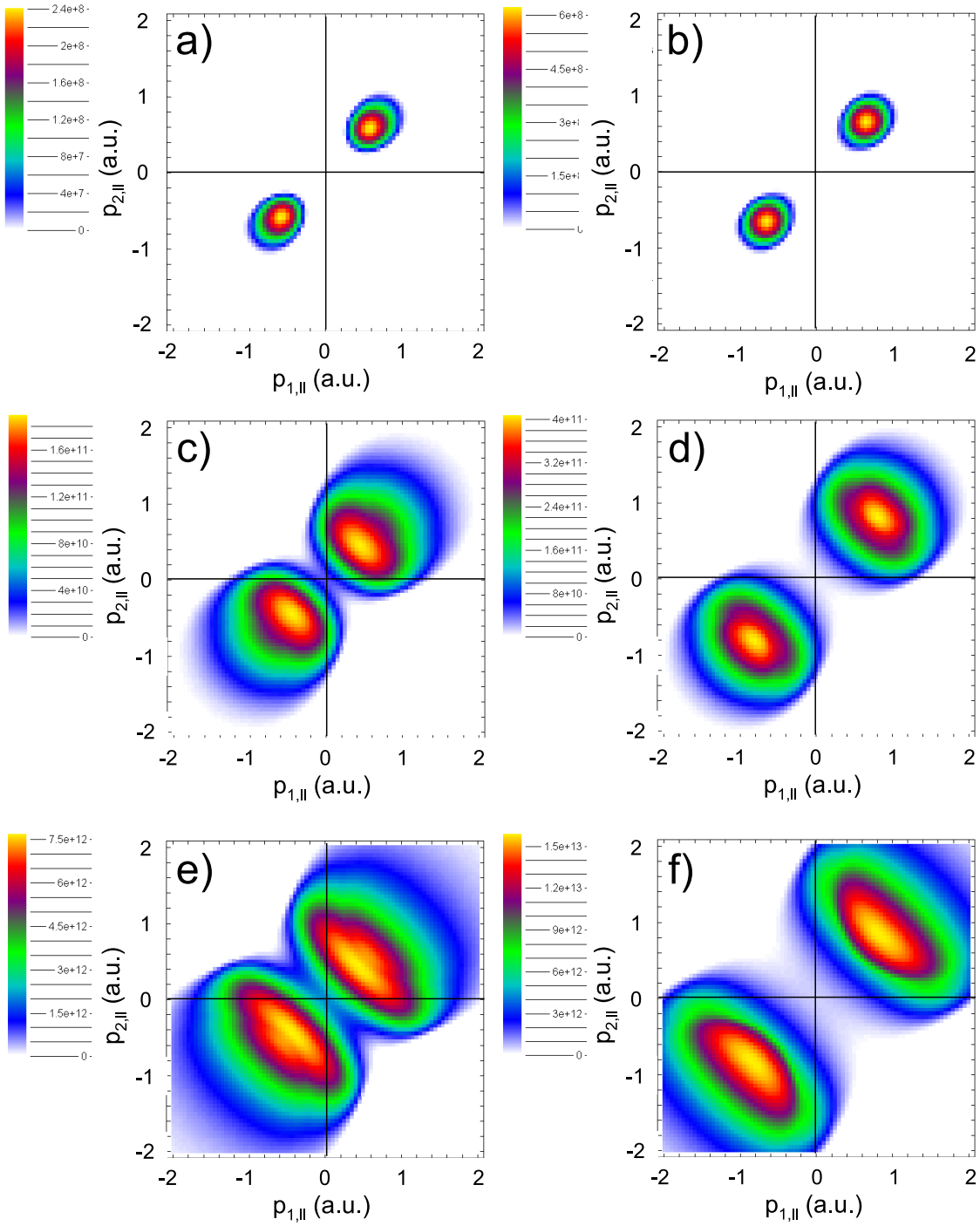

Fig. 4.12: e^--e^- momentum correlation for the longitudinal momentum components obtained by our semiclassical model calculation using the velocity gauge (left panel) and the length gauge (right panel). The light intensities are: 0.9×10^{14} W/cm^2 (a,b); 1.5×10^{14} W/cm^2 (c,d); 2.4×10^{14} W/cm^2 (e,f).

More recently it has been argued, that the difference in the shape of the electron sum-momentum distributions, for Ar and He on one hand and for Ne on the other hand, appears due to the atom specific relative contribution of impact excitation and impact ionization to NSDI [97]. Indeed, the dependence of the total excitation and ionization cross sections on the kinetic energy of the recolliding electron shows, that the first dominates over the second for Ar^+ and He^+, while the opposite is the case for Ne^+ in a large range of energies. One may expect that this gives rise to different contributions to NSDI from the two ionization mechanisms. As a result, different sum-momentum distributions are observed. Although this model explains well the experimental results, its relevance is questionable since it is based on total instead of differential cross sections. The latter are more realistic but difficult to include.

The e^- impact excitation-electric field ionization mechanism for NSDI is strictly speaking sequential. The second electron is ionized by the electric field of the light wave from an excited state at a later time and not simultaneously as in the impact ionization mechanism. As we have seen in Figs. 4.2 and 4.5, the photoelectron pairs arising from impact excitation-field ionization start to dominate the e^--e^- momentum distribution with decreasing light intensity. At low intensity, where the kinetic energy of the returning electron is not high enough for direct impact ionization, only impact excitation followed by field ionization should contribute to NSDI. With increasing intensity the probability for electron impact ionization grows. On the other hand the lifetimes of excited states of Ar^+ should decrease in a stronger field. As a result both electrons in the excitation-field ionization pathway are also emitted almost simultaneously giving rise to the similar momenta. This idea has been drawn from the calculations for He by van der Hart [135]. It allows one to explain the intensity dependent features of the impact excitation-field ionization we found for the Ar data.

In conclusion of this chapter it can be stated that our semiclassical calculations based on the rescattering model agree qualitatively well with our experimental results for Ar and Ne. Our model is able to reproduce the momentum correlation spectra with the distinctive features of the instantaneous electron impact ionization. Among other theoretical models the most successful are the quantum-mechanical S-matrix calculations applying three-body contact interaction [87, 85, 90] as well as the most complete semiclassical trajectory calculation with the full three-body Coulomb interaction [99, 100]. A quantitative disagreement of the existing theoretical results with experiment is not surprising in view of the approximations made. Till now no complete quantum-mechanical calculation has been performed at the relevant wavelength and for complex atomic systems like Ar and Ne.

We observed the footprint of instantaneous electron impact ionization in the

light intensity region, where it is forbidden within the classical rescattering model. This can be explained by taking a lowering of the unperturbed ionization potential of the singly charged ion in the external electric field of the light wave at the instant of recollision into account. The light field thus essentially influences the rescattering process. The dependence of the transverse electron sum-momentum distribution $f(p_\perp)$ on light intensity we found experimentally may indicate that this is also the case at high light intensities, where $E_{kin,max} \gg I_p^+$. An alternative way of understanding the observed impact ionization "below" threshold is to assume that the collision complex which forms when the electron returns to the ion core absorbs photons. If a sufficient number is absorbed the internal energy suffices for instantaneous double ionization of the atom.

Comparing Ar to Ne data atom specific features appear. For Ne the instantaneous electron impact ionization prevails in a large range of light intensities, from the classical threshold I_p^+ to far above, as a comparison with previous results shows [131]. In the case of Ar, a second ionization mechanism, which is believed to be electron impact excitation with subsequent electric field ionization, competes with the first one and dominates with decreasing light intensity.

5. Molecules in high-intensity ultra-short laser pulses

In the previous chapter the experimental results on non-sequential double ionization of atoms in high-intensity ultra-short laser pulses have been presented and discussed. The present chapter is dedicated to molecules, in particular to N_2 and O_2.

There are several differences between molecules and atoms that might be relevant for the ionization dynamics in a strong laser field. The presence of several nuclear centers may lead to new interference effects between electron wave packets emitted at different nuclei. Moreover, the symmetry of the ground state orbitals occupied by the valence electron (e.g. bonding or antibonding) may have an effect on the ionization process. Finally, the orientation of the molecular axis with respect to the electric field of the light wave changes the effective potential that the valence electron experiences during photoionization. So far, only a few experiments have addressed these questions and the theory is not as developed as it is for atoms.

5.1 Introduction

Similar to atoms, several homonuclear and heteronuclear molecules show an excessive double ionization probability observed in integral measurements of the doubly charged ion yield [136, 58, 59, 137, 138]. This fact indicates that double ionization of molecules may also proceed non-sequentially. However, the total ion yield data are not sufficient to identify the ionization mechanism in detail.

A study of the dependence of double ionization on the ellipticity of the light polarization may provide a clue on the NSDI mechanism, such as the suppression of the doubly charged ion yield in elliptically polarized light found for atoms. For example, for the benzene molecule (C_6H_6) the dependence of the doubly to singly charged ion yield ratio on the ellipticity indicated that NSDI is due to electron recollision [139].

Electron rescattering, which is the main mechanism of atomic NSDI, was recently reported for molecular hydrogen [140] and also for D_2 [141, 142]. The high-energy protons (and D^+ ions) observed in these experiments were interpreted either as the outcome of rescattering excitation of the singly charged molecular ion followed by

its dissociation or as coming from rescattering-induced ionization. Based on these experimental findings one may thus expect that electron rescattering is the general mechanism of molecular NSDI.

In this chapter we study double ionization of N_2 and O_2 by means of momentum spectroscopy in order to identify the non-sequential mechanism. We also investigate molecule specific effects on the final electron momentum correlation. In a recollision double ionization process the probability of ionization depends primarily on the external electric field strength and on the ionization energy of the system. Since N_2 and Ar have the same ionization potentials, and O_2 has the same ionization potential as Xe, one would expect similar double ionization behavior of the corresponding molecular and atomic systems. A direct comparison of molecules with their atomic "companions" allows one to clarify the influence of the molecular structure on the ionization dynamics and to resolve the question whether the molecular double ionization mechanism is the same as that for atoms.

Recent single ionization experiments with N_2 and O_2 have shown that N_2 behaves like Ar, while O_2 and Xe, despite their similar ionization potentials, clearly differ. The difference has been observed in the total ion yield measurement as a function of light intensity, where the signal for the O_2 molecule was strongly suppressed compared to that for Xe [59, 143]. In above-threshold ionization (ATI) spectra [144] a reduced electron yield has been found for O_2 at low and high electron kinetic energy compared to corresponding ATI spectra of Xe, whereas the spectra of N_2 and Ar looked similar. These effects have been attributed to the different symmetry of the ground state orbitals occupied by the valence electron (σ_g, bonding for N_2 and π_g, antibonding for O_2) [144, 145]. In a diatomic molecule, quantum interference effects of electron wave packets emitted at the two nuclear centers may occur. A destructive interference appears in case of antibonding symmetry of the active molecular orbital. It results in a suppression of molecular ionization and a reduced production of low-energy electrons in the ATI spectrum compared to an atomic system with the same ionization potential.

A simple semiclassical model for double ionization of molecules based on electron recollision will be developed in this chapter. It takes into account the symmetry of the initial state orbitals occupied by the valence electron. Thus, we can directly compare our experimental results with model calculations in order to understand the influence of the initial state symmetry on molecular double ionization and the role of interference effects.

5.2 The electron sum-momentum distributions for N_2 and O_2

As we have seen in the previous chapter about NSDI of atoms, the sum-momentum distribution of the two photoelectrons for the momentum component parallel to the polarization direction of the laser beam provides an obvious indication of the ionization mechanism. We performed these measurements for N_2 and O_2 in order to identify the NSDI mechanism for diatomic molecules.

Fig. 5.1 shows these distributions for N_2 (left panel) and O_2 (right panel) at different light intensities. The laser field strengths were chosen in a regime where NSDI has been reported to predominate [59, 137]. The upper two distributions were obtained at light intensities where, within the rescattering model, the maximum kinetic energy of the recolliding electron is not enough for direct e^- impact ionization of the singly charged ion. As can be seen, at all intensities used in the experiment, both N_2 as well as O_2 do not exhibit the double hump structure in the momentum distribution which is considered to be characteristic for NSDI due to recollision. However, we have already seen for Ar that the absence of the pronounced double hump structure in the $f(p_\parallel)$ distribution does not necessarily mean the absence of NSDI by electron recollision. The Gauss-like functional form of the O_2 distributions does not change with increasing laser field strength from below the ionization threshold (1.3×10^{14} W/cm^2 in Fig. 5.1 (b)) to far above (2.2×10^{14} W/cm^2 in Fig. 5.1 (h)). The width of the distribution just becomes broader. In contrast, the N_2 distributions exhibit a narrow plateau which develops to a Gaussian distribution only at the highest light intensity.

A further characteristic of NSDI via rescattering is a dependence of the cutoff momentum of $f(p_\parallel)$ on the ponderomotive potential U_p which follows a $4\sqrt{U_p}$ rule. A relation like this is expected for instantaneous electron impact ionization of atoms (see Sec. 4.3). Fig. 5.2 shows the experimentally observed cutoff momenta for N_2 (filled squares) and O_2 (open circles) and also the function $4\sqrt{U_p}$ for comparison. Three experimental points for N_2 are located close to the curve $4\sqrt{U_p}$ and have the same trend with light intensity. Only at the highest intensity 2.5×10^{14} W/cm^2 the data point deviates from the common tendency being located far below the curve. At this laser intensity the corresponding momentum distribution $f(p_\parallel)$ is dominated by electrons with momenta close to zero. Thus, from the dependence of the cutoff momentum on the laser intensity we find a first signature of instantaneous e^- impact ionization for N_2, except for the highest intensity. A full match of the data points with the curve $4\sqrt{U_p}$ cannot be expected since the sum-momentum distributions in Fig. 5.1 include contributions from electrons which are not coming from the e^- impact ionization channel. These electrons may result in a sum-momentum distribution with maximum at $p_\parallel = 0$. Consequently, the cutoff momentum determined from the

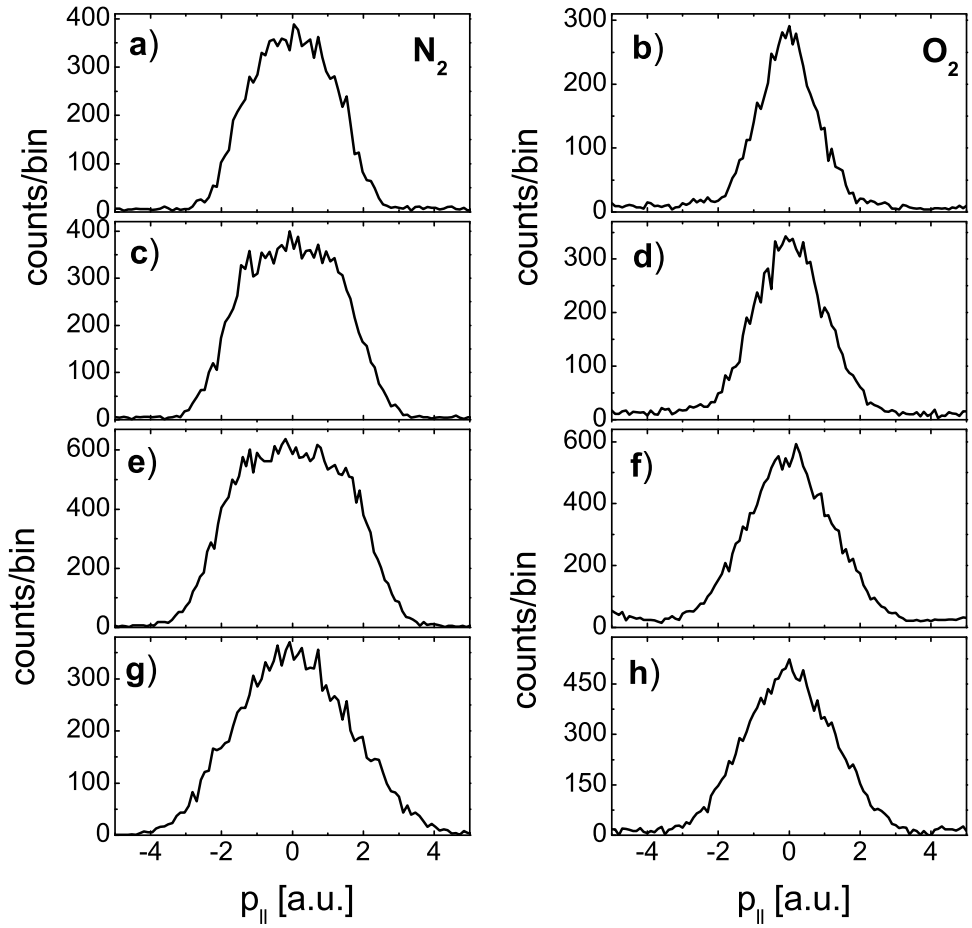

Fig. 5.1: Electron sum-momentum distributions after double ionization projected onto an axis parallel to the laser beam polarization vector. Left panel: N_2 at light intensities 1.3×10^{14} W/cm^2 (a), 1.5×10^{14} W/cm^2 (c), 1.8×10^{14} W/cm^2 (e), 2.5×10^{14} W/cm^2 (g); Right panel: O_2 at 1.1×10^{14} W/cm^2 (b), 1.7×10^{14} W/cm^2 (d), 1.9×10^{14} W/cm^2 (f), 2.2×10^{14} W/cm^2 (h).

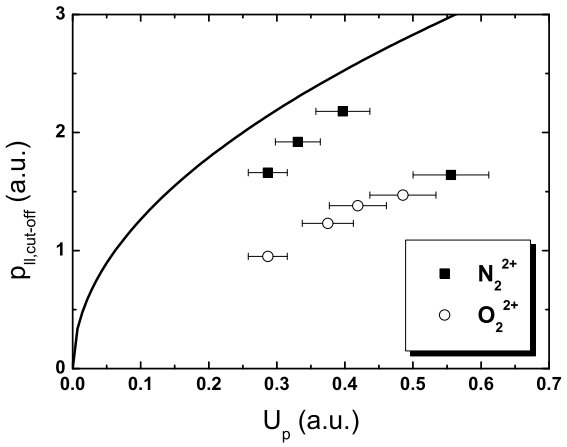

Fig. 5.2: The dependence of the cutoff momentum of the N_2 and O_2 momentum distributions on the light intensity. The data have been extracted from Fig. 5.1. The error bars denote the uncertainty in the determination of the light intensity. The solid line represents the function $4\sqrt{U_p}$.

full sum-momentum distribution is smaller than $4\sqrt{U_p}$.

For O_2, all data points are far below the $4\sqrt{U_p}$ curve. The cutoff momenta for O_2 are about half of the corresponding cutoff momenta for N_2. This indicates, at first sight, that electrons which determine the cutoff momentum do not result from instantaneous e^- impact ionization. In Sec. 5.5 we will show, however, that e^- impact ionization of a molecule like O_2 may give rise to a narrow sum-momentum distribution with a small cutoff momentum.

Summarizing our measurements of the electron sum-momentum distribution for N_2 and O_2, the double-hump structure found for atoms has not been observed for molecules. However, for N_2 the width of the distribution indicates a significant contribution of instantaneous electron impact ionization.

5.3 e^- - e^- momentum correlation for N_2 and O_2

Since the momentum correlation spectra of the two photoelectrons provide the most complete information about the NSDI dynamics, we expect to find other signatures of electron impact ionization for N_2 and to understand the reason for the observed e^- sum-momentum distributions for both, N_2 and O_2.

Fig. 5.3 shows these spectra for N_2 at 1.5×10^{14} W/cm^2 and for O_2 at three

different laser intensities. The spectra are shown for the momentum component parallel to the laser polarization direction.

In the previous chapter we have discussed that electrons emitted from atoms during NSDI to the same half-space along the polarization direction give rise to the two maxima on the main diagonal in the momentum correlation spectrum (first and third quadrants). Moreover this is the main signature of instantaneous electron impact ionization [68, 69].

In Fig. 5.3 (b) we observe such maxima for N_2, where the two photoelectrons are emitted preferentially with similar momentum components ($p_{1,\parallel} = p_{2,\parallel}$). However, significantly more electron pairs with small momenta ($p_{i,\parallel} \approx 0, i = 1, 2$) are found for N_2 in comparison with its atomic companion Ar at the same light intensity (see Fig. 4.2 (b)). We will show in the next section that these pairs may be attributed to rescattering impact ionization of N_2^+. The final momentum correlation of this NSDI mechanism is thus decisively influenced by the molecular structure. Similar to Ar, those electron pairs in the 2nd and 4th quadrants of Fig. 5.3 (b) found significantly off the main diagonal have to be attributed to rescattering electron impact excitation of N_2^+ with subsequent electric field ionization of the excited electron [69].

In contrast, the momentum correlation spectra for O_2 do not show any characteristics expected for rescattering impact ionization (Fig. 5.3 (a,c,d)). At all laser intensities in our experiment the momentum correlation for O_2 has a homogeneous distribution with a maximum close to zero momentum. Such a distribution is usually characteristic for sequential double ionization. However, we have noted earlier that the light intensities in our experiment were chosen in the regime where NSDI is expected. Therefore a possible conclusion is that the molecular structure modifies the final state momentum correlation of NSDI significantly.

To give the main points of our measurements of the e^--e^- momentum correlation for N_2 and O_2, we observed the typical structures of the electron impact ionization for N_2 but not for O_2. Moreover, the significant contribution of electron pairs at zero momentum found for both molecules is an evidence of the strong influence of the molecular structure on the final electron momentum correlation.

In the next section we will develop simple models which allow us to test both, the possibility of rescattering NSDI for N_2 and O_2 molecules as well as the sequential double ionization scenario for O_2.

5.4 Modeling of sequential ionization

In order to clarify whether the reason for the observed momentum distributions for O_2 is sequential ionization, we first calculate electron sum-momentum distributions expected from this mechanism.

Our semiclassical model is based on the KFR approximation as applied by

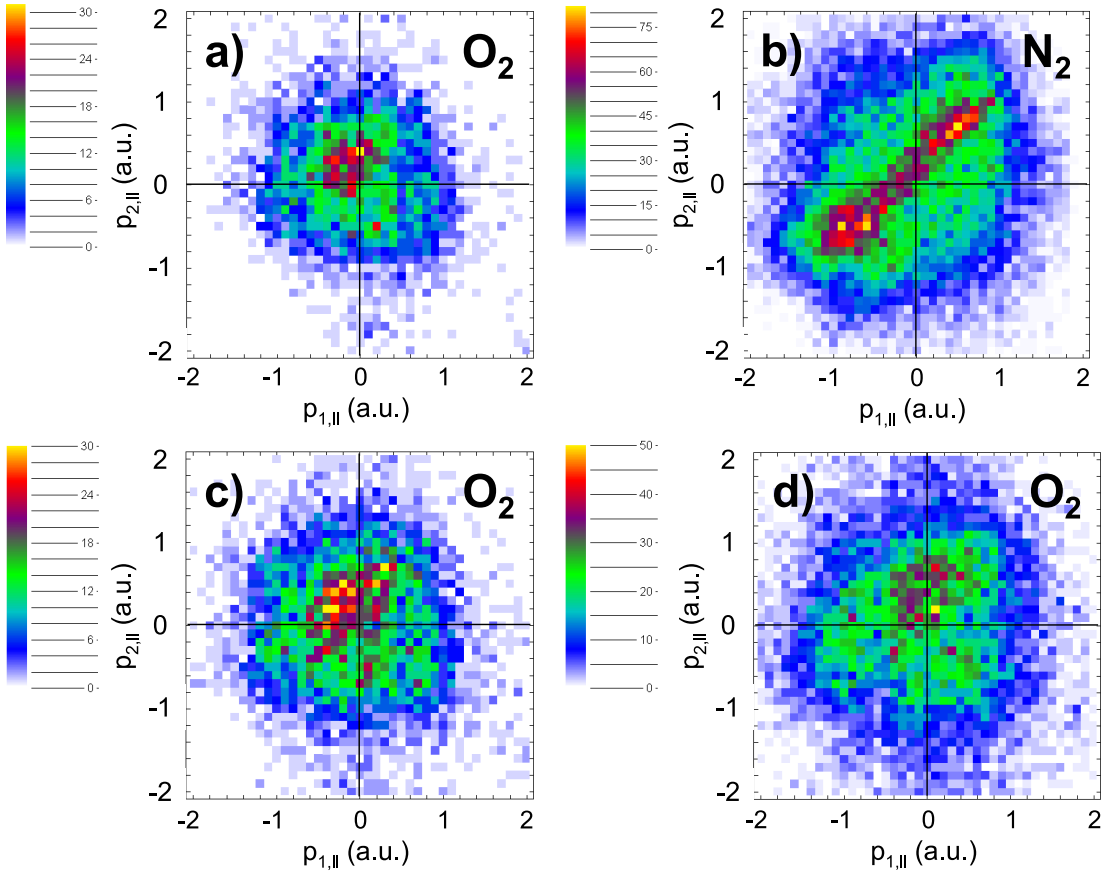

Fig. 5.3: e^--e^- momentum correlation (longitudinal projection on the light polarization axis) for N_2 at 1.5×10^{14} W/cm^2 (b) and for O_2 at 1.1×10^{14} W/cm^2 (a), at 1.7×10^{14} W/cm^2 (c) and at 2.2×10^{14} W/cm^2 (d).

Smirnov and Krainov [146, 147] to the H_2^+ molecular ion. Quasistatic electric field ionization is assumed for both ionization steps. The symmetry of the initial state orbital occupied by the valence electron is included in the calculation, however in a simplified way. Averaging over the randomly oriented internuclear axis was performed. This is allowed since the 35 fs laser pulses do not align the molecule.

Generally, molecules can be aligned by a linearly polarized low-frequency intense laser field due to the torque on the laser-induced molecular dipole moment [148, 149, 150]. For short laser pulses, alignment will be important for the ionization process if it occurs on a time scale comparable with the laser pulse duration. As has been shown in [151], for a given laser field strength E_0 the alignment time τ of N_2 and O_2 can be estimated based on the scaling law $\tau \propto \sqrt{\mu/R}/E_0$ found by Bandrauk and Ruel [152] in their calculations for H_2^+. Here, R is the internuclear separation and μ

is the molecular reduced mass. In our case the estimated shortest alignment times for N_2 and O_2 are assured to be longer than the pulse duration of 35 fs.

In our models we also assume a fixed internuclear separation. This simplification seems reasonable since for O_2 and N_2 as well as for the respective singly charged ions the periods of molecular vibration are several times longer then the optical cycle of the laser field (2.7 fs).

Let $f_1(\vec{p}_1)$ and $f_2(\vec{p}_2)$ be the momentum distribution functions of the two photoelectrons after stepwise double ionization. They are independent for sequential ionization. Therefore the sum-momentum distribution can be written as a convolution integral of the two distribution functions

$$\begin{aligned} g(\vec{p}) &= \int f_1(\vec{p}_1) \cdot f_2(\vec{p}_2) \cdot \delta^3(\vec{p} - \vec{p}_1 - \vec{p}_2) d^3\vec{p}_1 d^3\vec{p}_2 \\ &= \int f_1(\vec{p}_1) \cdot f_2(\vec{p} - \vec{p}_1) d^3\vec{p}_1, \end{aligned} \tag{5.1}$$

where $\vec{p} = \vec{p}_1 + \vec{p}_2$. We are interested in the distribution of the sum-momentum component $p_\parallel$ parallel to the light polarization direction for a direct comparison with the experimentally observed distributions in Fig. 5.1

$$g(p_\parallel) = \int g(\vec{p}) d^2\vec{p}_\perp = \iint f_1(\vec{p}_1) \cdot f_2(\vec{p} - \vec{p}_1) d^2\vec{p}_\perp d^3\vec{p}_1. \tag{5.2}$$

The momentum distribution $f_i(\vec{p}_i)$ of each electron is given by

$$f_i(\vec{p}_i) = \omega_0 \sin^2\left(\frac{\vec{p}_i \vec{R}}{2}\right) e^{-\alpha_{i\parallel} p_{i\parallel}^2 - \alpha_{i\perp} p_{i\perp}^2}, \tag{5.3}$$

with

$$\alpha_{i\parallel} = \frac{\omega^2 (2I_{p,i})^{2/3}}{3E^3}; \qquad \alpha_{i\perp} = \frac{(2I_{p,i})^{1/2}}{E} \quad [129]. \tag{5.4}$$

Here, ω is the laser field frequency, $I_{p,i}$ is the ionization potential of O_2 ($i = 1$) and O_2^+ ($i = 2$) respectively, E is the amplitude of the electric field of the light wave, and $\vec{R}$ is the vector of the internuclear separation. The sin term in Eq. (5.3) takes the antibonding symmetry of the valence molecular orbital into account [144, 145]. In Eq. (5.3) ω_0 only determines the maximum value of the distribution while it has no influence on its shape.

After integration in Eq. (5.2) we obtain:

$$\begin{aligned} g(p_\parallel) &= 1+\frac{1}{2}\cos\left(p_\parallel R_\parallel\right)e^{-\frac{1}{4}(\frac{1}{\alpha_{1\perp}}+\frac{1}{\alpha_{2\perp}})R_\perp^2} \\ &\quad -\cos\left(\frac{\alpha_{1\parallel}}{\alpha_{1\parallel}+\alpha_{2\parallel}}p_\parallel R_\parallel\right)e^{-\frac{R_\perp^2}{4\alpha_{2\perp}}-\frac{R_\parallel^2}{4(\alpha_{1\parallel}+\alpha_{2\parallel})}} \\ &\quad -\cos\left(\frac{\alpha_{2\parallel}}{\alpha_{1\parallel}+\alpha_{2\parallel}}p_\parallel R_\parallel\right)e^{-\frac{R_\perp^2}{4\alpha_{1\perp}}-\frac{R_\parallel^2}{4(\alpha_{1\parallel}+\alpha_{2\parallel})}} \\ &\quad +\frac{1}{2}\cos\left(\frac{\alpha_{1\parallel}-\alpha_{2\parallel}}{\alpha_{1\parallel}+\alpha_{2\parallel}}p_\parallel R_\parallel\right)e^{-\frac{1}{4}(\frac{1}{\alpha_{1\perp}}+\frac{1}{\alpha_{2\perp}})R_\perp^2-\frac{R_\parallel^2}{\alpha_{1\parallel}+\alpha_{2\parallel}}}. \end{aligned} \tag{5.5}$$

Here $R_\parallel$ and $R_\perp$ are projections of $\vec{R}$ onto the axis parallel and perpendicular to the electric field direction respectively.

Finally we average over all possible orientations of the internuclear axis with respect to the external electric field:

$$\bar{g}(p_\parallel) = \int_0^{2\pi}\int_0^{\pi} g(p_\parallel)\, sin\theta\, d\theta\, d\varphi. \tag{5.6}$$

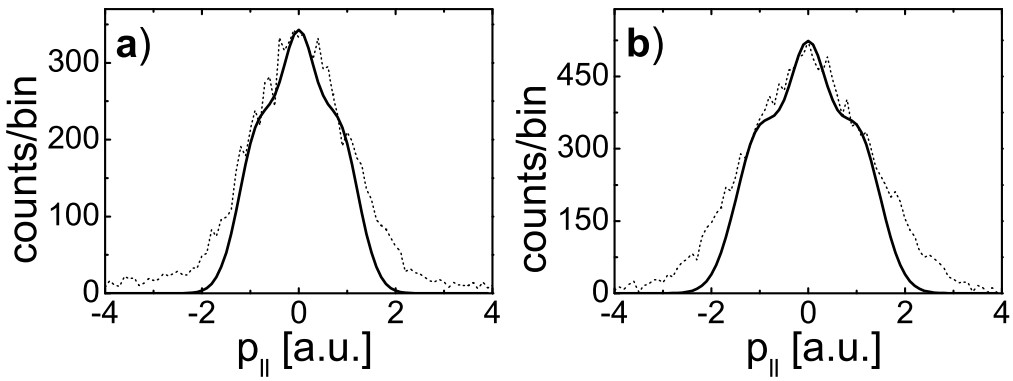

Fig. 5.4: Electron sum-momentum distribution calculated for sequential double ionization of O_2 (solid line) compared with the corresponding experimental results (dashed line): (a) at 1.7×10^{14} W/cm^2, (b) at 2.2×10^{14} W/cm^2.

Fig. 5.4 shows the results of our calculation for sequential double ionization of O_2 at two light intensities (solid lines). The dashed lines are the sum-momentum

distributions obtained in the experiment (Fig. 5.1). Obviously, the theoretical distributions are narrower than the experimental ones.

The theoretical approach stated above is known to *overestimate* the width of the momentum distribution when applied to sequential ionization of atoms. If the O_2 molecule in our experiment is ionized sequentially one would therefore expect that the experimental width of the electron sum-momentum distribution is narrower than the theoretical one. From this we conclude that the double ionization of O_2 does not proceed sequentially. Despite the absence of any characteristics of NSDI, double ionization of the O_2 molecule is thus expected to be non-sequential! The question, however, remains whether recollision is the underlying ionization mechanism.

5.5 NSDI model calculation for molecules

Let us now assume that the main mechanism for molecular NSDI is recollision. We will test this hypothesis by comparing the theoretical and experimental data. The theoretical model includes the recollision scenario as well as the symmetry of the initial state orbitals of the valence electrons in the molecule. If correct, the model should be able to reproduce the qualitative differences in the sum-momentum distributions and final electron momentum correlations for N_2 and O_2.

The calculation is based on a classical analog of the quantum mechanical S-matrix for recollision double ionization [91, 87]. The model has been described in detail in the previous chapter on atoms (Sec. 4.5). According to this, the differential probability for double ionization $|S(\vec{p}_1, \vec{p}_2)|^2$ is proportional to a form factor $|V_{\vec{p}_1,\vec{p}_2,\vec{k}}|^2$ [90]. In case of molecules only the form factor in Eq. (4.7) will change, depending on the molecular structure and the type of electron interaction at recollision.

We factorize the form factor into a contribution $g_1(\vec{k})$ describing the transition of the first electron to the continuum and a second contribution $g_2(\vec{p}_1, \vec{p}_2, \vec{k})$ describing the inelastic recollision

$$|V_{\vec{p}_1,\vec{p}_2,\vec{k}}|^2 = |g_1(\vec{k}) \cdot g_2(\vec{p}_1, \vec{p}_2, \vec{k})|^2. \tag{5.7}$$

$\vec{p}_1$ and $\vec{p}_2$ are the final state momenta of the two photoelectrons and $\vec{k}$ is the intermediate state momentum of the recolliding electron.

The inelastic scattering matrix element g_2 is calculated in Born approximation for the transition of the second electron bound in the single particle orbital $\psi_2(\vec{x})$ to the continuum upon recollision of the first electron

$$g_2(\vec{p}_1, \vec{p}_2, \vec{k}) = \int d^3\vec{x}\, d^3\vec{x}'\, e^{-i\vec{p}_1\vec{x} - i\vec{p}_2\vec{x}'} V_e(\vec{x}, \vec{x}')\, e^{i\vec{k}\vec{x}}\, \psi_2(\vec{x}'). \tag{5.8}$$

The wave function of the bound electron $\psi_2(\vec{x})$ is constructed by the method of linear combination of atomic orbitals (LCAO) for bonding (g) and antibonding (u)

molecular orbitals

$$\psi_{2,g} = c_1 \frac{e^{-\kappa r_1}}{r_1} + c_2 \frac{e^{-\kappa r_2}}{r_2},$$
$$\psi_{2,u} = c_1 \frac{e^{-\kappa r_1}}{r_1} - c_2 \frac{e^{-\kappa r_2}}{r_2}. \tag{5.9}$$

Here, c_1 and c_2 are normalization constants which are determined by the internuclear separation $|\vec{R}|$. The binding energy $\frac{\kappa^2}{2} = E_b$ defines κ. The interaction of the two nuclei with the bound electron is described by means of a δ-potential

$$V(\vec{r}) = V_0 \left(\delta(\vec{r}_1) \frac{\partial}{\partial r_1} r_1 + \delta(\vec{r}_2) \frac{\partial}{\partial r_2} r_2 \right). \tag{5.10}$$

Here, $\vec{r}_1$ and $\vec{r}_2$ are vectors pointing from the respective nuclear centers to the electron.

In this way we have constructed a simple model molecule which incorporates the main features of a real homonuclear molecule, in particular the two-center effect. As a consequence, the molecular orbital of our model molecule is either σ_g (bonding) or σ_u (antibonding). Although the relevant O_2 orbital is not a σ_u one, it nevertheless reflects main features of the initial state symmetry, and thus allows one to test the statement that the symmetry of the initial valence orbital is decisive. The electron-electron interaction $V_e(\vec{x}, \vec{x}')$ at the instant of recollision is assumed to be a contact interaction

$$V_e(\vec{x}, \vec{x}') = V_0 \delta(\vec{x} - \vec{x'}) \frac{\partial}{\partial |\vec{x} - \vec{x'}|} |\vec{x} - \vec{x'}|. \tag{5.11}$$

With these approximations, g_2 reads explicitly

$$g_{2,g/u}(\vec{p_1}, \vec{p_2}, \vec{k}) = \frac{h_{2,g/u}(|\vec{R}|)}{2I_p^+(t) + (\vec{k} - \vec{p}_1 - \vec{p}_2)^2} \begin{cases} \cos \frac{(\vec{k} - \vec{p_1} - \vec{p_2})\vec{R}}{2} & (g) \\ \sin \frac{(\vec{k} - \vec{p_1} - \vec{p_2})\vec{R}}{2} & (u), \end{cases} \tag{5.12}$$

where $h_{2,g/u}$ is a function of the internuclear separation $|\vec{R}|$ alone. It has a constant value, since $|\vec{R}|$ is assumed fixed in our model, and thus does not influence the properties of the momentum distribution . $I_p^+(t)$ is the time dependent ionization potential of the singly charged ion in the external electric field of the light wave (see Eq. (4.4)).

The transition matrix element of the first electron from the ground state of the molecule to the ionization continuum is split into an ionization rate part $R(t)$ and a geometry part g_1. The ionization rate $R(t)$ is calculated similar to that for atoms using the ADK tunneling rate [10]. The geometry part g_1 is incorporated in the form factor and is given by

$$g_1(\vec{k}) = \int d^3\vec{x}\, e^{-i\vec{k}\vec{x}}\, V(\vec{x})\, \psi_1(\vec{x}), \tag{5.13}$$

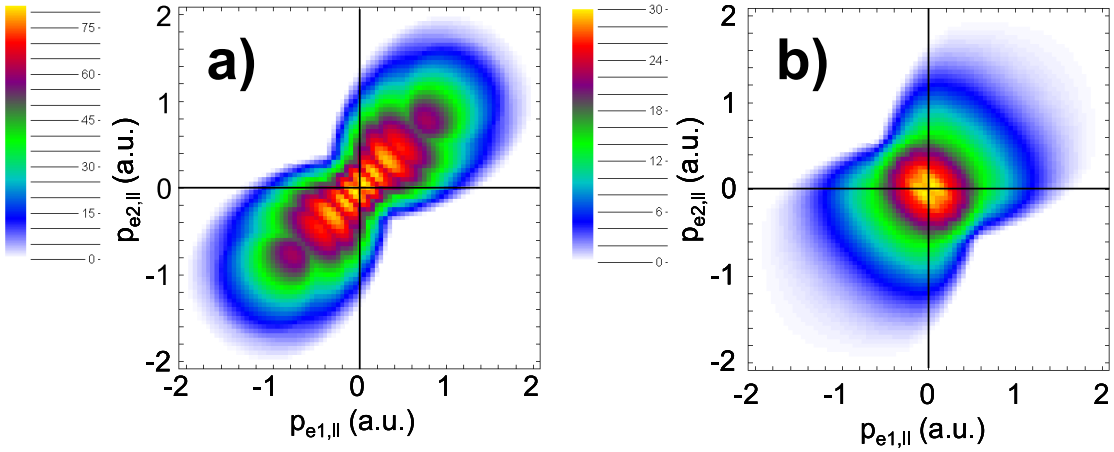

Fig. 5.5: Calculated e^--e^- momentum correlation for the model molecules: (a) N_2 at 1.5×10^{14} W/cm^2; (b) O_2 at 1.7×10^{14} W/cm^2.

where $V(\vec{x})$ is the interaction potential of the active electron with the singly charged ion core (see Eq. (5.5)). $\psi_1(\vec{x})$ is the wave function of the valence orbital occupied by the electron removed first to a plane wave intermediate Volkov state. $\psi_1(\vec{x})$ is constructed in the same way as $\psi_2(\vec{x})$ using the LCAO method. The term g_1 then appears as an intermediate state interference term

$$g_{1,g/u}(\vec{k}) = h_{1,g/u}(|\vec{R}|) \begin{cases} \cos\frac{\vec{k}\vec{R}}{2} & (g) \\ \sin\frac{\vec{k}\vec{R}}{2} & (u). \end{cases} \tag{5.14}$$

In Eqs. (5.12) and (5.14), the subscript (g) is for the σ_g and (u) for the σ_u valence orbital. Finally, we average again over all orientations of the internuclear axis of the molecule.

The calculated electron momentum correlation after NSDI is shown in Fig. 5.5 for N_2 at the light intensity of 1.5×10^{14} W/cm^2 (a) and for O_2 at 1.7×10^{14} W/cm^2 (b). These theoretical results can be compared to the corresponding experimental data at the same light intensities in Fig. 5.3 (b,c). For N_2, we find a correlation similar to that observed in the experiment with a significant amount of electron pairs with small and similar momenta $p_{ei,\parallel}$, $i = 1, 2$. The calculation for N_2 clearly shows an electron momentum correlation that is different from that of Ar at the same light intensity (Fig. 4.10 (a)). Thus, compared to the corresponding atom the presence of the two atomic centers in a molecule leads to a significantly different electron momentum correlation in the final state after NSDI at the same light intensity. The calculation also indicates that the specific "sausage" shape of the N_2 distribution is mainly determined by final state interference through the matrix

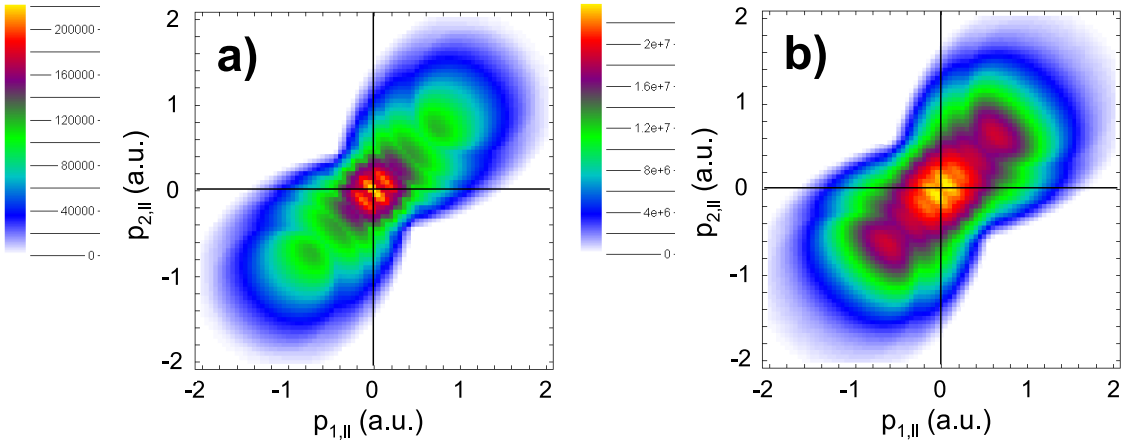

Fig. 5.6: e^--e^- momentum correlation calculated with $g_1(\vec{k}) = 1$ in Eq. (5.7) for model molecules: (a) N_2 at 1.5×10^{14} W/cm^2; (b) O_2 at 1.7×10^{14} W/cm^2.

element $g_{2,g}(\vec{p_1}, \vec{p_2}, \vec{k})$ (5.12). In contrast, $g_{1,g}(\vec{k})$ has only little effect on the final momentum correlation. To demonstrate this we assume $g_1 = 1$. Fig. 5.6 (a) shows the e^--e^- momentum correlation calculated at 1.5×10^{14} W/cm^2 for $g_1 = 1$. The specific shape of the distribution is quite similar to that in Fig. 5.5 (a).

For the model molecule corresponding to O_2 an electron momentum correlation significantly different from N_2 is found (Fig. 5.5 (b)). Despite the slightly higher light intensity, it is concentrated near $p_{e1,\|} = p_{e2,\|} = 0$. This is in agreement with the experimental finding at the same light intensity (Fig. 5.3 (c)). The $g_{1,u}(\vec{k})$ matrix element is found to be responsible for the electron momentum correlation which is localized at zero momentum for O_2. The sin term in Eq. (5.14) leads to a reduction of recollision electrons with small $\vec{k}$. They are emitted near the extrema of the oscillating electric field, where the tunnel ionization probability is maximum. These electrons with small momenta $\vec{k}$ in the intermediate state are mainly responsible for the emission of final state electrons with large $p_{ei,\|}$. The predominant influence of the sin term in Eq. (5.14) on the final state electron momenta can easily be seen if we compare the e^--e^- momentum correlation in Fig. 5.5 (b) with that in Fig. 5.6 (b), where $g_1 = 1$ is assumed. The distribution with $g_1 = 1$ becomes stretched along the diagonal $p_{e1,\|} = p_{e2,\|}$. Thus, different from N_2, the antibonding initial state symmetry of the model molecule corresponding to O_2 shows up mainly through the $g_{1,u}(\vec{k})$ matrix element.

A full quantitative agreement between the experiment and the model calculation is not expected because of the simplicity of the model. In a certain range of laser intensities our model correctly reproduces the qualitative difference between the two molecular systems with bonding and antibonding initial state symmetry. Fig. 5.7

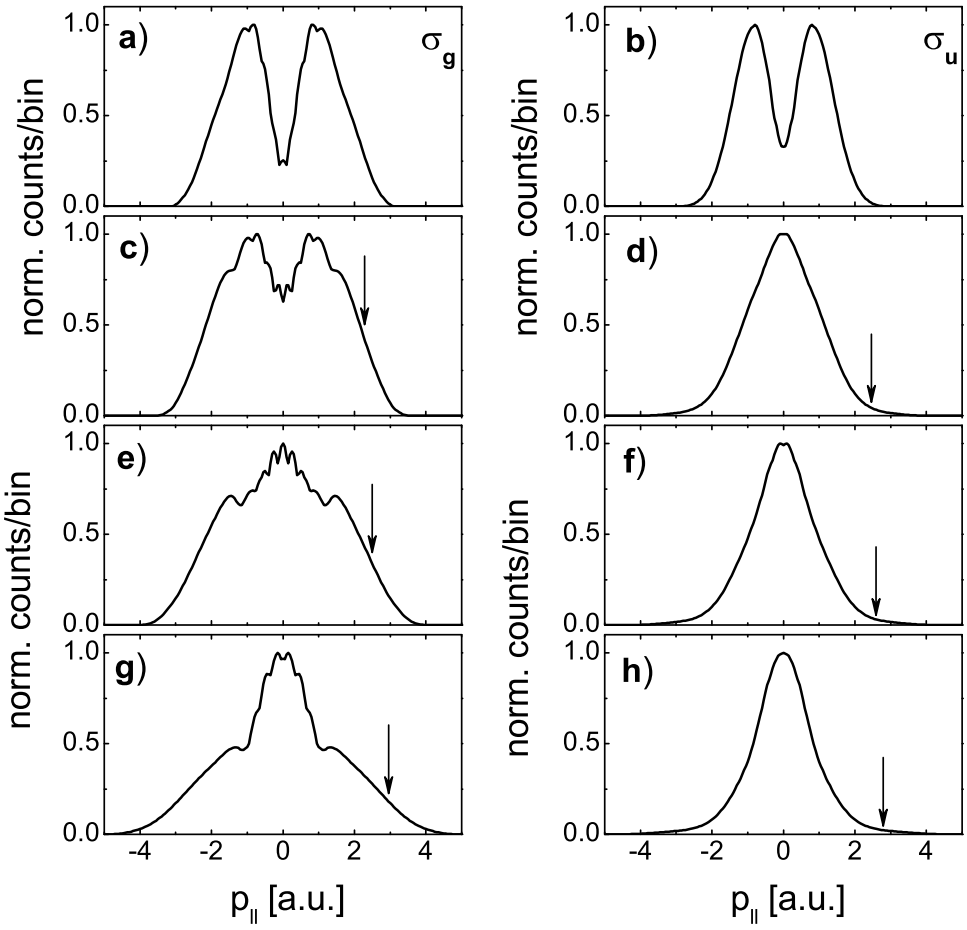

Fig. 5.7: Calculated electron sum-momentum distributions for N_2 (a,c,e,g) and O_2 (b,d,f,h) model molecules at the same light intensities as in Fig. 5.1. The arrows are located at $p_{\|} = 4\sqrt{U_p}$.

shows the results of the model calculation for the sum-momentum distributions of the two photoelectrons produced in NSDI. Similar to real N_2 and O_2 molecules, the width of the momentum distribution for the σ_g initial state molecular orbital is about $4\sqrt{U_p}$ and about twice as large as that for the σ_u orbital. Moreover, our model calculation reproduces qualitatively the main tendency of the sum-momentum distribution for N_2 with increasing light intensity, including its strong change in shape at 2.5×10^{14} W/cm^2 (compare Fig. 5.7 and Fig. 5.1).

In case of O_2, the deviations between our calculations and the experimental results become stronger with increasing light intensity. The calculated sum-momentum distribution narrows rather than broadens. The main reason for this is suspected in the initial state symmetry of the valence molecular orbital, which is taken as σ_u and not the correct π_g. A further reason is probably the approximation for the instant

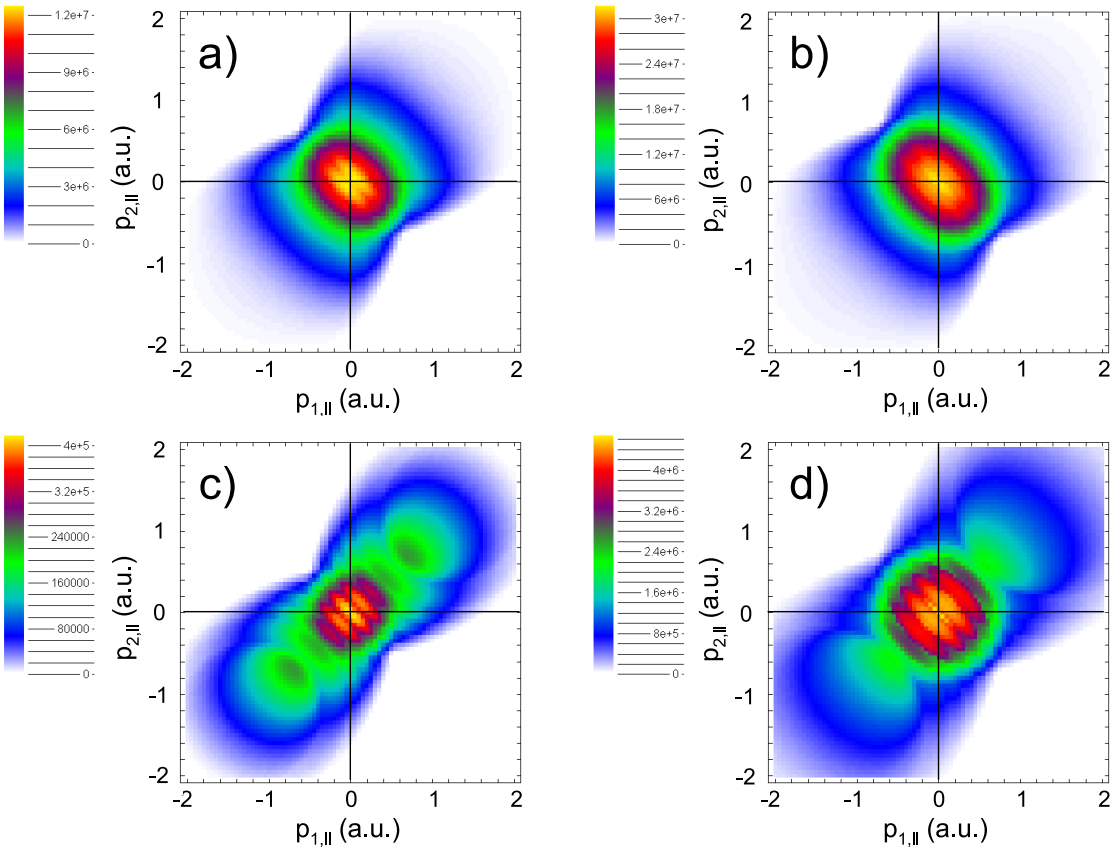

Fig. 5.8: Calculated e^--e^- momentum correlation for the model molecules: O_2 at 1.9×10^{14} W/cm^2(a) and at 2.2×10^{14} W/cm^2(b); N_2 at 1.8×10^{14} W/cm^2(c) and at 2.5×10^{14} W/cm^2(d).

of recollision, where an e^--e^- contact interaction potential in velocity gauge was assumed. Our calculations for atom have revealed the gauge dependence of the final electron momentum distribution, especially at higher light intensities. As can be seen in Fig. 5.8, for molecules $f(p_{e1,\parallel}, p_{e2,\parallel})$ stretches along the diagonal $p_{e1,\parallel} = -p_{e2,\parallel}$ in a similar way as for atoms.

At the lowest light intensities the agreement between the model and the experiment is lost (compare Fig. 5.7 (a,b) with Fig. 5.1 (a,b) respectively). In contrast to the experiment, the calculated electron sum-momentum distribution develops a double hump structure. This discrepancy has probably its origin in our classical approach. The classically accessible phase space for the recolliding electron where $E_{kin,max}(t) \geq I_p^+(t)$ gets very small around $p_{ei,\parallel} = 0$. A quantum mechanical calculation may improve the situation for low light intensities.

So far we have discussed momentum distributions that are averaged over the orientation of the internuclear axis. This corresponds to our experimental conditions. For a fixed molecular orientation our model calculation shows that the final electron momentum distribution changes strongly with the alignment of the molecule with respect to the polarization direction of the light wave. Fig. 5.9 (a,c) displays the electron-electron momentum correlation with the molecular axis $\vec{R}$ aligned parallel with respect to the polarization direction $\vec{E}$ of the light wave. The same distributions are shown in Fig. 5.9 (b,d) for molecules aligned perpendicular to $\vec{E}$. The upper panel shows the results for N_2 and the lower one for O_2. Obviously, for N_2 the momentum correlation averaged over all orientations (Fig. 5.5 (a)) is mainly determined by the events where $\vec{R} \perp \vec{E}$. The contribution of electrons emitted at $\vec{R} \parallel \vec{E}$ is orders of magnitude smaller. This is due to $\sin\theta$ being small in the orientation average integral in Eq. (5.6) for $\theta(\vec{R}, \vec{E})$ close to zero. The same is true for O_2 if $\vec{R} \parallel \vec{E}$. Additionally, for $\vec{R} \perp \vec{E}$, due to the antibonding symmetry of O_2, electron waves emitted from the two nuclear centers cancel each other on the observation axis along the electric field direction. This destructive interference results in a negligibly small contribution to the momentum correlation from $\vec{R} \perp \vec{E}$ in Fig. 5.9 (d). In this case intermediate angles $0 < \theta(\vec{R}, \vec{E}) < \pi/2$ determine the main contribution to the e^--e^- momentum distribution after averaging.

Fig. 5.10 shows the relative contribution of the photoelectron pairs at different $\theta(\vec{R}, \vec{E})$ to the full orientation-averaged e^--e^- momentum correlation $\frac{N(\theta)}{\int N(\theta) d\theta}$. The maximum contribution for the O_2 model molecule (left panel) is found at an angle of about 35 deg. For N_2 (right panel), the dependence on the molecular orientation changes from a minimum at 0 deg, i.e. along the laser field direction, to a maximum for the perpendicular orientation of the molecule with respect to the field axis. It is important to note that the molecular orientation dependence in our model is only taken into account in the form factor $|V_{\vec{p}_1,\vec{p}_2,\vec{k}}|^2$ in Eq. (4.7). The ionization rate $R(t)$ for a molecule is assumed to be the same as for an atom with the corresponding

ionization potential, i.e. independent of the molecular orientation in the laser field.

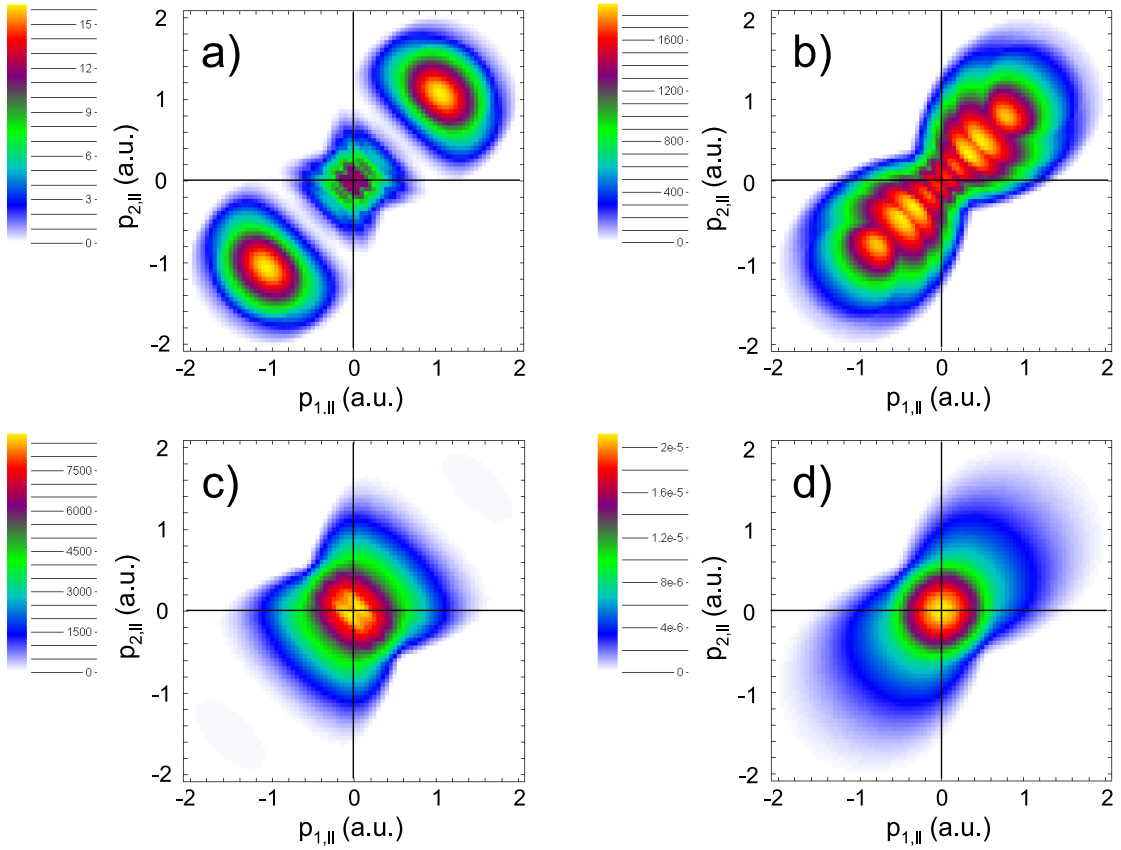

Fig. 5.9: Calculated e^--e^- momentum correlation similar to that in Fig. 5.5 but for the fixed alignment of the molecular axis with respect to the light beam polarization axis. $\vec{R} \parallel \vec{E}$ (right panel), $\vec{R} \perp \vec{E}$ (left panel). N_2 at 1.5×10^{14} W/cm^2(a,b); O_2 at 1.7×10^{14} W/cm^2(c,d).

Actually, several theoretical models indicate that the strong field single electron ionization rate of molecules depends on the molecular orientation with respect to the laser field [151, 153, 154, 155, 156]. Recently, it has been found experimentally that N_2 molecules aligned parallel to the ionizing electric field of the linearly polarized light wave get ionized four times more likely than molecules aligned perpendicular to the field [157]. As has been discussed above, ultra-short laser pulses $\leqslant$ 50 fs do not align molecules like N_2 and O_2. In this case, orientation effects cannot be observed directly in the experiment because of the isotropic distribution of molecular orientations. Nevertheless, it has been shown by DeWitt *et al.* within the so-called structure-based tunneling model [151], as well as in calculations by Tong *et al.* based

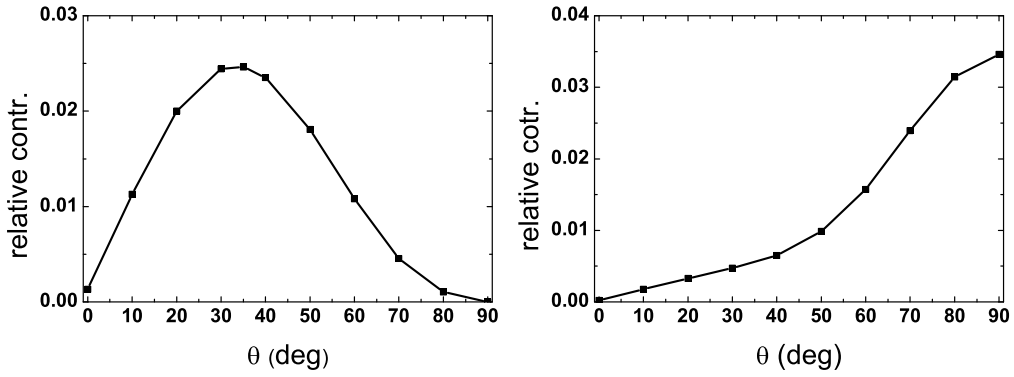

Fig. 5.10: Relative contribution to the e^--e^- momentum correlation after NSDI of the photoelectron pairs ejected at different molecular orientation with respect to the laser field direction $\theta(\vec{R}, \vec{E_0})$.

on molecular ADK theory [154], that molecular orientation has a significant effect on the tunneling ionization rate. Molecules with anisotropic electron distribution like O_2 have a small ionization probability if they are aligned along the laser field direction [154]. As a result, the molecular orientation effects contribute to the overall ionization rate averaged over randomly oriented molecules in an intense laser field. In particular, this may lead to a suppressed ionization rate of molecules with anisotropic electron distribution like O_2.

Summarizing, our NSDI calculations for the model molecules corresponding to N_2 and O_2 are able to reproduce the main features of the electron momentum distributions found experimentally. They also indicate that the e^--e^- momentum correlation is mainly determined during tunneling of the first electron for O_2 and during the inelastic recollision for N_2. The initial state symmetry of the molecular orbital is found to be responsible for the differences between N_2 and O_2 in the final state after NSDI. We have also shown the influence of the molecular orientation on the electron momentum correlation, which can not be resolved in our experiment.

5.6 Other theoretical models and their relevance in experiments

We have seen that the differences between N_2 and O_2 found in our experiment on double ionization by ultrashort high-intensity laser pulses can be successfully ex-

plained by an initial state symmetry effect. Molecules with bonding and antibonding symmetry of the initial state valence orbitals can give rise to entirely different electron momentum correlations in the final state after NSDI. The same symmetry effect has been found to be responsible for suppressed single ionization and the reduced yield of low-energy electrons in ATI spectra for O_2 with respect to Xe, which has the same ionization potential [144, 145]. However, destructive interference due to the antibonding symmetry of the electronic ground state is not the only mechanism which explains the suppressed single ionization of O_2.

An alternative explanation has been suggested by Guo in [158]. He introduced a so-called charge-screening correction to the tunneling theory, that allows one to describe correctly the observed suppressed yield of O_2^+ ions. This model assumes that the detailed electronic structure of the molecule plays the key role in strong field tunneling ionization. In particular, a molecule with the spatially symmetric two-electron wave function (a singlet state) is expected to behave in a strong laser field like a structureless atom with the same ionization potential. In contrast, if an electron is removed from a molecule with an antisymmetric two-electron wave function (a triplet state) via strong field tunneling ionization, the remaining one has no time to adjust its position and to minimize the energy. As a consequence, the ion core charge seen by the ionizing electron effectively increases and ionization becomes less probable than in a weak field. The ADK calculation for O_2, which has a triplet ground state, with the corrected I_p and with an effective charge well reproduces the experimentally observed suppressed single ionization. This effect does not appear for N_2, which has a closed shell electronic structure (singlet state), as well as for rare gas atoms where the outermost electrons are assumed to be uniformly distributed around the ion core [158].

A drawback of the charge-screening model as it is introduced in [158] is that the presence of the two nuclei in the molecule is ignored. The molecule is simply modeled by a single ion core and the valence electrons. The applicability of the model to realistic molecular systems is questionable, not to mention its extension to NSDI of molecules. So far only one *ab initio* 1D quantum-mechanical calculation has been performed for a model atom with a spatially symmetric (singlet state) and antisymmetric (triplet state) two-electron wave function [159]. The calculation has shown that the electronic structure (singlet or triplet) may influence the NSDI process.

A further theoretical approach has investigated the possible influence of vibrational motion on the single ionization rate of diatomic molecules [160]. The calculation predicts a reduced ionization rate for O_2 and H_2 molecules but the effect due to the vibrational motion seems to be too small to explain the experimental data. The relevance of the model for NSDI is even more doubtful since the typical vibrational period of the molecule is much longer than the optical cycle of 800 nm laser radiation which sets the scale for NSDI.

Recently, a simple classical analysis for NSDI of N_2 and O_2 by high-intensity short laser pulses [161] has been performed. In this calculation only the final stage of the ionization process is analyzed, i.e. the evolution of the two photoelectrons in combined Coulomb and external fields after a highly excited molecular complex has formed during electron rescattering. This analysis does not indicate any difference in the final e^--e^- momentum correlation for N_2 and O_2 with similar initial conditions. The result of this calculation strongly suggests that the difference between N_2 and O_2 observed in our experiment has its origin in an earlier stage of the ionization process.

Both mechanisms, the interference due to bonding or antibonding symmetry of the molecular orbital and the charge-screening correction, are quite general and thus should apply at least to every diatomic molecule. However, a recent experiment on single ionization of diatomic molecules in a strong laser field seems to indicate that neither the first nor the second mechanism alone is sufficient to quantitatively predict integral ion yields in single ionization of diatomics in general [162]. Besides N_2 and O_2, single ionization of S_2 and F_2 molecules has been investigated in this study. F_2 has a singlet electronic ground state and an ionization potential similar to N_2, but the symmetry of the ground state molecular valence orbital is antibonding (π_g) as for O_2. According to the interference mechanism, single ionization of F_2 is thus expected to be suppressed with respect to N_2 [145]. This, however, is not observed in the experiment [162]. The S_2 molecule has a triplet electronic ground state with antibonding symmetry of the active molecular valence orbital similar to O_2, but with significantly lower ionization potential $I_p = 9.26$ eV. The ionization suppression effect in S_2, which is expected to be less pronounced compared to O_2 due to a larger internuclear separation, is also not confirmed experimentally. On the other hand, also the charge-screening model with its prediction of suppressed ionization for F_2 fails in describing the experimental data.

Further experimental investigation of diatomics, including heteronuclear, has shown that molecules with singlet electron configuration exhibit more atomlike single ionization properties, while molecules with doublet and triplet electronic structure appear to have suppressed ionization relative to atoms with the same I_p [163].

Contrary, the most recent experimental data for Cl_2, a molecule with the closed-shell antibonding valence orbital and I_p similar to Xe, seem to confirm the hypothesis that suppressed single ionization in a strong laser field appears due to the antibonding symmetry effect of the molecular valence orbital [164]. This result may indicate that the absence of ionization suppression for F_2 could be an exception from the main tendency.

A tunneling ionization theory developed for molecules [154, 155] was able to reproduce several experimental results for the ratio of ionization signals of molecules with respect to the corresponding atoms with similar I_p. Based on the ADK model for tunneling ionization of atoms, this theory has been modified to account for

the symmetry differences in the initial-state wave function of a valence electron in the molecular orbital. The molecular tunneling ionization theory fails, however, to predict the observed single ionization ratio for F_2 :Ar [154].

Just recently, the quantum-mechanical strong-field S-matrix calculations performed for N_2 and O_2 in [144, 145] have been extended to other linear molecules [156] in order to study the effect of molecular orbital symmetry and molecular orientation on the photoelectron energy spectra and angular distributions as well as on the total ionization rates. For a molecule with π symmetry of its valence molecular orbital a minimum in the angular distribution after single electron ionization has been found at 0 deg and a maximum at about 40 deg with respect to the polarization direction. Such an angular distribution occurs if the molecule is aligned along the polarization axis but not for randomly oriented π-symmetric molecules and not for σ-symmetric molecules. These symmetry-induced effects predicted for angular distributions [156] are remarkable in light of recent experimental observations by Alnaser *at al.* [165]. In this experiment signatures of symmetry effects have been observed in angular distributions for the decay of excited electronic states of N_2^{2+} and O_2^{2+} produced in NSDI of N_2 and O_2 via rescattering. The observed angular distribution spectra exhibit a similar structure as the theoretically predicted one for the single electron ionization of N_2 and O_2 [155, 156]. This result suggests that the strongest symmetry-induced anisotropic angular effects appear at the first step of NSDI, i.e. when the outermost valence π or σ electron is removed via tunneling ionization[165].

Finally, a strong-field approximation calculation by Kjeldsen and Madsen [166], similar to that in [156], for the N_2 molecule should be mentioned. It has been performed in both, the length and velocity gauge. The results of this calculation for the photoelectron angular distribution as well as for the dependence of the single ionization rate on the molecular orientation are different for the two gauges. In the length gauge the ionization rate is maximum when the molecule is aligned along the laser field. In contrast, in the velocity gauge the maximum ionization rate is found at the perpendicular orientation of the molecule. Our model calculations have also been performed in velocity gauge. This may be the reason for the maximum at $\theta(\vec{R}, \vec{E}) = 90$ deg found for N_2 in the dependence on $\theta(\vec{R}, \vec{E})$ of the relative contribution of the photoelectron pairs to the e^--e^- momentum correlation averaged over molecular orientations (see Fig. 5.10).

Summarizing, in this chapter we have presented and discussed our results on NSDI of diatomic molecules. The main features found in our experiment can be understood within the framework of the rescattering model with instantaneous electron impact ionization of the singly charged molecular ion. The molecular structure decisively influences the final e^--e^- momentum correlation. The differences found

between N_2 and Ar momentum correlation spectra indicates that this influence is more pronounced in double ionization than in single ionization. The N_2 molecular structure strongly affects the inelastic recollision. On the other hand, the e^--e^- momentum correlation for O_2 is mainly determined in the first stage of the ionization process during the transition of the first electron to the ionization continuum. Our model calculation shows that the final electron correlation can be significantly different depending on the alignment of the molecule in the external field of the light wave. Averaging over randomly oriented molecular axes washes out much of the alignment-induced effects. The hypothesis that the symmetry of the initial state orbitals occupied by the active valence electrons plays a decisive role for NSDI of molecules seems to be confirmed by our experiment for N_2 and O_2. However, its relevance for other diatomic molecules is still not clear and has to be proven. Finally, for a correct description of molecular NSDI, which is limited in our semiclassical model, a full quantum-mechanical calculation is strongly desired.

6. Summary and outlook

In the present work, the ionization dynamics of the atoms Ar and Ne and the diatomic molecules N_2 and O_2 in an intense laser field has been investigated experimentally by means of correlated electron-ion momentum spectroscopy based on COLTRIMS. The main interest of this experimental study is non-sequential double ionization (NSDI), a nonlinear process which occurs in an electromagnetic field of highly intense laser radiation. The characteristic features of NSDI are most prominent for linearly polarized light. The typical light intensities for experimental observation of NSDI are of the order of 10^{14} W/cm^2.

In the present experiment 35 fs laser pulses with a central wave length of 800 nm and a repetition rate of 100 kHz have been used as a source of laser radiation.

To the present knowledge, the underlying ionization mechanism of NSDI is rescattering [62, 63]. In this mechanism an electron, ionized by the electric field of a light wave, is driven back by this field to its singly charged parent ion core, which is then ionized by the electron impact. In this way the two photoelectrons get correlated. In previous experiments spectra for the momentum correlation of the two photoelectrons after NSDI were observed for several atoms [16, 68, 72]. They revealed differences in NSDI of Ar and Ne. These atom specific features of NSDI are corroborated in this experiment. Whereas the results for Ne can be well understood within the electron impact ionization mechanism, the assumption of an additional ionization mechanism seems to be necessary to interpret the Ar data [68, 69, 167]. A possible scenario for this mechanism is instantaneous electron impact excitation of the singly charged ion with subsequent electric field ionization of the excited ion. The experiment shows that for Ar this second ionization mechanism becomes more significant with decreasing light intensity. In contrast, for Ne the instantaneous electron impact ionization prevails in a large range of light intensities, from the classical threshold I_p^+ to far above.

Within the classical rescattering scenario a threshold for instantaneous electron impact ionization is expected when the maximum kinetic energy of the recolliding electron $E_{kin,max}$ is comparable with the ionization potential of the singly charged ion I_p^+. It becomes energetically forbidden at $E_{kin,max} < I_p^+$. Nevertheless, in this experiment, structures characteristic of NSDI by instantaneous electron impact have been discovered for Ar at light intensities where $E_{kin,max} < I_p^+$, i.e. below threshold. It has been shown that sub-threshold e^- impact ionization may be understood in

the framework of the rescattering model by taking into account the shifting ionization threshold in the presence of the external electric field of the light wave at the instant of recollision. In the quasistatic approach this field instantaneously reduces the ionization potential of the singly charged ion, thus facilitating e^- impact ionization below threshold. A semiclassical calculation based on this improved rescattering model yields e^--e^- momentum correlations which are in good qualitative agreement with the experimental results including those at light intensities below NSDI threshold (see Chapter 4). A threshold lowering also explains why no abrupt decrease in the total ion yield ratio $[A^{++}]/[A^+]$ was found at $E_{kin,max} \sim I_p^+$ for various noble gases. Consequently, one can conclude that the electric field of the light wave essentially influences the electron scattering event in NSDI. The dependence on the light intensity of the electron sum-momentum distribution $f(p_\perp)$ in the plane perpendicular to the light polarization direction seems to confirm this conclusion also for $E_{kin,max} \gg I_p^+$.

The comparison of this experiment with several theoretical calculations shows that specific discrepancies exist. For the time being, the most successful model calculations yielding results qualitatively similar to the experiment are the semiclassical and quantum-mechanical calculations applying the three-body contact interaction [87, 85, 90]. Also the most complete semiclassical trajectory calculation with the full three-body Coulomb interaction [99, 100] is able to reproduce the experimental findings. The quantitative disagreement with experiment of the available theoretical results is not surprising in view of the approximations made.

Another interesting problem addressed in this thesis is non-sequential double ionization of molecules. At present it is not sufficiently explored experimentally as well as theoretically. Previous experiments revealed footprints of NSDI for several molecules in the dependence on light intensity of the total doubly charged ion yield [58, 59, 136, 137, 138]. However, the ionization mechanism could not be identified completely. The main goals of this experiment have been to identify the molecular NSDI mechanism and to investigate the influence of molecule specific effects on the ionization process, and thus on the final electron momentum correlation. Homonuclear diatomics like N_2 and O_2 are good candidates for this investigation. Their relatively simple structure with two identical nuclear centers allows one to model them theoretically more accurate and to understand the influence of the molecular structure in comparison with atoms.

The e^--e^- momentum correlation found in the experiment differs significantly for N_2 and O_2. The distribution $f(p_{e1,\parallel}, p_{e2,\parallel})$ for N_2 exhibits structures characteristic of instantaneous e^- impact ionization while this is not the case for O_2. Both, N_2 and O_2 show new features in the final electron momentum correlation which are not observed for atoms. The comparison of N_2 molecule with the Ar atom, which has a similar ionization potential I_p^+, at the same light intensity reveals most obviously the effect of two nuclei (see Chapter 5).

A semiclassical analysis based on the rescattering model has been applied to the N_2 and O_2 molecules in order to test the applicability of the electron impact ionization mechanism. The model calculation includes the symmetry of the initial molecular state occupied by the active valence electrons. The results of this calculation qualitatively reproduce the main features found in the experiment. Thus, two important conclusions can be drawn. First, instantaneous electron impact ionization seems to be the general mechanism for NSDI of atoms and molecules. Second, the molecular structure decisively influences the final e^--e^- momentum correlation after NSDI. It has been found that the bonding symmetry of the initial state of the molecule strongly modifies the inelastic electron recollision. In contrast, the antibonding symmetry mainly affects the first stage of NSDI during the electron transition to the ionization continuum via tunneling.

Although this experiment on N_2 and O_2 indicates that the symmetry of the initial state orbital occupied by the valence electron plays a decisive role for NSDI, further experimental investigations are necessary to generalize this statement for all diatomic molecules.

From the theoretical point of view, complete NSDI quantum-mechanical calculations which correctly describe the interaction of the recolliding electron with the bound e^- and with the ion core are strongly desirable for atoms as well as for diatomic molecules. Also instantaneous electron excitation followed by electric field ionization has to be taken into account for a correct description of NSDI of Ar and He.

Appendix A

C++ code for the data analysis

The analysis of the measured data has been performed by means of the "CoboldPC" software (ReontDek Handles GmbH). We have modified the main C++ code and adjusted it for our experiment. It allows to generate a dynamic link library (dll) file which, being recalled from the "CoboldPC", determines the data analysis.

```
//////////////////////////////////////////////////////////////////////
//USER DEFINED ANALYSIS PART CALLED FROM COBOLD MAIN PROGRAM
//////////////////////////////////////////////////////////////////////

//COORDINATES//
double x0e, y0e;
double Ua, L_accel, L_free, T0e, Tc, e, Wc, L_accel_i;
double /*Xi0, Yi0, */Ti1, Ti2;
int Start_Sort,Stop_Sort;

//FUNCTIONS FOR THE ANALYSIS//

//FUNCTION TO EXTRACT DATA FROM LeCroy TDC//
int merge(int high_byte,int low_byte)
{
return ((high_byte & 0x000000FF)*256 + (low_byte & 0x000000FF));
}

//FUNCTION TO EXTRACT INFORMATION OF THE TDC CHANNEL//
int extr_channel(int in)
{
return ((in & 0x00007C00)/0x00000400); //extract channel
}

//TEST WHETHER THE RAW DATA MAKES SENSE//
int bit(int x)
```

```
{
return ((x & 0x00000100)/0x00000100);
}

double position(double t1,double t2)
{
return (t2-t1);
}

double time_test(double time_x1, double time_x2, double time_of_flight)
{
return (time_x1+time_x2-2*time_of_flight);
}
//EXTRACT THE RAW DATA FROM THE PHILLIPS TDC//
int merge_ion(int data)
{
return (data & 0x00000FFF);
}

//EXTRACT INFORMATION OF THE TDC CHANNEL
int extr_channel_ion(int in)
{
return ((in & 0x0000F000)/0x00001000);
}

double time_test_ion(double time_x1, double time_x2)
{
return (time_x1+time_x2);
}

double F (double p, double E, double la, double lf, double t0, double t)
{
return (p/E + sqrt(p*p + 2*E*la)/E + lf/sqrt(p*p + 2*E*la) + t0 - t);
}

double DF (double p, double E, double la, double lf)
{
return (1/E + (p/sqrt(p*p + 2*E*la))*(1/E - lf/(p*p + 2*E*la)));
}

double P_transver (double w, double r, double t)
```

```
{
return (w*r/fabs(2*sin(w*t/2)));
}
////////////////////////////////////////////////////////////////////////
CDAN_API LPCTSTR AnalysisGetInformationString()
{
return LPCTSTR("DAN for CoboldPC 2002");
}
////////////////////////////////////////////////////////////////////////

//PARAMETERS FOR THE ANALYSIS//

CDAN_API BOOL AnalysisInitialize(CDoubleArray *pEventData,
CDoubleArray *pParameters, CDoubleArray *pWeighParameter)
{
x0e = (pParameters->GetAt(200));
y0e= (pParameters->GetAt(201));
Ua = (pParameters->GetAt(202));
L_accel = (pParameters->GetAt(203))/0.529E-10;
L_free = (pParameters->GetAt(204))/0.529E-10;
T0e = 2.07E+7*(pParameters->GetAt(205));
Tc = 2.07E+7*(pParameters->GetAt(206));
e = (pParameters->GetAt(207));
Wc = 6.283185/(2.07E+7*(pParameters->GetAt(208)));
Ti1 = (pParameters->GetAt(209));
Ti2 = (pParameters->GetAt(210));
L_accel_i = (pParameters->GetAt(211))/0.529E-10;
//Xi0 = (pParameters->GetAt(212));
//Yi0 = (pParameters->GetAt(213));
// First event to be taken into account//
Start_Sort = (int) (pParameters->GetAt(212) + 0.1);
Stop_Sort  = (int) (pParameters->GetAt(213) + 0.1);
srand( (unsigned)time( NULL ) );

return TRUE;
}

//COORDINATES USED IN THE ANALYSIS//
CDAN_API void AnalysisProcessEvent(CDoubleArray *pEventData,
CDoubleArray *pParameters, CDoubleArray *pWeighParameter)
{
```

```
int i, n, m, channel = 0;
int Event_Counter;
double hit_1[32], hit[32], pos_e[2], re, pzi1, pzi2;
double x = 0;
double Xi, Yi/*, TOFi,Ri, pxyi*/;
double pe, pe0, E_accel, T, pxye, R, T1, Q, Ekin, p_calc;
bool good_ev;
double trans = 3.7996e5;

//EVENT COUNTER//
Event_Counter = (int) (pParameters->GetAt(214) + 1.1);
pParameters->SetAt(214, Event_Counter);

for (n = 0; n < 32; n++)
{
hit_1[n] = (double) (-1000.0);
hit[n] = (double) (-1000.0);
}

for (n = 0; n < 43; n++)
{
pEventData->SetAt(30 + n,(double)(-1000.0));
}

//EXTRACTION OF TIME SIGNALS FROM THE LeCroy TDC (ELECTRONS AND IONS)//
for (n = 0; n < 6; n++)
{
if (bit((int)(pEventData->GetAt(2*n+1)+0.1)) == 1)
{
channel = extr_channel((int)(pEventData->GetAt(2*n+2)+0.1));

if ((0 <= channel) && (channel < 5))
{
hit_1[channel] = (double)merge((int)(pEventData->GetAt(2*n+1)+0.1),
  (int)(pEventData->GetAt(2*n+2)+0.1));

//set a real value
pEventData->SetAt(30 + channel, hit_1[channel]);
}
if (channel == 10)
{
```

```
hit_1[5] = (double)merge((int)(pEventData->GetAt(2*n+1)+0.1),
   (int)(pEventData->GetAt(2*n+2)+0.1));
//set a real value
pEventData->SetAt(35, hit_1[5]);
}
}

else break;
}
for (n = 7; n < 12; n++)
{
if (bit((int)(pEventData->GetAt(2*n)+0.1)) == 1)
{
channel = extr_channel((int)(pEventData->GetAt(2*n+1)+0.1));

if ((0 <= channel) && (channel < 5))
{
hit_1[channel+6] = (double)merge((int)(pEventData->GetAt(2*n)+0.1),
    (int)(pEventData->GetAt(2*n+1)+0.1));

//set a real value
pEventData->SetAt(36 + channel , hit_1[channel+6]);
}
}

else break;
}

//EXTRACTION OF TIME SIGNALS FROM THE Phillips TDC (IONS)//
for (n = 24; n < 28; n++)
{
channel = extr_channel_ion((int)(pEventData->GetAt(n)+0.1));
if ((channel >= 0) && (channel <= 3))
{
hit[channel] = (double)merge_ion((int)(pEventData->GetAt(n)+0.1));

//set a real value
if (hit[channel] < 4095)
pEventData->SetAt(41+channel, hit[channel]);
}
}
```

```
// TEST WHETHER ALL DELAY-LINE SIGNALS ARE PRESENT//
//presence of laser pulse and time-of-flight is garanteed by hardware//
m = 0;
for (channel = 1; channel < 5; channel++)
{
if (0.0 < hit_1[channel]) m = m+1;
}
for (channel = 7; channel < 11; channel++)
{
if (0.0 < hit_1[channel]) m = m+1;
}
pEventData->SetAt(45, (double) (m));
// all signals are present!
if ((Event_Counter > Start_Sort) && (Event_Counter < Stop_Sort))
{
if (m == 8)
{
for (channel = 0; channel < 2; channel++)
{
// position X,Y of e
pos_e[channel] = position(hit_1[2*channel+1], hit_1[2*channel+2]);

pEventData->SetAt(46+channel,position(hit_1[2*channel+1],
   hit_1[2*channel+2]));
// T2+T1-2*Tf of e
pEventData->SetAt(48+channel,time_test(hit_1[2*channel+1],
    hit_1[2*channel+2], hit_1[0]));
// position X,Y of i
pEventData->SetAt(50+channel,position(hit_1[2*channel+8],
   hit_1[2*channel+7]));

// position X,Y of i
Xi = ((rand() % 100)*0.01 - 0.5) + position(hit_1[8],hit_1[7]);
Yi = ((rand() % 100)*0.01 - 0.5) + position(hit_1[10],hit_1[9]);
// T2+T1-2*Tf of i
pEventData->SetAt(52+channel,time_test(hit_1[2*channel+8],
    hit_1[2*channel+7], hit_1[6]));
}
}
```

```
//CALCULATION OF THE ELECTRON TIME-OF-FLIGHT//
if ((hit_1[5] > 0.0) && (hit_1[0] > 0.0))
pEventData->SetAt(54,hit_1[5] - hit_1[0]);

if ((hit_1[5] > 0.0) && (hit_1[6] > 0.0) && (hit_1[0] > 0.0))
{
// ELECTRON CYCLOTRON MOTION//
re = sqrt((pos_e[0]+((rand() % 100)*0.01 - 0.5)-x0e)*(pos_e[0]+
((rand() % 100)*0.01 - 0.5)-x0e) +
  (pos_e[1]+((rand() % 100)*0.01 - 0.5)-y0e)*(pos_e[1]+
((rand() % 100)*0.01 - 0.5)-y0e));
pEventData->SetAt(55,re);

//CALCULATION OF THE ION TIME-OF-FLIGHT//
pEventData->SetAt(56,hit_1[6] + hit_1[5] - hit_1[0]);// TOF of i
}

n = 0;
if (0.0 < hit_1[0]) n = n+1;
if (0.0 < hit_1[6]) n = n+1;
pEventData->SetAt(57, (double) (n));

//CALCULATION OF THE ION POSITION FROM THE Phillips TDC//
n = 0;
for (channel = 0; channel < 4; channel++)
{
if (hit[channel] < 4095) n = n+1;
}

if (n == 4)
{
for (channel = 0; channel < 2; channel++)
{

pEventData->SetAt(58+channel,position(hit[2*channel+1],
   hit[2*channel]));
// T2+T1-2*Tf of i//
pEventData->SetAt(60+channel,time_test_ion(hit[2*channel],
  hit[2*channel+1]));
}
}
```

```
good_ev = true;
for (i = 0; i < 6; i++)
{
if (hit_1[i] <= 0.0) good_ev = false;
}

//MOMENTUM COMPONMENT Pz FOR THE ELECTRON//
E_accel = Ua/(54.4*L_accel);
pe = Tc*E_accel;
T = 2.07E+7*(hit_1[5] - hit_1[0] + ((rand() % 100)*0.01 - 0.5));
T1 = T - T0e;
do
{
pe0 = pe;
pe = pe0 - F(pe0, E_accel, L_accel, L_free, T0e, T)/DF(pe0, E_accel,
L_accel, L_free);
}
while (fabs(pe - pe0) >= e);

if ((hit_1[5] > 0.0) && (hit_1[0] > 0.0))
{
pEventData->SetAt(62, (double) (pe));

//MOMENTUM COMPONMENT Pxy FOR THE ELECTRON//
R = 5.4E+6*re;
pxye = P_transver (Wc, R, T1);
pEventData->SetAt(63, (double)(pxye));

//ELECTRON EMITION ANGLE theta//
Q = acos(pe/sqrt(pe*pe + pxye*pxye));
pEventData->SetAt(64, (double)(Q));

//KINETIC ENERGY OF THE ELECTRON//
Ekin = 0.5*(pe*pe + pxye*pxye)*0.77;
pEventData->SetAt(65, (double)(Ekin));
}

//MOMENTUM COMPONMENT Pz FOR i+, i++//
if ((hit_1[5] > 0.0) && (hit_1[6] > 0.0) && (hit_1[0] > 0.0))
{
```

```
//i+
pzi1 = (-hit_1[6] - hit_1[5] + hit_1[0] + Ti1 +
((rand() % 100)*0.01 - 0.5)) * trans * Ua / L_accel_i;
pEventData->SetAt(66, (double) (pzi1));

//i++
pzi2 = (-hit_1[6] - hit_1[5] + hit_1[0] + Ti2 +
((rand() % 100)*0.01 - 0.5)) * 2.0 * trans * Ua / L_accel_i;
pEventData->SetAt(67, (double) (pzi2));

//MOMENTUM Pz FOR THE SECOND ELECTRON//
p_calc = -pzi2 - pe;
pEventData->SetAt(68, (double) (-pzi2 - pe));

//MOMENTUM CONSERVATION FOR SINGLE ELECTRON IONIZATION (SHOULD BE ZERO)//
pEventData->SetAt(69, (double) (-pzi1 - pe));

//MOMENTUM DIFFERENCE FOR DOUBLE IONIZATION//
pEventData->SetAt(70, (double) (-pzi2 - 2*pe));


//CONDITRION THAT THE DETECTED ELECTRON IS COMING AT THE DETECTOR FIRST//
if (pe <= p_calc)
{
pEventData->SetAt(71, (double)(Q));

pEventData->SetAt(72, (double)(Ekin));
}

}
}
  return;
}

CDAN_API void AnalysisFinalize(CDoubleArray *pEventData,
CDoubleArray *pParameters, CDoubleArray *pWeighParameter)
{
}
```

Appendix B

C++ code for NSDI model calculation

This program has been written in the course of the present work and used for the NSDI model calculations for Ar, Ne, N_2, and O_2.

```
//Program for a corr-Spectrum
//written by E. Eremina

#include <stdio.h>
#include <stdlib.h>
#include <math.h>
#include <float.h>
#include <iostream>
#include <conio.h>
#include <fstream>
#include <string>
#include <time.h>

using namespace std;
double Ip1, Ip2, Up;
double w;//laser frequency
double F, F0;//laser field strengt

////////////functions/////////////////////////////////////////////////////
//momentum function
double mom (double U, double x0,double x)
{
return (2*sqrt(U)*(cos(x)-cos(x0)));
}

/*position function
double pos (double U, double y0,double y)
{
```

```
return (2*sqrt(Up)/w*((sin(y)-sin(y0))-cos(y0)*(y-y0)));
}
*/
double Fu (double y0, double y)
{
return ((sin(y)-sin(y0))-cos(y0)*(y-y0));
}

double delta (double p1, double p2, double I, double Er)
{
return (Er - I - p1*p1/2 - p2*p2/2);
}

double Ip (double I, double s, double F0)
{
return (I - 2*sqrt(2*fabs(F0*sin(s))));
}
////////////////////////////////////////////////////////////////////////

void main()
{
string dataname_new;

double Ip1, Ip2, Up;
double w;//laser frequency
double F, F0;//laser field strengt
int l, i;
long double Pi = 3.1415926535;
double v;
double b=1.5;
double a[3][12100];
double wt,wt0, wt1, wt_r;
double rate;//ADK-ionization rate
double Ilas, e;
double Eret, Exess;
double p1, p2;
double Nu;

cout << "Matrix: " << endl;
////////////////////////////////////////////////////////////////////////
for (l = 0; l < 12100; l++)
```

```
{
 a[0][l] = (abs(l/110)-50)*0.1;
 if (l%110 == 0)
 {
i=0;
do
{
a[1][l+i] = (i-50)*0.1;
i++;
}
while (i<110);
 }
a[2][l] = 0;
}
////////////////////////////////////////////////////////////////////////
//laser intensity in units of W/cm^2

cout << "Laser intensity in W/cm^2: " << endl;
cin >> Ilas;

F0 = sqrt(Ilas/351E14);

w = 5.7;//in a.u. for lambda = 800nm

//ionization potential of Ar+ and Ar2+ in a.u.
Ip1 = 15.76/27.21;
Ip2 = 27.63/27.21;

v = 2*Ip1;

e = 1E-4;//accuracy

//corresponding ponderomotive potential in a.u.
Up = 5.9712*(Ilas/1E14)/27.21;
////////////////////////////////////////////////////////////////////////
wt0 = Pi/2;
do
{
wt = wt0 + Pi/40;
F = F0*sin(wt0);
rate = (4/F)*exp(-(2*sqrt(8*Ip1*Ip1*Ip1))/(3*F));
```

```
// cout << "wt0 = " << wt0 << " Rate = " << rate << endl;

// condition for the return is
// 2*sqrt(Up)/w*((sin(y)-sin(y0))-cos(y0)*(y-y0)) = 0
//=> Fu(wt0,wt_r)->0

wt_r = wt0+0.1;
do
{
wt1 = wt_r + 0.00001*Pi;
wt_r = wt1;
}
while (fabs(Fu(wt0,wt_r/*-0.00001*Pi*/)) >= e);

Eret = 0.5*mom(Up,wt0,wt_r)*mom(Up,wt0,wt_r);

cout << "wt0 = " << wt0 << " wt_r = " << wt_r << " Eret = "
<< Eret << " Ip= " << Ip(Ip2,wt_r,F0) << endl;
////////////////////////////////////////////////////////////////////////
// drift after rescattering ionization if (Pi/2 <= wt0 <= Pi)
for (l = 0; l < 12100; l++)
{
p1 = a[0][l] - 2*sqrt(Up)*cos(wt_r);
p2 = a[1][l] - 2*sqrt(Up)*cos(wt_r);

if (delta(p1,p2,Ip(Ip2,wt_r,F0),Eret)>0)
{
Exess = delta(p1,p2,Ip(Ip2,wt_r,F0),Eret);
Nu = a[2][l]+ rate*Exess;// rate*Exess;
// cout << "wt0 = " << wt0 << " wt_r = " << wt_r
 << " Ip = " << Ip2 << endl;
a[2][l] = Nu;
}

}
// symmetry part due to drift after rescattering ionization
//if (3*Pi/2 <= wt0 <= 2*Pi)

for (l = 0; l < 12100; l++)
{
```

```
p1 = a[0][l] + 2*sqrt(Up)*cos(wt_r);
p2 = a[1][l] + 2*sqrt(Up)*cos(wt_r);

if (delta(p1,p2,Ip(Ip2,(wt_r+Pi),F0),Eret)>0)
{
Exess = delta(p1,p2,Ip(Ip2,(wt_r+Pi),F0),Eret);
Nu = a[2][l]+ rate*Exess;// rate*Exess;
a[2][l] = Nu;
}
}
wt0 = wt;
}
while (wt0 < (Pi-0.001*Pi));//
////////////////////////////////////////////////////////////////////////
cout << "Name of the new file: " << endl;
cin >> dataname_new;

ofstream newdata(dataname_new.c_str(),ios::out);
if (!newdata)
{
cerr << "could not be written!" << endl;
exit(1);
}

newdata.setf(ios_base::scientific);

for (l = 0; l < 12100; l++)
{
newdata << a[0][l] << "\t" << a[1][l] << "\t" << a[2][l] << "\n";
}

cout << "Ready :)" << endl;
////////////////////////////////////////////////////////////////////////
getch();
return;
}
```

Bibliography

[1] G. Petite, P. Agostini, and H.G. Muller. *J. Phys. B*, 21:4097, 1988.

[2] E.R. Peterson and P.H. Bucksbaum. Above-threshold double-ionization spectroscopy of argon. *Phys. Rev. A*, 64:053405, 2001.

[3] D. Strickland and G. Mourou. *Opt. Commun.*, 56:219, 1985.

[4] G.S.Voronov and N.B. Delone. *JETP Letters*, 1:66, 1965.

[5] M. Göppert-Mayer. *Ann. der Physik*, 9:273, 1931.

[6] P. Agostini, F. Fabre, G. Mainfray, G. Petite, and N.K. Rahman. *Phys. Rev. Lett.*, 42:1127, 1979.

[7] F. Krausz. *Phys. World*, 14:41, 2001.

[8] P. Saliéres, A. l'Huillier, P. Antoin, and M. Lewenstein. *Adv. At. Mol. Opt. Phys.*, 41:83, 1999.

[9] A.M. Perelomov, V.S. Popov, and M.V. Terent'ev. *Sov. Phys. JETP*, 23:924, 1966.

[10] M.V. Ammosov, N.B. Delone, and V.P. Krainov. *Sov. Phys. JETP*, 64:1191, 1986.

[11] A. L'Huillier, L.A. Lompre, G. Mainfray, and C. Manus. *Phys. Rev. A*, 27:2503, 1983.

[12] D.N. Fittinghoff, P.R. Bolton, B. Chang, and K.C. Kulander. *Phys. Rev. Lett.*, 69:2642, 1992.

[13] S. Larochelle, A. Talebpour, and S. L. Chin. *J. Phys. B*, 31:1201, 1998.

[14] B. Walker, B. Sheehy, L. F. DiMauro, P. Agostini, K. J. Schafer, and K. C. Kulander. *Phys. Rev. Lett.*, 73:1227, 1994.

[15] J. Ullrich, R. Moshammer, R. Dörner, O. Jagutzki, V. Mergel, H. Schmidt-Böcking, and L. Spielberger. Recoil-ion momentum spectroscopy. *J. Phys. B*, 30:2917, 1997.

[16] Th. Weber, M. Weckenbrock, A. Staudte, L. Spielberger, O. Jagutzki, V. Mergel, F. Afaneh, G. Urbasch, M. Vollmer, H. Giessen, and R. Dörner. Recoil-ion momentum distributions for single and double ionization of helium in strong laser fields. *Phys. Rev. Lett.*, 84:443, 2000.

[17] R. Moshammer, B. Feuerstein, W. Schmitt, A. Dorn, C. D. Schröter, J. Ullrich, H. Rottke, C. Trump, M. Wittmann, G. Korn, K. Hoffmann, and W. Sandner. Momentum distributions of ne_{n+} ions created by an intense ultrashort laser pulse. *Phys. Rev. Lett.*, 84:447, 2000.

[18] B. Witzel, N.A. Papadogiannis, and D. Charalambidis. Charge-state resolved above threshold ionization. *Phys. Rev. Lett.*, 85:2268, 2000.

[19] R. Lafon, J.L. Chaloupka, B. Sheehy, P.M. Paul, P. Agostini, K.C. Kulander, and L.F. DiMauro. Electron energy spectra from intense laser double ionization of helium. *Phys. Rev. Lett.*, 86:2762, 2001.

[20] L.F. DiMauro and P. Agostini. *Adv. At. Mol. Opt. Phys.*, 35:79, 1995.

[21] M. Protopapas, C.H. Keitel, and P.L. Knight. Atomic physics with super-high intensity lasers. *Rep. Prog. Phys.*, 60:389, 1997.

[22] C.J. Joachain, M. Dörr, and N. Kylstra. *Adv. At. Mol. Opt. Phys.*, 42:225, 2000.

[23] R. Dörner, Th. Weber, M. Weckenbrock, A. Staudte, M. Hattass, H. Schmidt-Böcking, R. Moshammer, and J. Ullrich. *Adv. At. Mol. Opt. Phys.*, 48:1, 2002.

[24] J.L. Hall, E.J. Robinson, and L.M. Branscomb. *Phys. Rev. Lett.*, 14:1013, 1965.

[25] F. Fabre, G. Petite, P. Agostini, and M. Clement. *J. Phys. B*, 15:1353, 1982.

[26] G. Petite, F. Fabre, P. Agostini, M. Crance, and M. Aymar. *Phys. Rev. A*, 29:2677, 1984.

[27] L.A. Lompre, G. Mainfray, C. Manus, and J. Thebault. *Phys. Rev. A*, 15:1604, 1977.

[28] L.A. Lompre, A. L'Huillier, G. Mainfray, and C. Manus. *J. Opt. Soc. Am. B*, 2:1906, 1985.

[29] K. Burnett, V.C. Reed, and P.L. Knight. *J. Phys. B*, 26:561, 1993.

[30] P. Kruit, J. Kimman, H.G. Muller, and M.J. Van der Wiel. *Phys. Rev. A*, 28:248, 1983.

[31] R.R. Freeman, P.H. Bucksbaum, H. Milchberg, S. Darack, D. Schumacher, and M.E. Geusic. *Phys. Rev. Lett.*, 59:1092, 1987.

[32] P. Hansch, M.A. Walker, and L.D. Woerkom. *Phys. Rev. A*, 55:R2535, 1997.

[33] Y. Gontier and M. Trahin. *J. Phys. B*, 13:4383, 1980.

[34] P.H. Bucksbaum, R.R. Freeman, M. Bashkansky, and T.J. McIlrath. *J. Opt.Soc. Am. B*, 4:760, 1980.

[35] P. Agostini, A. Antonetti, P. Breger, M. Crance, A. Migus, H.G. Muller, and G. Petite. *J. Phys. B*, 22:1971, 1989.

[36] P. Agostini, P. Breger, A. L'Huillier, H.G. Muller, G. Petite, A. Antonetti, and A. Migus. *Phys. Rev. Lett.*, 63:2208, 1989.

[37] H. Rottke, B. Wolff, X. Brickwedde, D. Feldmann, and K.H. Welge. *Phys. Rev. Lett.*, 64:404, 1990.

[38] L.V. Keldysh. *Sov. Phys. JETP*, 20:1307, 1965.

[39] A.M. Perelomov, V.S. Popov, and M.V. Terent'ev. *Sov. Phys. JETP*, 24:207, 1967.

[40] V.S. Popov, V.P. Kuznetsov, and A.M. Perelomov. *Sov. Phys. JETP*, 26:222, 1968.

[41] F.H.M. Faisal. *J. Phys. B*, 6:L89, 1973.

[42] H.R. Reiss. *Phys. Rev. A*, 22:1786, 1980.

[43] N.B. Delone and V.P. Krainov. *Multiphoton Processes in Atoms.* Springer Series on Atoms and Plasmas, 1993.

[44] S. Augst, D.D. Meyerhofer, D. Strickland, and S.L. Chin. *J. Opt. Soc. Am. B*, 8:858, 1991.

[45] G. Gibson, T.S. Luk, and C.K. Rhodes. *Phys. Rev. A*, 41:5049, 1990.

[46] F.A. Ilkov, J.E. Decker, and S.L. Chin. *J. Phys. B*, 25:4005, 1992.

[47] G.E. Bayfield and P.M. Koch. *Phys. Rev. Lett.*, 33:258, 1974.

[48] T.F. Gallagher. *Phys. Rev. Lett.*, 61:2304, 1988.

[49] I. Aleksakhin, N. Delone, I. Zapesochnyi, and V. Suran. *Sov. Phys. JETP*, 49:447, 1979.

[50] A. L'Huillier, L.A. Lompre, G. Mainfray, and C. Manus. *Phys. Rev. Lett.*, 48:1814, 1982.

[51] A. Szöke, K.C. Kulander, and J.N. Bardsley. *J. Phys. B*, 24:3165, 1991.

[52] J.L. Krause, K.J. Schafer, and K.C. Kulander. *Phys. Rev. Lett.*, 68:3535, 1992.

[53] B. Walker, E. Mevel, B. Yang, P. Breger, J.P. Chambaret, A. Antonetti, L.F. DiMauro, and P. Agostini. *Phys. Rev. A*, 48:R894, 1993.

[54] D.N. Fittinghoff, P.R. Bolton, B. Chang, and K.C. Kulander. *Phys. Rev. A*, 49:2174, 1994.

[55] S. Augst, D.D. Meyerhofer, D. Strickland, and S.L. Chin. *Phys. Rev. A*, 52:R917, 1995.

[56] A. Talebpour, S. Larochelle, and S. L. Chin. *J. Phys. B*, 30:L245, 1997.

[57] S. Larochelle, A. Talebpour, and S. L. Chin. *J. Phys. B*, 30:L245, 1997.

[58] C. Cornaggia and Ph. Hering. *J. Phys. B*, 31:L503, 1998.

[59] C. Guo, M. Li, J. P. Nibarger, and G. N. Gibson. *Phys. Rev. A*, 58:R4271, 1998.

[60] V. Schmidt. *Electron Spectrometry of Atoms using Synchrotron Radiation*. Cambridge University Press, 1997.

[61] M.Yu. Kuchiev. *Sov. Phys. JETP Lett.*, 45:404, 1987.

[62] K.J. Schafer, B. Yang, L.F. DiMauro, and K.C. Kulander. *Phys. Rev. Lett.*, 70:1599, 1993.

[63] P.B. Corkum. *Phys. Rev. Lett.*, 71:1994, 1993.

[64] U. Eichmann, M. Dörr, H. Maeda, W. Becker, and W.Sandner. *Phys. Rev. Lett.*, 84:3550, 2000.

[65] P. Dietrich, N.H. Burnett, M. Ivanov, and P. Corkum. *Phys. Rev. A*, 50:R3585, 1994.

[66] G.G. Paulus, W. Nicklich, H. Xu, P. Lambropoulos, and H. Walther. *Phys. Rev. Lett.*, 72:2851, 1994.

[67] B. Sheehy, R. Lafon, M. Widmer, B. Walker, L.F. DiMauro, P. Agostini, and K.C. Kulander. *Phys. Rev. A*, 58:3942, 1998.

[68] Th. Weber, H. Giessen, M. Weckenbrock, G. Urbasch, A. Staudte, L. Spielberger, O. Jagutzki, V. Mergel, M. Vollmer, and R. Dörner. Correlated electron emission in multiphoton double ionization. *Nature*, 405:658, 2000.

[69] B. Feuerstein, R. Moshammer, D. Fischer, A. Dorn, C. D. Schröter, J. Deipenwisch, J. R. Crespo López-Urrutia, C. Höhr, P. Neumayer, J. Ullrich, H. Rottke, C. Trump, M. Wittmann, G. Korn, and W. Sandner. Separation of recollision mechanisms in nonsequential strong field double ionization of ar: The role of excitation tunneling. *Phys. Rev. Lett.*, 87:043003, 2001.

[70] M. Weckenbrock, M. Hattas, A. Czasch, O. Jagutzki, L. Schmidt, T. Weber, H. Roskos, T. Löffler, M. Thomson, and R. Dörner. *J. Phys. B*, 34:L449, 2001.

[71] R. Moshammer, B. Feuerstein, J. Crespo López-Urrutia, J. Deipenwisch, A. Dorn, D. Fischer, C. Höhr, P. Neumayer, C. D. Schröter, J. Ullrich, H. Rottke, C. Trump, M. Wittmann, G. Korn, and W. Sandner. Correlated two-electron dynamics in strong-field double ionization. *Phys. Rev. A*, 65:035401, 2002.

[72] R. Moshammer, J. Ullrich, B. Feuerstein, D. Fischer, A. Dorn, C.D. Schröter, J.R. Crespo López-Urrutia, C. Höhr, H. Rottke, C. Trump, M. Wittmann, G. Korn, K. Hoffmann, and W. Sandner. Strongly directed electron emission in non-sequential double ionization of ne by intense laser pulses. *J. Phys. B*, 36:L113, 2003.

[73] J.L. Chaloupka, J. Rudati, R. Lafon, P. Agostini, K.C. Kulander, and L.F. DiMauro. Observation of a transition in the dynamics of strong-field double ionization. *Phys. Rev. Lett.*, 90:033002, 2003.

[74] J.S. Parker, K.T. Taylor, Ch.W. Clark, and S. Blodgett-Ford. *J. Phys. B*, 29:L33, 1996.

[75] E.S. Smyth, J.S. Parker, and K.T. Taylor. *Comp. Phys. Comm.*, 114:1, 1998.

[76] D.D. Dundas, K.T. Taylor, J.S. Parker, and E.S. Smyth. *J. Phys. B*, 32:L231, 1999.

[77] J.S. Parker, L.R. Moore, E.S. Smyth, and K.T. Taylor. *J. Phys. B*, 33:1057, 2000.

[78] J.S. Parker, L.R. Moore, K.J. Mehring, D. Dundas, and K.T. Taylor. *J. Phys. B*, 34:L69, 2001.

[79] J.S. Parker, J.S. Doherty, K.J. Meharg, and K.T. Taylor. *J. Phys. B*, 36:L393, 2003.

[80] A. Becker and F.H.M. Faisal. *J. Phys. B*, 29:L197, 1996.

[81] A. Becker and F.H.M. Faisal. *Phys. Rev. Lett.*, 84:3546, 2000.

[82] A. Becker and F.H.M. Faisal. *Phys. Rev. Lett.*, 89:193003, 2002.

[83] S.V. Popruzhenko and S.P. Goreslavskii. *J. Phys. B*, 34:L239, 2000.

[84] S.P. Goreslavskii and S.V. Popruzhenko. *Opt. Express*, 8:395, 2001.

[85] R. Kopold, W. Becker, H. Rottke, and W. Sandner. *Phys. Rev. Lett.*, 85:3781, 2000.

[86] S.P. Goreslavskii, Ph.A. Korneev, S.V. Popruzhenko, R. Kopold, and W. Becker. *J. Mod. Opt.*, 50:423, 2003.

[87] C. Figueira de Morisson Faria, X. Liu, W. Becker, and H. Schomerus. *Phys. Rev. A*, 69:021402, 2004.

[88] A. Becker and F.H.M. Faisal. *Phys. Rev. A*, 59:R1742, 1999.

[89] A. Becker and F.H.M. Faisal. *J. Phys. B*, 32:L335, 1996.

[90] S.P. Goreslavskii, S.V. Popruzhenko, R. Kopold, and W. Becker. *Phys. Rev. A*, 64:053402, 2001.

[91] C. Figueira de Morisson Faria, H. Schomerus, X. Liu, and W. Becker. *Phys. Rev. A*, 69:043405, 2004.

[92] M. Weckenbrock, A. Becker, A. Staudte, M. Smolarski, V.R. Bhardwaj, and D.M. Rayner. *Phys. Rev. Lett.*, 91:123004, 2003.

[93] T. Brabec, M.Yu. Ivanov, and P. B. Corkum. *Phys. Rev. A*, 54:R2551, 1996.

[94] H.W. van der Hart and K. Burnett. *Phys. Rev. A*, 62:013407, 2000.

[95] G.L. Yudin and M.Yu. Ivanov. *Phys. Rev. A*, 63:033404, 2001.

[96] V.R. Bhardwaj, S.A. Aseyev, M. Mehendale, G.L. Yudin, D.M. Villeneuve, D.M. Rayner, M.Y. Ivanov, and P.B. Corkum. *Phys. Rev. Lett.*, 86:3522, 2001.

[97] V.L. Bastos de Jesus, B. Feuerstein, K. Zrost, D. Fischer, A. Rudenko, F. Afaneh, C.D. Schröter, R. Moshammer, and J. Ullrich. *J. Phys. B*, 37:L161, 2004.

[98] J. Chen, J. Liu, L.B. Fu, and W.M. Zheng. *Phys. Rev. A*, 63:011404, 2001.

[99] L.B. Fu, J. Liu, J. Chen, and S.G. Chen. *Phys. Rev. A*, 63:043416, 2001.

[100] L.B. Fu, J. Liu, and S.G. Chen. *Phys. Rev. A*, 65:021406, 2002.

[101] K. Sacha and B. Eckhardt. *Phys. Rev. A*, 63:043414, 2001.

[102] D. Bauer. *Phys. Rev. A*, 56:3028, 1997.

[103] M. Dörr. *Opt. Express*, 6:111, 2000.

[104] M. Lein, E.K.U. Gross, and V. Engel. *Phys. Rev. Lett.*, 85:4707, 2000.

[105] W.C. Liu, J.H. Eberly, S.L. Haan, and R. Grobe. *Phys. Rev. Lett.*, 83:520, 1999.

[106] R. Panfili, J.H. Eberly, and S.L. Haan. *Opt. Express*, 8:431, 2001.

[107] M. Lein, E.K.U. Gross, and V. Engel. *J. Phys. B*, 33:433, 2000.

[108] M. Lein, V. Engel, and E.K.U. Gross. *Opt. Express*, 8:411, 2001.

[109] A.M. Popov, O.V. Tikhonova, and E.A. Volkova. *Opt. Express*, 8:441, 2001.

[110] S.L. Haan, P.S. Wheeler, R. Panfili, and J.H. Eberly. *Phys. Rev. Lett.*, 66:061402, 2002.

[111] C. Szymanowski, R. Panfili, W.C. Liu, S.L. Haan, and J.H. Eberly. *Phys. Rev. A*, 61:055401, 2000.

[112] J. Ullrich and V.P. Shevelko. *Many-Particle Quantum Dynamics in Atomic and Molecular Fragmentation*. Springer Series on Atomic, Optical, and Plasma Physics, 2003.

[113] J. Ullrich, R. Moshammer, A. Dorn, R. Dörner, L.Ph.H. Schmidt, and H. Schmidt-Böcking. Recoil-ion and electron momentum spectroscopy: reaction-microscopes. *Rep. Prog. Phys.*, 66:1463, 2003.

[114] J. Ullrich and H. Schmidt-Böcking. *Phys. Lett. A*, 125:193, 1987.

[115] J. Ullrich, M. Horbatsch, V. Dangendorf, S. Kelbch, and H. Schmidt-Böcking. *J. Phys. B*, 21:611, 1988.

[116] R. Moshammer, M. Unverzagt, W. Schmitt, J. Ullrich, and H. Schmidt-Böcking. *Nucl. Instrum. Methods B*, 108:425, 1996.

[117] O. Jagutzki, V. Mergel, K Ullmann-Pfleger, L. Spielberger, U. Spillmann, R. Dörner, and H. Schmidt-Böcking. *Nucl. Instrum. Methods A*, 477:244, 2002.

[118] D.R. Miller. *Atomic and Molecular Beam Methods*. Oxford University Press, 1988.

[119] O.F. Hagena et al. *J. Chem. Phys.*, 56:1793, 1972.

[120] O.F. Hagena. *Rev. Sci. Instrum.*, 63:2374, 1992.

[121] J. Wörmer, V. Guzielski, J. Stapelfeldt, and T. Möller. *Chem. Phys. Lett.*, 159:321, 1989.

[122] H. Beijerinck and N. Verster. *Physica*, 111C:327, 1981.

[123] E.L. Knuth. *J. Chem. Phys.*, 66:3515, 1977.

[124] RoentDeck Handles GmbH. *MCP detector with delay-line anode*, 2000.

[125] David A. Dahl. *SIMION 3D Version 6.0 User's Manual*, idaho national engineering laboratory edition, 1995.

[126] F. Lindner, G.G. Paulus, F. Grasbon, A. Dreischuh, and H. Walther. *IEEE J. Quantum Electron.*, 38:1465, 2002.

[127] P. Maine, D. Strickland, P. Bado, M. Pessot, and G. Mourou. *IEEE J. Quantum Electron.*, 24:398, 1988.

[128] M.G. Schätzel and F. Lindner. privat communication.

[129] N.B. Delone and V. P. Krainov. *Physics-Uspekhi*, 41:469, 1998.

[130] G.G. Paulus, F. Grasbon, H. Walther, R. Kopold, and W. Becker. *Phys. Rev. A*, 64:021401(R), 2001.

[131] Christoph Trump. *"Atomare and molekulare Fragmentationsdynamik in intensiven ultrakurzen Lichtpulsen"*. PhD thesis, Technische Universität Berlin, 2000.

[132] N.B. Delone and V.P. Krainov. *J. Opt. Soc. Am. B*, 8:1207, 1991.

[133] R. Panfili, S.L. Haan, and J.H. Eberly. *Phys. Rev. Lett.*, 89:113001, 2002.

[134] Schomerus. bla. Privat communication.

[135] Hugo W. van der Hart. *J. Phys. B*, 33:L699, 2000.

[136] A. Talebpour, C.-Y. Chien, Y. Liang, S. Larochelle, and S. L. Chin. *J. Phys. B*, 30:1721, 1997.

[137] C. Cornaggia and Ph. Hering. *Phys. Rev. A*, 62:023403, 2000.

[138] C. Guo and G. N. Gibson. *Phys. Rev. A*, 63:040701, 2001.

[139] V.R. Bhardwaj, D.M. Rayner, D.M. Villeneuve, and P.B. Corkum. *Phys. Rev. Lett.*, 87:253003, 2001.

[140] H. Niikura, F. Légaré, R. Hasbani, A.D. Bandrauk, M.Yu. Ivanov, D.M. Villeneuve, and P.B. Corkum. *Nature*, 417:917, 2002.

[141] A.S. Alnaser, T. Osipov, E.P. Benis, A. Wech, B. Shan, C.L. Cocke, X.M. Tong, and C.D. Lin. *Phys. Rev. Lett.*, 91:163002, 2003.

[142] H. Sakai, J.J. Larsen, I. Wendt-Larsen, J. Olesen, P.B. Corkum, and H. Stapelfeldt. *Phys. Rev. A*, 67:063404, 2003.

[143] A. Talebpour, C.-Y. Chien, and S. L. Chin. *J. Phys. B*, 29:L677, 1996.

[144] F. Grasbon, G.G. Paulus, S. L. Chin, H. Walther, J. Muth-Böhm, A. Becker, and F.H.M. Faisal. *Phys. Rev. A*, 63:041402(R), 2001.

[145] J. Muth-Böhm, A. Becker, and F.H.M. Faisal. *Phys. Rev. Lett.*, 85:2280, 2000.

[146] M.B. Smirnov and V.P. Krainov. *Phys. Scr.*, 57:420, 1998.

[147] M.B. Smirnov and V.P. Krainov. *J. Exp. Theor. Phys.*, 86:323, 1998.

[148] J.J. Larsen, H. Sakai, C.P. Safvan, I. Wendt-Larsen, and H. Stapelfeldt. *J. Chem. Phys.*, 111:7774, 1999.

[149] J.J. Larsen, K. Hald, N. Bjerre, and H. Stapelfeldt. *Phys. Rev. Lett.*, 85:2470, 2000.

[150] F. Rosca-Pruna and M.J.J. Vrakking. *Phys. Rev. Lett.*, 87:153902, 2001.

[151] M.J. DeWitt, B.S. Prall, R.J. Levis, D.M. Rayner, D.M. Villeneuve, and P.B. Corkum. *J. Chem. Phys.*, 113:1553, 2000.

[152] A.D. Bandrauk and J. Ruel. *Phys. Rev. A*, 59:2153, 1999.

[153] A. Talebpour, S. Larochelle, and S. L. Chin. *J. Phys. B*, 31:L49, 1998.

[154] X.M. Tong, Z.X. Zhao, and C.D. Lin. *Phys. Rev. A*, 66:033402, 2002.

[155] Z.X. Zhao, X.M. Tong, and C.D. Lin. *Phys. Rev. A*, 67:043404, 2003.

[156] A. Jaroń-Becker, A. Becker, and F.H.M. Faisal. *Phys. Rev. A*, 69:023410, 2004.

[157] I.V. Litvinyuk, K.F. Lee, P.W. Dooley, D.M. Rayner, D.M. Villeneuve, and P.B. Corkum. *Phys. Rev. Lett.*, 90:233003, 2003.

[158] C. Guo. *Phys. Rev. Lett.*, 85:2276, 2000.

[159] C. Guo, R.T. Jones, and G.N. Gibson. *Phys. Rev. A*, 62:015402, 2000.

[160] A. Saenz. *J. Phys. B*, 33:4365, 2000.

[161] J.S. Prauzner-Bechcicki, K. Sacha, B. Eckhardt, and J. Zakrzewski. *submitted to Phys. Rev. A*, 2004.

[162] M.J. DeWitt, E. Wells, and R.R. Jones. *Phys. Rev. Lett.*, 87:153001, 2001.

[163] E. Wells, M.J. DeWitt, and R.R. Jones. *Phys. Rev. A*, 66:013409, 2002.

[164] E.P. Benis, J.F. Xia, X.M. Tong, M. Faheem, M. Zamkov, B. Shan, P. Richard, and Z. Chang. *Phys. Rev. A*, 70:025401, 2004.

[165] A.S. Alnaser, S. Voss, X.M. Tong, C.M. Maharjan, P. Ranitovic, B. Ulrich, T. Osipov, B. Shan, Z. Chang, and C.L. Cocke. *Phys. Rev. Lett.*, 93:113003, 2004.

[166] T.K. Kjeldsen and L.B. Madsen. *J. Phys. B*, 37:2033, 2004.

[167] B. Feuerstein, R. Moshammer, and J. Ullrich. *J. Phys. B*, 33:L823, 2000.

Publications

The following papers have been published in the course of the present work:

- E. Eremina, X. Liu, H. Rottke, W. Sandner, M.G. Schätzel, A. Dreischuh, G.G. Paulus, H. Walther, R. Moshammer, and J. Ullrich,
  Influence of molecular structure on double ionisation of N_2 and O_2 by high intensity ultra-short laser pulses,
  Phys. Rev. Lett. **92**, 173001 (2004);

- E. Eremina, X. Liu, H. Rottke, W. Sandner, A. Dreischuh, F. Lindner, F. Grasbon, G.G. Paulus, H. Walther, R. Moshammer, B. Feuerstein and J. Ullrich,
  Laser-induced non-sequential double ionisation investigated at and below the threshold for electron impact ionization,
  J. Phys. B **36**, 3269-3280 (2003);

- X. Liu, H. Rottke, E. Eremina, W. Sandner, E. Goulielmakis, K. O´Keeffe, M. Lezius, F. Krausz, F. Lindner, M.G. Schätzel, G.G. Paulus, H. Walther,
  Nonsequential double ionisation at the single-optical-cycle limit,
  Phys. Rev. Lett. **93**, 263001 (2004).

Acknowledgements

At the end of my thesis I would like to thank all those people who have contributed to the success of this work.

First of all I want to express my deepest gratitude to Prof. Dr. Wolfgang Sandner for giving me the opportunity to carry out this exciting research work in his group at the Max Born Institute, for encouraging and supporting me throughout all my PhD, for promoting the presentation of the experimental results at numereous conferences and meetings.

I am most indebted to Dr. Horst Rottke for guiding this project and my work, for providing most of the ideas realized in this experiment, for being always open for discussions, giving me advice and helping in all questions. The success of our experiments and my thesis in particular would not be possible without his enormous contribution and support. I also thank Horst for thoroughly proofreading of my thesis.

I am very grateful to my colleagues from the Max Plank Institute for Quantum Optics, Gerhard Paulus, Michael Schätzel, Alexander Dreischuh, and Fabrizio Lindner for providing the laser system for our experiments, for the collaboration, for the support and hospitality during the time of our experiment in Garching.

I also thank my colleagues from the Max Plank Institute für Kernphysik for collaboration, especially Robert Moshammer and Bernhold Feuerstein for helping during the adjustment of our first coincident electron-ion measurements.

I would especially like to thank my colleagues at the Division B2 of the Max Born Institute:

Elena Gubbini for the friendly atmosphere and heartiness, her aid during all the time and especially at writing my thesis;

Dr. Xiaojun Liu for the excellent cooperation, assistance in many problems, and giving an incentive for our semiclassical model calculations;

Rainer Hoffmann for helping with electrical equipment during the build-up phase, as well as Ralph Ewers for the mechanical part;

Stefan Gerlach for helping with the computer problems;

Silvia Szlapka and Bettina Haase for the perfect organizing work, mutual understanding and cordiality;

I would like to express my sincere thanks to my colleagues and friends Michael

Schtätzel, Dr. Artem Rudenko, Dr. Sven Gnutzmann for their countenance and making me confident with my abilities during the difficult stages of my thesis. I am also indebted to Sven for his help with the correction of my thesis.

Moreover, many thanks to the people, not mentioned by name, who contributed to the successful completion of this thesis.

Finally, I heartily thank my family for the emotional support and encouragement.